Electromagnetic Modelling and Optimization for SPECT-MRI and Auricular Vagus Nerve Stimulation

Elektromagnetische modellering en optimalisering van SPECT-MRI en stimulatie van de auriculaire nervus vagus

Mohammed Samoudi

Promotoren: prof. dr. ir. W. Joseph, prof. dr. ir. E. Tanghe
Proefschrift ingediend tot het behalen van de graad van
Doctor in de ingenieurswetenschappen: elektrotechniek

UNIVERSITEIT
GENT

Vakgroep Informatietechnologie
Voorzitter: prof. dr. ir. B. Dhoedt
Faculteit Ingenieurswetenschappen en Architectuur
Academiejaar 2017 - 2018

ISBN 978-94-6355-087-1
NUR 927, 928
Wettelijk depot: D/2018/10.500/5

UNIVERSITEIT GENT

FACULTEIT INGENIEURSWETENSCHAPPEN EN ARCHITECTUUR

Promotors
Prof. dr. ir. Wout Joseph
Prof. dr. ir. Emmeric Tanghe

Chair
Prof. dr. ir. Daniël De Zutter, (Ghent University, Belgium)

Other members of the examination board
Prof. dr. ir. Jan Vanfleteren (Ghent University, Belgium), secretary
Prof. dr. Kaniusas Eugenijus (Vienna University of Technology, Austria)
dr. ir. Vincent Keereman (Ghent University Hopsital, Belgium)
Prof. dr. ir. Roel Van Holen (Ghent University, Belgium)
dr. ir. Günter Vermeeren (Ghent University, Belgium)

Acknowledgment

"In the middle of every difficulty lies opportunity."
Albert Einstein

After an intensive period of almost five years, today is the day: writing this note of thanks is the finishing touch on my dissertation. It has been a period of intense learning for me, not only in the scientific arena, but also on a personal level. Writing this dissertation has had a big impact on me. I start this acknowledgment by giving thanks and praises to God.

I would like to reflect on the people who have supported and helped me so much throughout this period. I am greatly indebted to my supervisors profs. Wout Joseph, and Emmeric Tanghe. I am sincerely grateful to Wout for his availability, for giving me confidence when I needed it, for his patience with me, his help during some tough moments and for being my daily guide during this doctorate. I really appreciate the collaboration with Wout. Many thanks to Emmeric, who has deepened my knowledge in the neuro-stimulation and biomedical applications. I appreciate his enthusiastic and friendly way of discussion. I would like to thank prof. Luc Martens for the opportunity to join his group to pursue a PhD. Besides, his helpful and constructive critics have always improved the quality of my researches. I am also grateful to prof. Dick Botteldooren and prof. Timothy Van Renterghem for giving me the opportunity to work on the ultrasound project.

Besides my advisors, I would like to thank the rest of my jury: prof. Daniël De Zutter, prof. Jan Vanfleteren, prof. Kaniusas Eugenijus, prof. Roel Van Holen, dr. Vincent Keereman, and dr. Günter Vermeeren for their encouragement and insightful comments. Their comments, critics, and suggestions have helped me to improve the quality and the flow of the dissertation.

A very special gratitude goes out to prof. Eugen, prof. Jozsef, Stefan, Sarah and Florian from research group biomedical sensing, TU Vienna. Special thanks to Günter who helped me a lot with simulations and resolved several issues with license server.

I seize this opportunity to thank all my (ex)colleagues at WAVES: Reza, Sander, Xu, Toon, Thomas, Sunil, Simon, Sergei, Roel, Rodney, Reza, Quentin, Ning, Nico, Mostafa, Michel, Margot, Kris, Jens, Frederic, David, Brecht, Arno, Divya, Rodney, Kang, Matthias, Leen, Sam, Gemma, and Yang. I would like to thank everyone from the SIMRET project, especially prof. Roel, Karen, Carmen, and

Gregory from MEDISIP for the great insights in SPECT and MRI.

I have also a thought here for my friends in Ghent (Chabiha group): Nacereddine, Yaseer (& sons), Moez, Younes, Said, Mouad, and Rafiq. May God bless you all. Thank you all for Saturday meetings, discussions and your helping hand. Thanks Younes Balou, who somehow showed me that being a millionaire is not a matter of degrees. Thank Tahar for the time we have had. Thanks Abdellatif for being my housemate in Rabat and Montreal and for all the memories we have had. Thanks Ismail, Majid, Bechar, Soufiane, and every ex-colleague from INPT. Special thanks to all INPT professors.

I would like to thank my wife Masude for standing beside me throughout my career and writing this book. I also thank my wonderful and lovely child Yassine. Thank you both for always making me smile and for understanding on those weekends when I was writing this book instead of being home. I hope that one day Yassine can read this book and understand why I spent so much time in front of my computer. My family, including my in-laws, have always supported me throughout my career and authoring this book and I really appreciate it. Special thank to dr. Jamal, Rachida, Aymane, Amine and Israe.

Infinite thanks to my bother Soufiane and sisters Imane and Jihane and all my family. Thanks for your constant supports, sacrifices and blessings.

Last but not least, my deepest gratitude to my parents: Naima & Ahmed. Thanks for fashioning me to be who I am, the blessings, and everything. I owe you everything. There are no words strong enough to describe my gratitude and respect for you.

My special thankfulness, warmth, and appreciation to everyone!

Amine M. Samoudi
Ghent, January 2018

Table of Contents

List of Figures

List of Tables

List of Acronyms

A

ABVN	Auricular Branches Vagus Nerve
ABVNS	Auricular Branches Vagus Nerve Stimulation
AP	Action Potential
AV	Average

C

CAD	Computer Aided Design
CT	Computed Tomography

D

DSV	Diameter of Spherical Volume

E

EPI	Echo-Planar Imaging
EM	Electromagnetic

F

FDTD	Finite Difference Time Domain

FID	Free Induction Decay
FOV	Field Of View

I

ICNIRP	International Commission on Non-Ionizing Radiation Protection
IEC	International Electrotechnical Commission
INSERT	Integrated SPECT/MRI for enhanced stratification in radio-chemotherapy

M

MoM	Method of Moments
MRI	Magnetic Resonance Imaging

N

NMR	Nuclear Magnetic Resonance

P

PAD	Peripheral Arterial Disease
PET	Positron Emission Tomography
PNS	Peripheral Nerve Stimulation
pVNS	Percutaneous Vagus Nerve Stimulation

R

RF	Radio Frequency
RMS	Root Mean Square
Rx	Receiver
RX	X-ray Radiography

S

SAR	Specific Absorption Rate
SENN	spatially Extended Nonlinear Node
SIMRET	Simultaneous Magnetic Resonance Imaging and Emission Tomography
SPECT	Single Photon Emission Computed Tomography

T

Tx	Transmitter

U

US	UltraSound

V

VNS	Vagus Nerve Stimulation

Nederlandse samenvatting

Elektromagnetische modellering en optimalisering van SPECT-MRI ...

Een recente ontwikkeling in het domein van de medische beeldvormingstechnologie is de verschuiving van enkelvoudige naar multimodale beeldvorming. In het bijzonder is er toegenomen belangstelling voor de combinatie van SPECT (single-photon emission computed tomography) met MRI (magnetic resonance imaging) systemen. Dit heeft vele voordelen: terwijl MRI een hoog contrast garandeert van de zachte weefsels in het lichaam en geen stralingsdosis met zich meebrengt, kan SPECT een inzicht bieden in een breed scala aan biologische processen. De SPECT/MRI-technologie staat echter ook voor verschillende uitdagingen, zoals een beperkte beschikbare ruimte, rotatie van SPECT-detectors en MR-compatibiliteit van het gecombineerde systeem. De snel schakelende MRI-velden induceren **wervelstromen** in de omliggende materialen, die op hun beurt aanleiding geven tot een geïnduceerd magneetveld. Dit geïnduceerde veld kan de lineaire gradiëntvelden verstoren en tegenwerken, hetgeen aanleiding geeft tot artefacten in het beeld en lokalisatiefouten.

Deze snel schakelende magnetische velden zijn noodzakelijk voor het genereren van ultra-snelle beeldsequenties, zoals in "echo planar imaging" en leveren beelden van hogere kwaliteit. Snel schakelende magnetische velden induceren echter niet alleen wervelstromen, maar geven ook aanleiding tot membraandepolarisatie en bijgevolg tot **stimulatie van zenuwen in het perifere zenuwstelsel**. De patiënt kan dit ervaren als onaangenaam tot ondraagbaar. Bijgevolg moet de fysiologische limiet voor blootstelling aan deze velden, gebaseerd zijn op het minimaliseren van onaangename sensaties. Als richtlijn voor de maximale tijdsafgeleide van het magnetisch veld en het geïnduceerde elektrische veld, wordt door IEC (2010) en ICNIRP (2004) een blootstellingslimiet vermeld van 80% van de mediane perceptiedrempel voor routine behandelingen en van 100% van de mediane perceptiedrempel voor gecontroleerde behandelingen. Omdat het praktisch moeilijk is om het geïnduceerde elektrische veld op te meten in het menselijk lichaam, kan men gebruik maken van **simulaties** die de geïnduceerde velden evalueren in realistische **menselijke modellen**, die geplaatst zijn in **"volledige-humaans" x-, y- en z-gradiëntspoelen**. De bekomen gesimuleerde velden kunnen vervolgens gebruikt worden in de vergelijking met de opgelegde blootstellingslimieten.

In Hoofdstuk 2 wordt een numeriek model voorgesteld van de x-, y- en z- gradiëntspoelen en de pentagonale en hexagonale opstelling van de collimatoren, dat gebruikt wordt om het magnetisch veld te bestuderen dat geïnduceerd wordt door

wervelstromen in het SPECT/MRI-systeem. We vertrekken van metingen van de resistiviteit van geprint wolfraam en een schatting van het effect van de wervelstromen op een prototype van een enkele collimator. Vervolgens karakteriseren we het magnetisch veld, dat geïnduceerd wordt in de opstelling van pentagonale en hexagonale collimatoren, en rapporteren we de impact van de gradiëntspoelen op het magnetisch veld.

Hoofdstuk 3 gaat verder in op de mogelijkheid om residuele wervelstromen in het SPECT/MRI-systeem te reduceren, door slimme aanpassingen aan te brengen in het ontwerp van de collimatoren. Eerst bepalen we de stroomdichtheid (J) in verschillende ontwerpen van enkelvoudige collimatoren en we vergelijken deze met de stroomdichtheid in de oorspronkelijke collimator. Vervolgens berekenen we het geïnduceerde magnetisch veld voor elke spoel van de aangepaste collimatoren en bespreken we de vermindering in het maximale geïnduceerde magnetische veld ten gevolge van de wervelstromen.

In Hoofdstuk 4 wordt de blootstelling van volwassenen en kinderen in een MR-scanner bepaald, door gebruik te maken van de gesimuleerde geïnduceerde elektrische velden in een realistisch 3D model van een volwassen man en vrouw en in kindmodellen, die geplaatst werden in afgeschermde x-, y-, en z-gradiëntspoelen. Het simulatieplatform werd eerst gevalideerd door vergelijking met analytisch bekomen resultaten, waarbij de beschrijving van de methodologie van de bepaling van het E-veld gebaseerd is op de richtlijnen van ICNIRP 2004 en IEC 2010. Vervolgens berekenen we de in-situ elektrische velden en vergelijken we de bekomen resultaten met de ICNIRP 2004 en IEC 2010 richtlijnen, om perifere zenuwstimulatie in patiënten te vermijden. De impact van het type spoel, het menselijk model en de geleidbaarheid van de huid op de geïnduceerde velden wordt ook besproken.

...en stimulatie van de auriculaire nervus vagus

Stimulatie van de cervicale nervus vagus gunstig in de behandeling van klinische depressie, refractaire epilepsie en congestief hartfalen. In conventionele nervus vagus stimulatie wordt een pulsgenerator operatief geïmplanteerd in de borstkas van de patiënt. Een onderhuidse draad, die de nervus vagus met de pulsgenerator verbindt, zal vervolgens de elektrische pulsen geleiden om de nervus vagus te stimuleren. Een alternatieve minder invasieve en recent ontwikkelde technologie is **percutane stimulatie van de auriculaire tak van de nervus vagus** (pVNS). Hierbij worden fijne naaldelektrodes in de oorschelp geplaatst, om zo de zenuwvertakkingen van de nervus vagus te bereiken. Huidige medische toepassingen van pVNS lijden echter aan een gebrek aan stimulatienauwkeurigheid en een minder goed gekende variabiliteit van de therapeutische resultaten. Dit heeft tot gevolg dat de methode aan potentieel verliest, in het bijzonder wanneer de stimulatie gebeurt in een gebied van de oorschelp met een hoge graad aan bezenuwing en met zenuwvezels van verschillende oorsprong, hetgeen aanleiding kan geven tot tegengestelde fysiologische reacties. Bijgevolg zijn simulaties noodzakelijk om de meest geschikte gebieden voor nervus vagus stimulatie te vinden en de gebruikte golfvormen voor de geïnjecteerde stroom en het opgewekte veld te optimaliseren.

Deze optimalisatie kan bovendien op gepersonaliseerde basis gebeuren. Het grote belang van de nauwkeurigheid van de stimulatie maakt de **sensitiviteitsanalyse** van het ontwikkelde numerieke model een onmisbaar instrument, om zo beter de afhankelijkheid van het model ten opzichte van de verschillende input parameters te kwantificeren. Alsook kan de link gelegd worden tussen de verschillende bronnen van onzekerheid in de numerieke input-parameters en de onzekerheid in de model-output.

Hoofdstuk 5 is gewijd aan het ontwerp van een **realistisch model voor pVNS**. We onderzoeken de impact van de positie en diepte van de elektrodes en de golfvorm van de stimulus op de exciteerbaarheid van enkelvoudige axonen en bundels van meerdere axonen. Een titratiemechanisme wordt gebruikt om de drempel voor zenuwstimulatie te bepalen voor verschillende stimulusgolfvormen, zoals monofasische, bifasische, anodische en kathodische pulsen. Het percentage geactiveerde axonen en de stimulatiedrempel voor activatie van een volledige axon populatie wordt gepresenteerd. De invloed van de positie en de diepte van de elektrode op het percentage geactiveerde axonen wordt ook besproken.

In Hoofdstuk 6 wordt een sensitiviteitsanalyse uitgevoerd op een numeriek model, dat ontwikkeld werd in Hoofdstuk 5. Het doel is om prioriteiten te stellen en invloedrijke parameters te identificeren, alsook om de modelrespons als functie van de input parameters in kaart te brengen. Indien nodig, beperken we hiervoor het bereik van de beschouwde input parameters. Bestudeerde parameters zijn de axondiameter, het aantal axonen, de model temperatuur, de geleidbaarheid van het oor en de diepte en positie van de gebruikte elektrodes. Tot slot wordt dit werk in Hoofdstuk 7 afgerond en worden de mogelijkheden omtrent toekomstig onderzoek voorgesteld.

Dit onderzoek werd uitgevoerd in de onderzoeksgroep WAVES in de vakgroep INTEC van de faculteit ingenieurswetenschappen. Het voorgestelde werk resulteerde in 6 A1-tijdschriftpublicaties als eerste auteur (waarvan er 2 momenteel nog onder review is), en 10 bijdrages op internationale conferenties en workshops.

English summary

Electromagnetic Modelling and Optimization for SPECT/MRI...

Recently, medical imaging technology is shifting from single to multimodality imaging. More recently, there is increased interest for combined single-photon emission computed tomography (SPECT) and magnetic resonance imaging (MRI) systems that have many advantages. MRI has a higher soft-tissue contrast without involving any radiation dose. SPECT can provide insight into a wide range of biological processes. However, SPECT/MRI insert results in different challenges, including space constraints, rotation of SPECT detectors, and MR compatibility of the combined system. The rapidly switching MRI gradient fields will induce **eddy currents** in the surrounding materials, which in turn produces an induced magnetic field that opposes and distorts the linear gradient fields and gives rise to image artifact and tissues localization errors.

Rapidly switching gradients are needed for ultra-fast imaging sequences such as echo planar and provides better imaging results. However, these rapidly changing magnetic fields will not only induce eddy currents, but can also lead to depolarization of membranes and subsequent nerve stimulation of the peripheral nervous system causing uncomfortable or intolerable sensation in the patients. Therefore, the physiological limit of exposure to such fields should be based on minimizing uncomfortable or intolerable sensation. The IEC (2010) and ICNIRP (2004) guidelines limitations for the time variation of the magnetic field or the induced electric fields are set 80% of the median perception threshold for **peripheral nerve stimulation** for routine operations, and 100% of the median perception threshold for controlled operations. Measurements of the induced electric field in the human body are practically difficult to be performed. Thus, **numerical simulations** should be developed to evaluate and compare the induced fields with standard limitations, using realistic whole-body **human models** within **whole-body x, y, and z gradient coils**.

Chapter 2 presents the numerical model of x, y, and z gradient coils along with pentagonal and hexagonal configurations of the collimators used to investigate the induced magnetic field due to eddy currents in SPECT/MRI system. We start by measurements of the printed tungsten resistivity along with an estimation of the eddy currents effect on a single prototype collimator. We then characterized the induced magnetic field in pentagonal and hexagonal collimator arrangements, and reported the effect of the gradient coils on the induced magnetic field.

Chapter 3 is a continuation of the residual eddy currents reduction in SPECT/MRI

system by introducing smart design modifications in the collimators. We started by evaluation of the current density (J) for different single collimators design and compared it to the original collimator current density. We then calculated the induced magnetic field for each ring of the adapted collimators and reduction in the maximum induced magnetic field due to eddy current was reported and discussed.

In Chapter 4, exposure of adults and children in an MR scanner was evaluated using the induced electric fields in realistic 3D whole-body adult male, adult female, and child models within shielded whole-body x, y, and z gradient coils. First, the simulation platform was validated against analytically derived results with description of the E-field evaluation methodology based on the ICNIRP 2004 and IEC 2010 guidelines. We then calculated in-situ electric fields and compare results with ICNIRP 2004, and IEC 2010 guidelines to prevent peripheral nerve stimulation in the patients. Effect of the coils' type, human model type, and skin conductivity on the induced electric fields was also reported and discussed.

...and Auricular Vagus Nerve Stimulation.

Stimulation of the cervical vagus nerve is beneficial for major depression, refractory epilepsy, and congestive heart failure. In conventional vagus nerve stimulation, a device is surgically implanted in the patient's chest with a wire threaded under the skin connecting the device to the vagus nerve. The device will then send electrical signals to stimulate the vagus nerve. **Percutaneous stimulation of the auricular branch of the vagus nerve** (pVNS) is a recently developed, and less invasive technique, based on using small needle electrodes in targeted regions of the auricle to access the nerve branches instead of surgically implanting the stimulation device. However, current clinical applications in pVNS lack in specificity of the stimulation with less known variation of the therapeutic effect, which reduces the stimulation potential of the method, especially when the stimulation occurs in a dense innervation region of the auricle with nerve fibers of different origin, leading to possible opposite physiological reactions. Thus, numerical simulations are necessary to identify and optimize the stimulation areas as well as the applied field and current patterns on individual level. The huge importance of the stimulation specificity and sensitivity makes the **sensitivity analysis** of the developed numerical model, an invaluable tool to better quantify the dependence of the numerical model to different parameters and adjust the uncertainty in the model output to different sources of uncertainty in the numerical model parameters.

Chapter 5 is dedicated to design a **realistic model of the pVNS** application and investigate the effect of the electrode depth and position, as well as the stimulation pattern on the excitation threshold in single and bundled axons. We used titration mechanism to investigate the nerves stimulation thresholds using different stimulation patterns including mono-phasic, bi-phasic, anodic, and cathodic pulses. The percentage of activated axons and stimulation thresholds for a complete axon population activation were presented with discussion of the effect of the electrode depth and position on the percentage of stimulated axons.

In Chapter 6, a sensitivity analysis of a numerical model developed in Chap-

ter 5 was performed. The objective is to prioritize and identify the influential and non-influential parameters and map the output behavior as a function of the input parameters by limiting the input range values to a specific domain if necessary. The investigated parameters include the fiber diameter, number of axons, model temperature, ear conductivity, as well as electrodes penetration depth and position.

Finally, Chapter 7 concludes this work and opportunities for future research are proposed.

This research was performed at the research group WAVES in the INTEC department of the faculty of engineering. The work presented here resulted in six A1 journal papers as a first author (of which two are still under review), and ten contributions at international conferences and workshops.

1 Introduction

The work presented in this dissertation is situated in the field of numerical modelling and optimization of biomedical applications. We used different computational tools to design and optimize the phenomenon of eddy currents in SPECT/MRI system, followed by the assessment of the induced electric field in patients undergoing MR scanning, and finally we investigated the auricular branches vagus nerve (ABVN) stimulation with sensitivity analysis of the numerical models. Firstly, we will give a general overview of medical imaging modalities and more specifically the problem of eddy currents arising from combining MRI and SPECT system. Secondly, we will discuss the safety considerations of patients in magnetic resonance imaging system. Finally, we will present the electrical stimulation of myelinated nerve and more specifically the spatially extended nonlinear node (SENN) model.

1.1 Medical Imaging

In modern medicine, medical imaging represents the process used to retrieve visual representations about the patient's interior anatomy and physiological functions of its organs and tissues. Imaging technologies form a significant component of the health budgets of all developed economies, and a lot of people need advanced imaging such as Magnetic Resonance Imaging (MRI), X-Rays and Computed Tomography (CT) scans during their life. It is also widely used for research purposes to investigate new treatments and enlarge our knowledge of the human

body physiological functions. Medical imaging is derived from the interaction of energy with human tissue. The energy can be in the form of radiation, magnetic or electric fields, or acoustic energy. Several medical imaging modalities are available to the patient. Every technique has risks and benefits and it is intended for specific applications. Thus different techniques can be proposed to the patient, especially when diagnosis is difficult. Imaging modalities can be classified into two categories: functional imaging techniques, mostly Positron Emission Tomography (PET) and Single Photon Emission Computed Tomography (SPECT); and anatomical imaging techniques like Computed Tomography (CT), X-ray Radiography (RX), Ultrasound (US), and Magnetic Resonance Imaging (MRI).

1.1.1 Magnetic Resonance Imaging

MRI is an imaging modality that uses non-ionizing radiation to create anatomical diagnostic images based on the nuclear magnetic resonance (NMR) principle. An MRI system consists of a strong magnet in which the patient lies (in the order of 0.2-14 Tesla), two radio frequency coils (RF) used to send signals to the body (transmit (Tx)) and then receive signals back (receiver (Rx)) and gradient coils for spatial encoding. These returning signals are converted into images by a computer attached to the scanner. Imaging of almost any part of the human body can be obtained in any plane.

Figure 1.1 shows an abbreviated description of the MRI imaging mechanism. First, the patient is placed in a static magnetic field (B_0). Hydrogen protons within the patient's body align to the magnetic field (polarized state) and precesses around the axis of the magnetic field (conventionally in the z-axis along the long axis of the patient) at the Larmor frequency. An RF pulse send by the Tx coil, tuned at the proton precessing frequency will then depolarize the longitudinal magnetisation of the protons. As soon as the RF is switched off, the transverse magnetisation begins to disappear and the protons relax back to their polarized state resulting in emitted RF radiation (at their Larmor frequency) intercepted by the Rx coil. Since the proton signal frequency is proportional to the magnetic field, a given proton signal frequency can be assigned to a location in the tissue, providing a map of the tissue in terms of the protons presence. Knowing that the proton density varies with the type of tissue, a certain amount of contrast is achieved to image the organs and other tissue variations in the subject tissue. A spatial encoding can be obtained by varying the protons spin-flip frequency with 3 different well-calibrated magnetic field gradients across the patient (in X-, Y- and Z-direction). The signal received by the Rx coil (containing location information encoded in the frequencies) is then separated by means of the Fourier transform to produce a two-dimensional map of the different tissues. Other mechanisms are used to reconstruct images in MRI:

spin-lattice (T1), spin-spin (T2), and free induction decay (T2* relaxation).

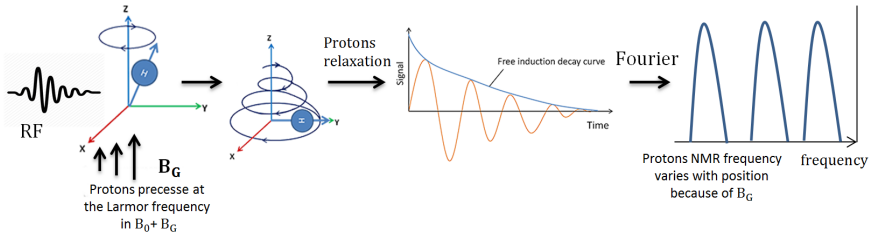

Figure 1.1: Basic principles of MRI: An RF pulse excites protons that are subjected to a static magnetic field B_0, together with a gradient magnetic field B_G, which is position dependent. After turning off the RF pulse, the protons relax back to their polarized state and while doing so, they emit an RF signal (FID: free induction decay). After Fourier transforming the FID, every frequency corresponds to a different location in the patient (due to B_G).

Figure 1.2 shows the main parts of an MR system. It is mainly composed of three parts: a strong magnet producing a static magnetic field, gradient coils producing a gradient magnetic field and a radio-frequency system.

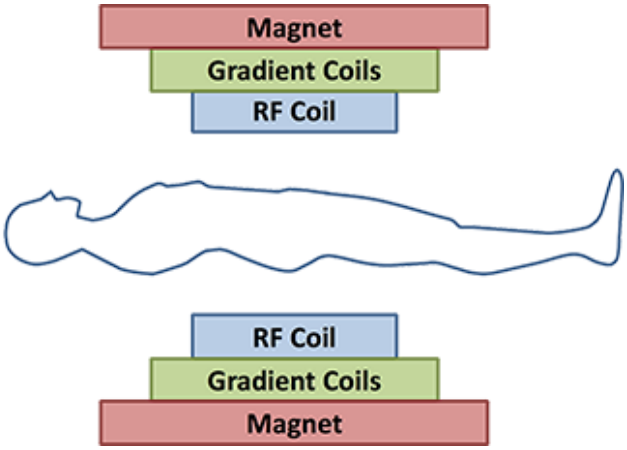

Figure 1.2: An MR system with the magnet, the gradient coils and the RF coil.

1.1.1.1 Static Magnetic Field

The main magnet is a superconducting, copper winding, electromagnet cooled with helium (- 270°) to produce a strong static magnetic field B_0 along the z-axis in Figure 1.2 . This magnetic field can only be disabled by quenching the magnet. Quenching means that the helium is rapidly removed from the magnet

in order to disable the strong magnetic field. This is only done in emergency situations because of the cost of helium. In clinical MRI scanners, the strength of the main magnetic field is 1.5T or 3T. The small animal MRI scanner that is used for the measurements in this thesis has a static magnetic field of 14T. Due to its high strength, the magnetic field is not only present inside the bore of the scanner. The magnetic field outside the scanner is called the fringe field. For safety measures it is important to shield the main magnet to reduce the fringe field. This can be done in two ways. Passive shielding is done by applying iron plates that surround the magnet. The other way is active shielding by applying windings in opposite direction outside the inner magnet to cancel out the main magnet field. An important property of the static magnetic field is the homogeneity in the field of view of the scanner. Non-homogeneities result in geometrically distorted images and can be reduced with both passive and active shimming techniques. Passive shimming is done during the installation of the scanner by positioning steel plates around the magnet. Active shimming is done during a pre-scan phase so that the main magnetic field in the bore is optimized per patient.

1.1.1.2 Gradient Coils

Gradient coils are used to produce variations in the main magnetic field B_0. The gradient field is along the z-axis for each of the three gradient coils (z-axis in Figure 1.2).There are three sets of gradient coils, one for each direction. The variation in the magnetic field permits localization of image slices as well as phase encoding and frequency encoding. Figure 1.3 shows and example of x, y, and z gradient coils. The gradient fields are three magnetic fields that are rapidly switched on and off during the MRI sequence and oriented orthogonal to each other. They are mainly used for spatial encoding of the MRI signals and are produced by gradient coils. The orientation of the gradients are termed as follows: the z axis is the direction along the bore, the x axis is the direction from left to right and the y axis is the direction from top to bottom (Figure 1.2). The strength of the gradient field is expressed as how rapidly the field changes with distance (mT/m). The maximum gradient amplitude in clinical MRI scanners is in the order of 10- 50 mT/m. The small animal 7T MRI system can have a maximum gradient strength of 500 mT/m. Higher gradient strength allows to acquire images faster or with better resolution. Other performance indicators are the gradient slew rate (defined as ratio of the peak gradient amplitude to the rise time) and the linearity. A linear variation in the field of view is required for proper spatial encoding. Nonlinearity of the gradient field will cause misplaced signals resulting in geometric distortions.

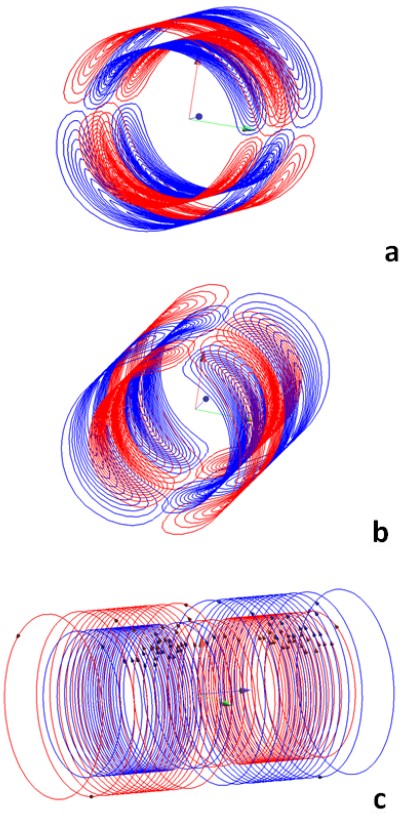

Figure 1.3: (a) X-gradient coil. (b) Y-gradient coil and(c) Z-gradient coil (Source: Poole [1]). Red and blue colors are used to indicate wires in which there is a different sense of current flow.

1.1.1.3 Radio-Frequency Coils

The radio-frequency system consists of two components, the transmitter coil and the receiver coil. The transmitter coil generates well designed radio frequent pulses in order to excite the nuclei of the desired slice. Therefore, the RF pulses have a predefined center frequency, bandwidth, amplitude and phase.

The center frequency of the pulse is determined by the slice position and the strength of the slice select gradient. The thickness of the slice is determined by the bandwidth of the pulse. The larger the transmitter coil, the more uniform its field. Therefore, in clinical MRI scanners, the transmitter coil is typically integrated in the scanner bore. The main function of the transmitter coil will be explained in the section about how the image is generated. Some transmitter coils can also operate as receiver coil. However, the larger the distance from the patient, the

lower the signal. That is the reason why in most cases specific receiver coils are used. These coils can be adapted to the anatomy of the part of interest so they can be as close as possible to the tissue in order to maximize the signal and minimize the noise. Examples of anatomy-specific coils are head (Figure 1.4) and knee coils. There are three types of receiver coils: volume coils that detect the signal from the whole volume surrounded by the coil, surface coils that detect only signals near the surface of the coil and phased area coils that are combinations of surface coils and volume coils.

Figure 1.4: An 8-channel RF coil for clinical brain imaging (Source: Siemens [2]).

1.1.1.4 Encoding Basics

The information about how this magnetization is distributed in the body is derived by the frequency and phase of its precession during the detection phase of the experiment. After excitation, the detected MR signal processes with a frequency (Larmor frequency) given by $\omega = \gamma B_0$ where $\gamma = 2\pi$ (42.577 MHz/T) is the gyro-magnetic ratio of a proton. At the start of the imaging process, an RF electromagnetic wave is transmitted by an RF coil. Meanwhile, a gradient coil will be switched on for the slice selection. For axial-plane imaging, the z gradient coil will be switched on, and the x gradient coil will be switched on for sagittal-plane imaging, and the y gradient coil will be switched on for coronal-plane imaging. If we take the axial-plane imaging as an example, when the z gradient coil is switched on, the magnetic field along the axial direction will be linearly varied and the precession frequency will also be linearly varied. The tuned narrow-band electromagnetic field will be absorbed by a slice of the target tissue. It is the protons on that slice that are excited. The overall magnetization vector of the protons on the slice will shift to be deviated from the original magnetization direction. Af-

ter the slice selection, a frequency-encoded gradient coil will be switched on. For instance, for the x gradient coil, the gradient strength is denoted by G_x. Thus, in the x direction, the precession frequency of the protons on the slice will be linearly varied along the x direction. If only the x gradient coil is switched on, there will be frequency encoding only in the x direction. All the protons on this slice precess at the same phase. However, for the imaging, a y-direction gradient magnetic field is also applied, which is used to produce a phase encoding. Assuming the y gradient strength is G_y, a phase shift will be created as

$$\phi = \gamma G_x y t \tag{1.1}$$

and the frequency encoding by the x gradient coil is expressed as

$$\omega = \gamma G_y x \tag{1.2}$$

The frequency and phase information from the MRI signal corresponds to the k-space of the twodimensional (2D) Fourier transform of an image. That is, the data in the MRI is in the frequency domain.

1.1.2 Single-Photon Emission Computed Tomography

Single-photon emission computed tomography (SPECT) is a nuclear medicine tomographic imaging technique. In clinical practice, almost all nuclear medicine procedures that use single photon emission tracers rely on the use of the gamma camera. It is a gamma ray position sensitive detector that typically consists of large slab of scintillator crystal with position circuitry and energy determination. To localize the emission site of the released photons, a multipinhole collimator is mounted on the front face of the system to provide a spatial correlation of the detected events. SPECT provides functional information with the advantage that it can provide information about regional tissue function, which usually changes during a disease [3]. The main elements of the SPECT are the tracer, gamma camera, and the acquisition system.

SPECT tracer: SPECT imaging is based on the radioactive decay of an injected tracer. The most commonly radionuclide used for SPECT is 99m-technetium. The decay of Technetium-99m to Technetium-99 occurs via the emission of gamma rays of 140 keV. Besides Technetium-99, Indium-111, Gallium-67, or Iodine-131 are also often used [4].

Gamma camera: The gamma camera will then be used to detect the emitted photons and consists of a collimator and a detector:

Detector: The SPECT detector components are the scintillation crystal to convert the gamma rays to light, photomultiplier tubes to detect the light, and analogue-digital converters that process the signals coming from the photomultipliers tubes.

Recently, detectors use semiconductors to directly convert the radiation in electrons [5].

Collimator: The main function of the collimator is to limit the direction of incidence of the photons heading towards the detector. It is mostly used to determine the angle of incidence of the incoming photon and therefore, along with the detector, we can define the original location of the photon. Collimators are made from material with a high number of electrons (typically Z from 72 to 82) and high density in order to have a sufficient stopping power. High stopping power is necessary to attenuate enough photons in order to build collimators that allow the reconstruction of high resolution images [6].

Image reconstruction: After the scan, 3D images are then produced using a series of planar projections at different angles around the patient. Images are then examined and reported by a nuclear medical physicist so that the medical doctor can then make a diagnosis.

1.1.3 Multimodality Imaging

Recently, medical imaging technology is shifting from single to multimodality imaging. Hybrid systems including both functional and anatomical imaging have become very popular over the past decade. SPECT and PET as functional imaging modalities have already been combined with CT [7].

Integrated whole-body positron emission tomography (PET)/MR hybrid imaging combines excellent soft tissue contrast and various functional imaging parameters provided by MR with high sensitivity and quantification of radiotracer metabolism provided by positron emission tomography. In 2010, the first commercially available whole body systems for PET/MR hybrid imaging entered the market, based on two separate MR and PET imagers in one room (Philips Ingenuity TF PET/MRI, Best, The Netherlands) [8], followed by a fully integrated whole-body PET/MR hybrid imaging system (Biograph mMR; Siemens AG, Healthcare Sector, Erlangen, Germany) [9] that enables simultaneous PET/MR data acquisition. Since then, the number of worldwide installations of PET/MR systems has increased steadily, making possible the introduction of new diagnostic applications and products in oncology, neurology, pediatric oncology, and cardiovascular disease [10]. Although the first clinical evaluation of integrated PET/MR is under way [11–13], it is a technically challenging method that relies on new technologies and innovative solutions. Current research topics include: MR-based attenuation correction of human soft tissues and hardware components, the lack of bone information with MR imaging, the limited field of view (FOV) in MR, and the implementation of motion correction technologies [10].

Recently, Mediso [14] and MRSolutions [15] developed a sequential preclin-

ical SPECT/MRI system. However, no simultaneous SPECT/MRI systems have been built so far. Combining SPECT with MRI over the CT has many advantages. For example, MRI system has a higher spatial resolution enhanced by higher soft-tissue contrast. Moreover, MRI does not involve any radiation dose like CT. The MRI/SPECT system can also benefit from the SPECT mechanisms to provide insight into a wide range of biological processes. Combining SPECT with MRI can be advantageous over the PET/MRI for two main reasons. First, the SPECT system has a lower cost price over the PET system due to availability of longer half-life radionuclides (few hours to few days). SPECT radionuclides are easier to handle and can be produced and distributed by pharmaceutical companies easily. However, PET tracers have a shorter half-life (few minutes to few hours), which drastically increases the operational costs. Another advantage of SPECT over PET is the possibility to do dual-tracer imaging, enabling specific targeting abilities. However, combining SPECT and MRI systems results in many challenges related to rotation of SPECT detectors, collimator material compatibility and space constraints. In fact, MRI localization is based on rapidly switching gradient fields. This rapidly changing magnetic field induces circular electric currents (eddy currents) within conducting structures.

The eddy currents will then produce an induced magnetic field that opposes and distorts the linear gradient fields in the region of interest, resulting in image artifacts, MR pictures with blurring and ghosting [16–18]. The eddy currents also cause forces on the conductors inside MRI system, which results in noise and reduction of the lifetime [19]. Although many approaches have been proposed to minimize the generation of eddy currents (active and passive shielding coils, current pulse pre-emphasis, less conductive magnet bore materials and alternative cryostat configurations) [20–24], significant distortions will often remain. This is particularly the case in the presence of highly conductive objects where eddy currents are characterized by long time constants [18]. Collimators are composed of materials that have a high gamma ray absorption (usually an alloy of lead and tungsten). The choice of collimation material is determined by the density, cost, required rigidity, and the machining complexity [5]. Several numerical approaches have been proposed to simulate the eddy currents effect in MRI. However, no simulation of the tungsten collimator insert inside MRI systems have been performed so far. As a numerical method, the network method, has been applied in the analysis of the currents induced by axially symmetric coils (e.g., z-gradient) in a realistic cryostat [19, 23, 25]. The three-dimensional FDTD method for the modeling of low-frequency transient eddy currents in MRI was developed in [26, 27] and used to design gradient coils while taking into account the eddy currents effects. Thus, numerical modelling of the preclinical SPECT/MRI system is important to investigate and reduce the induced eddy current in the collimators due to x-, y-, and z-gradient coils for different arrangements of tungsten collimators. Different de-

signs and arrangements of the tungsten collimators should be proposed to reduce the induced magnetic fields due to eddy currents.

1.2 Safety Considerations of Patients in Magnetic Resonance Imaging System

Interactions of the living tissue with MRI scanner can cause potential patient risks. Rapidly induced fields could stimulate nerves of the peripheral nervous system (PNS). Nerve stimulation might interfere with the examination. Therefore, the physiological limit of exposure to such fields should be based on minimizing uncomfortable or intolerable sensation.

Different guidelines and standards suggest limits to mitigate these potential hazards. The IEC standard (2010) [28] and the ICNIRP (2004) [29] have two levels related to PNS for the induced electric field: the normal operating mode (L_{01}) and the first level controlled operating mode (L_{12}). L_{01} refers to the mode of operation of the MR equipment in which none of the fields have a value that can cause physiological stress to patients. L_{12} refers to the mode of operation of the MR equipment in which one or more outputs reach a value that can cause physiological stress to patients which needs to be controlled by medical supervision. MR equipments that allows the operation in the first level controlled operating mode shall comply with the following requirements:

- Before the start of each scan, an indication of the operating mode defined by the predicted value of the gradient output and SAR, to be applied during the scan shall be displayed at the control panel.
- If the value of the gradient output or SAR that controls the scan is such as to enter the first level controlled operating mode, the attention of the operator shall be drawn to this condition by a clear indication on the control panel. A record of the operating mode or equivalent data shall be an integral part of the image data.
- A deliberate action of the operator shall be necessary in order to enter the first level controlled operating mode.

L_{01} and L_{12} are calculated as follows:

$$L_{01} = 0.8\ rb\ (1 + \frac{0.36\ ms}{t_{s,eff}}) \tag{1.3}$$

$$L_{12} = 1.0\ rb\ (1 + \frac{0.36\ ms}{t_{s,eff}}) \tag{1.4}$$

where $t_{s,eff}$ (ms) and rb(in T/s or V/m) denote the effective stimulus duration and the rheobase (rheobase is the maximum exposure level for an infinite stimulus duration) given in Table 1.1. L_{01} and L_{12} as well as rb shall either be expressed as the electric field E (V/m) induced or as the time rate of change of the magnetic field dB/dt (T/s).

The effective stimulus duration $t_{s,eff}$ is defined as the duration of any period of the monotonic increasing or decreasing gradient, used to describe its limits for cardiac or peripheral nerve stimulation. It is defined as the ratio of the peak-to-peak field variation and the maximum value of the time derivative of the gradient in that period (see Figure 1.5). Three periods of monotonic change of the gradient G are shown in Figure 1.5a. The corresponding gradient output dB/dt is shown in Figure 1.5b and the effective stimulus duration $t_{s,eff}$ is indicated. Figure 1.6 shows limits for peripheral nerve stimulation for different values of the effective stimulus duration $t_{s,eff}$.

Type of gradient system	rb expressed as E(V/m)	rheobase expressed as dB/dt (T/s)
Whole body gradient system	2.2	20
Special purpose gradient system	2.2	Not applicable

Table 1.1: Rheobase values per type of gradient system [28]

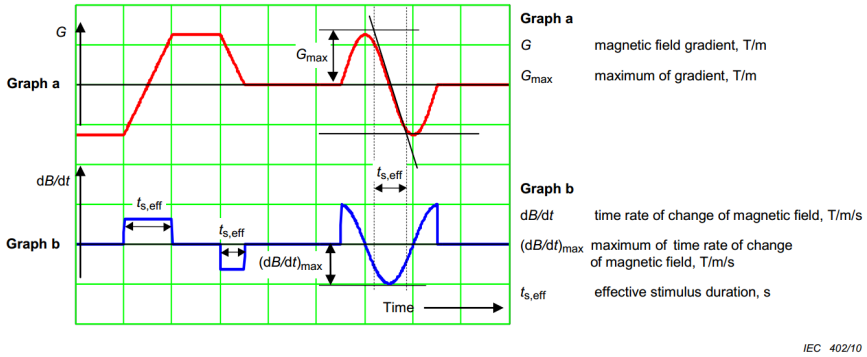

Figure 1.5: Three periods of monotonic change of the gradient G are shown in graph a. The corresponding gradient output dB/dt is shown in graph b and the effective stimulus duration $t_{s,eff}$ is indicated [28].

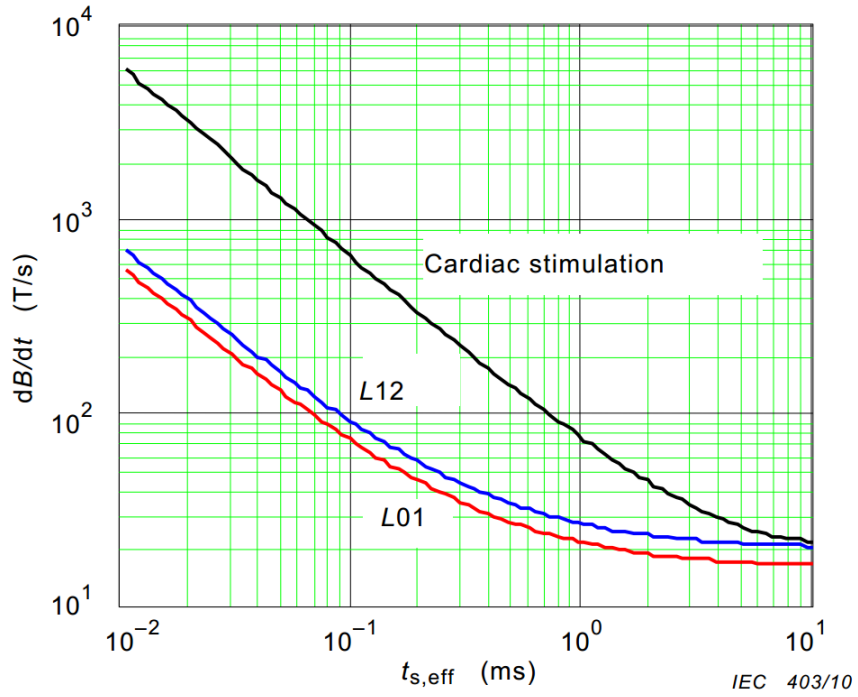

Figure 1.6: Limits for peripheral nerve stimulation. The limit for cardiac stimulation is shown for comparison [28].

The IEC (2010) and ICNIRP (2004) [28–30] guidelines suggest limiting the time variation of the magnetic field or the induced electric field to 80% of the median perception threshold for peripheral nerve stimulation (PNS) for routine operations, and 100% of the median perception threshold for controlled operations. To comply with the guidelines, the induced electric field should be measured in the human tissue and compared to the limits, which is practically difficult to be performed. Numerical simulations were then developed to evaluate and compare the induced fields with standard limitations.

Several studies tried to simulate and investigate the PNS phenomenon in MRI, each with its own limitations. Spherical and cylindrical tissue models were used in [31] with the electric scalar potential method to calculate the internal electric field. Simplified cylindrical models of a body and gradient coil were used in [32] to calculate the exact solution to Maxwell's equations and predict the transient E-fields induced within the body model by the rapid switching of current in the coil. Mao et al. [33] used a "limited tissue" male body model (visible phantom) and only x-gradient coil model to investigate the induced E-field. In [34] and [35], finite difference time domain (FDTD) was applied to simulate gradient field-induced E-fields and induced currents within a human model using homogeneous conducting rotational ellipsoid model, and two human male models (visible phantom, limited tissue and resolution), one with homogeneous conductivity and the other with non-homogeneous conductivity. As reported, only simplified human models were used for these investigations. However, since the human body size and tissues locations inside the MRI coils are different between adult male, adult female and child models, the choice of the human body model can have and important impact on the induced electric field. Another important issue, not considered in the PNS literature, is the modelling of the skin in the low-frequency magnetic field exposure. Schmid et al. [36] reported that the skin tissue conductivity can be a potential source of errors and uncertainties concerning computations of induced electric field strengths in the low frequency range, which is the case for PNS due to switching gradient coils. Thus, numerical simulations of adults and children exposure to whole-body MRI system (x-, y-, and z-gradient coils) and comparison with the guidelines is important to fully understand the effect of the coil type (transverse and longitudinal coils), human model type (adult male, adult female, and child), and skin conductivity on the induced electric fields. Compliances with IEC2010 and ICNIRP2004 on medical magnetic resonance: protection of patients guidelines should be investigated for all the configurations.

1.3 Vagus Nerve Stimulation

1.3.1 Nerve Cell Structure

Neurons form the basic functional elements of the nervous system. Each neuron contains a nerve cell body with a nucleus and organelles. Branching off the nerve cell body are the dendrites. Most neurons have several dendrites which are extensively branched. The incoming neural signal is relayed via the axon in the form of an electrical signal, the action potential, to the synapse. At the synapse, neural signals are chemically transmitted to a postsynaptic receiver cell via secretion of neurotransmitter molecules that bind to receptors at the postsynaptic specialisation. Depending on the direction of the information transfer, neurons are classified as afferent or efferent if they transfer information to or from the brain, respectively. Because the propagation of an action potential is based on the active depolarisation of the cell membrane, the resulting conduction velocity of the axon is governed by the ion exchange rate. By insulating the membrane with myelin, the number of sites where the depolarisation occurs is limited to the nodes of Ranvier, resulting in saltatory conduction between those nodes. Myelination therefore greatly enhances the conduction velocity of an action potential along the axon [37].

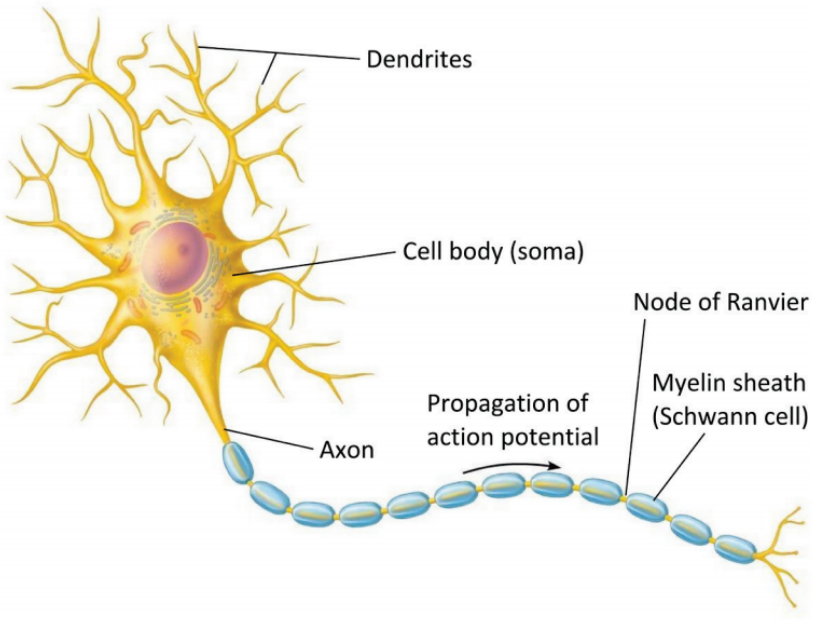

Figure 1.7: Structure of typical neuron (source [37]).

1.3.2 Representation of the Electrical Stimulation of Myelinated Nerve

Vagus nerve effective stimulation in humans is mediated by thick myelinated afferent Aβ axon fibers [38]. In this section, the electrical stimulation of myelinated nerve is represented in 1.3.2 and the transmembrane voltage equation is presented in 1.3.3 along with equations of the SENN (Spatially Extended Nonlinear Node) model parameters.

Figure 1.8 shows a general representation of a myelinated fiber subject to an induced electric field. The current travels from the stimulus electrode to the fiber, through the conducting medium, causing external voltage disturbances, $V_{e,n}$, at the nearby nodes. Depending on the direction of the transmembrane current flow, these disturbances can either trigger depolarization or hyperpolarization of the membrane.

Figure 1.9 shows an equivalent representation of the myelinated nerve as formulated by McNeal [39]. The individual nodes are represented as a circuit elements consisting of capacitance (C_m), resistance (R_m), and a potential source (E_r). Each nodal membrane circuit element is connected to the following circuit through the resistance of the axoplasmic fluid, R_a. The potential source E_r is caused by the differences in the ionic concentration between the outside and the inside of the axon along with different conductances for each ion. The voltages $V_{e,n}$ are the external nodal voltages as shown in Figure 1.8, resulting from the induced electric fields in the conducting medium by the applied electromagnetic field or the stimulus current. Section 1.3.3 will elaborate on the equations of the transmembrane voltage and the ionic current.

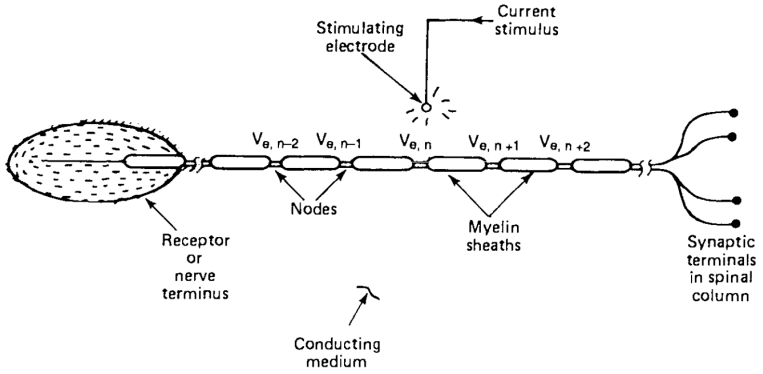

Figure 1.8: Representation of electrical stimulation of myelinated nerve. The current stimulus results in voltage disturbances $V_{e,n}$ at the individual nodes. These in turn cause a local depolarization of the nerve membrane [39].

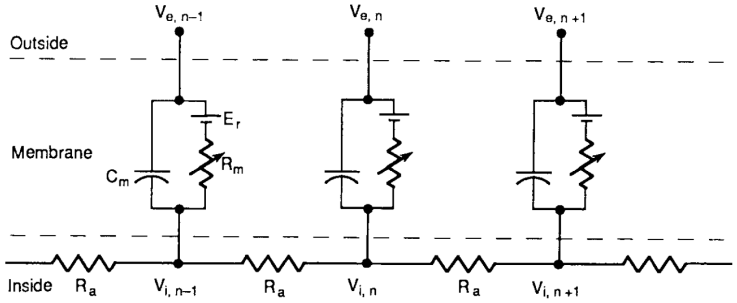

Figure 1.9: Equivalent circuit models for excitable membranes [39].

1.3.3 Transmembrane Voltage

The current emanating from the n^{th} node in Figure 1.9 is then the sum of the capacitive and ionic currents, and is related to internal ionic current, $I_{i,n}$, by

$$C_m \frac{dV_n}{dt} + I_{i,n} = G_a(V_{i,n-1} - 2V_{i,n} + V_{i,n+1}) \tag{1.5}$$

where C_m(F) is the membrane capacitance of the node and G_a(S) is the internodal conductance through the axoplasmic fluid ($1/R_a$ in Figure 1.9). $I_{i,n}$(A) is the internal ionic current flowing in the n^{th} node and V_n (V) is the transmembrane potential at the n^{th} node. V_n is considered relative to the resting potential, in a way that positive V_n applies to depolarization form the membrane's resting potential, while negative V_n implies hyperpolarization.

$$V_n = V_{i,n} - V_{e,n} \tag{1.6}$$

where $V_{i,n}$ and $V_{e,n}$ are the internal and external nodal voltages, respectively. Expressions of G_a, G_m ($1/R_m$ in Figure 1.9), and C_m are given by

$$G_a = \frac{\pi d^2}{4\rho_i L_i} \tag{1.7}$$

$$G_m = g_m \pi d w \tag{1.8}$$

$$C_m = c_m \pi d w \tag{1.9}$$

where d is the axon diameter at the node, L_i is the internodal gap, ρ_i is the resistivity of the axoplasm, c_m is the membrane capacitance per unit area, g_m is the subthreshold membrane conductance per unit area, and w is the nodal gap width. The internodal distance, L_i, is related to the fiber diameter D by

$$L_i = 100D \tag{1.10}$$

which is in turn related to the axon diameter d by

$$d = 0.7D \tag{1.11}$$

Other than D, the other variables on the right-hand side of Eqs. 1.7, 1.8, and 1.9 are fiber diameter independent. Substituting Eq. 1.6 into Eq. 1.5 results in:

$$\frac{dV_n}{dt} = \frac{1}{C_m}[G_a(V_{n-1} - 2V_n + V_{n+1} + V_{e,n-1} - 2V_{e,n} + V_{e,n+1}) - I_{i,n}] \tag{1.12}$$

The ionic current $I_{i,n}$ in Eq. 1.12 can be expressed in a linear membrane:

$$I_{i,n} = G_m V_n \tag{1.13}$$

1.3.4 E-field Interaction with the Nerve and Neuroelectric Modes of Excitation

Iteration of the applied electric field with the nerve can be described in Figure 1.10. Figure 1.10 shows the three principal modes of neuro-electric excitation as follows: bend mode (where the axon's trajectory undergoes bend), end mode (for sensory receptor or motor-neuron end plate for example), or at a spatial gradient of the electric field. Depending on the configuration conditions, one or another of these three modes can be dominant. More than one mode can be simultaneously activated. In such cases, action potentials can be launched from more than one node by a single stimulus waveform. The bend and end modes (the 2 upper graphs in Figure 1.10) are sensitive to the magnitude of the E-fields rather than its gradient, thus nerve excitation does occur where there is a significant electric field surrounding the neuron [40]. For the spatial gradient mode, maximum depolarization occurs where the spatial gradient of the E-field is maximally positive [40].

For stimuli of long duration and long straight axons, the change in membrane potential relative to its resting value is given by:

$$-\lambda^2 \frac{\partial E_x}{\partial x} \tag{1.14}$$

where λ is the membrane space constant, E_x is the component of the electric field along the direction of the axon, and $\frac{\partial E_x}{\partial x}$ is the directional derivative of the electric field along the same direction. Equation 1.14 shows that that axons will be first depolarized in the region where the component of the electric field along the axon is decreasing most rapidly in the direction of the axon (gradient mode) [41].

Stimulation of axons can also occurs at axon terminations or sharp bends, even in the absence of electric field gradients [41]. In this case, and provided the axon is long compared to its space constant, the membrane depolarization is given by

$$-\lambda E_x \tag{1.15}$$

where E_x is the component of the electric field along the direction of the axon at the termination ([42]). At sharp right angle bends, this figure is reduced by a factor of 2. According to equation 1.15, axons will be depolarized first where terminations or sharp bends occur in regions where the electric field along the direction of the axon is high.

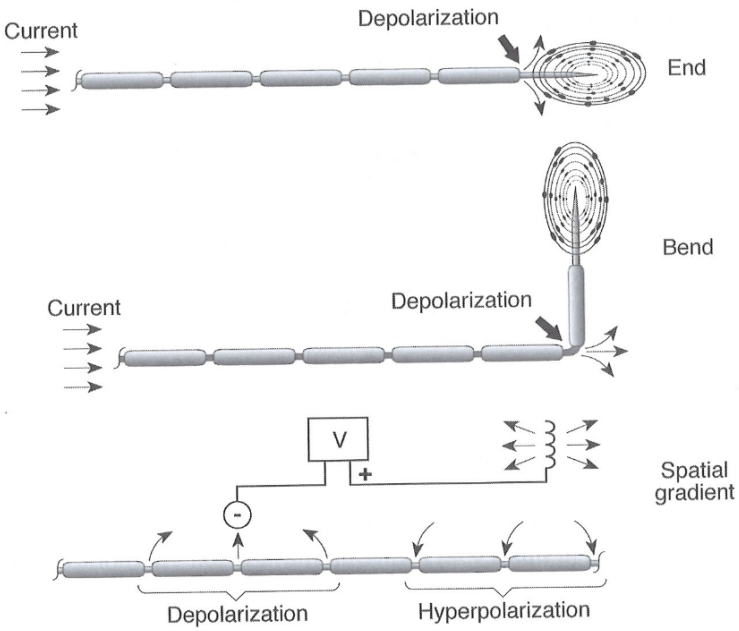

Figure 1.10: Modes of neural stimulation. Excitation is initiated at points of maximum current efflux acorss a neural membrane. Point excitation sites of fiber terminals, sharp bends, and the maximal spatial gradient of the E-field [43].

1.3.5 Vagus Nerve Stimulation Clinical Application and Challenges

While the peripheral nerve stimulation is an undesired effect for patients undergoing MRI scans and should be limited, stimulation of the cervical vagus nerve is beneficial for therapeutic refractory epilepsy, major depression, and congestive

heart failure [44, 45]. In fact, the vagus nerve, an important component of the autonomic nervous system, plays a major role in the regulation of metabolic homeostasis by controlling and regulating the function of various glands, and organs throughout the body [46]. Vagus nerve stimulation (VNS) refers to any technique that stimulates the vagus nerve, including manual or electrical stimulation. Left cervical VNS is an approved therapy for refractory epilepsy and for treatment resistant depression [47]. Right cervical VNS is effective for treating heart failure in preclinical studies. In conventional vagus nerve stimulation, a device is surgically implanted under the skin on the patient chest, and a wire is threaded under the skin connecting the device to the left vagus nerve. When activated, the device sends electrical signals along the vagus nerve to the brainstem, which then sends signals to certain brain areas [47].

Percutaneous stimulation of the auricular branch of the vagus nerve (pVNS) is a recently developed, and less invasive technique, to minimize the associated risks of the surgical implantation [48, 49]. pVNS relies on the introduction of small needle electrodes in targeted regions of the auricle to access the nerve branches. The major current applications of the pVNS are the treatment of chronic pain [50] and peripheral arterial disease (common circulating problem in which narrowed arteries reduce blood flow to the limbs) [51]. However, current clinical applications in pVNS are still based on empirical selection of both stimulation regions and parameters with unknown variation of the therapeutic effect, which affect the specificity of the stimulation, especially when the stimulation occurs in a dense innervation region of the auricle with nerve fibers of different origin. This leads to possible opposite physiological reactions [52]. Thus, numerical simulations are necessary to optimize the stimulation areas as well as the applied field and current patterns on individual level. Simulations of the electromagnetic fields excited in human biological tissue by artificial neurostimulation are limited to the most common types of neurostimulation, e.g., for peripheral nerve stimulation [53], transcranial magnetic stimulation [54], deep brain stimulation [55, 56], and spinal cord stimulation [57]. Therefore, it is important to establish, a realistic high-resolution model of the pVNS application and investigate the effect of the electrodes' depth and position, as well as the stimulation pattern on the excitation threshold in single and bundled axons. The importance of the stimulation specificity and sensitivity makes the sensitivity analysis of the numerical model, an invaluable tool to better quantify the dependence of the numerical model to different parameters. The sensitivity analysis will be used to link the uncertainty in the model output to different sources of uncertainty in the model parameters. It will also be used to identify the most contributing input parameter and ascertain interaction effects within the model. Thus, we can achieve a better model verification and understanding, factor prioritization, and model simplification.

1.4 Main Research Contributions and Outline

The general topic of this dissertation is numerical modelling and optimization of the SPECT/MRI system and Auricular Vagus Nerve Stimulation. The first part of this dissertation will be focused on the numerical modelling and optimization of induced eddy currents in SPECT/MRI systems. The second part deals with exposure of patients inside MR systems. The final part is dedicated to the Auricular Vagus Nerve Stimulation modelling and optimization. The following subjects are described in the chapters of this thesis.

In Chapter 2, a detailed numerical model of x, y, and z gradient coils along with pentagonal and hexagonal configurations of the collimators were used to investigate the induced magnetic field due to eddy currents in SPECT/MRI system. The numerical model was validated with measurements. Measurements of the printed tungsten resistivity were performed and an estimation of the induced eddy currents using a single prototype collimator was reported. We then investigated the induced magnetic field in a full ring of pentagonal and hexagonal ring of collimators, and studied the effect of adding gaps between the collimators in the pentagonal geometry to reduce eddy current density to less than 2 % of the applied gradient field.

Chapter 3 continues the investigation and reduction of eddy currents in SPECT/MRI system by introducing design modifications (slit-slat, material reduction) in the collimators to optimize the SPECT system. First, the current density (J) was evaluated for different single collimator design and compared to the original collimator current density. The induced magnetic field was then calculated for each ring of the adapted collimators and reduction in maximum induced magnetic field due to eddy current was reported and discussed.

The rapidly changing MRI gradient fields are not only the cause of induced eddy currents in collimators but can also lead to depolarization of membranes and subsequent nerve stimulation of the peripheral nervous system causing uncomfortable or intolerable sensation in the patients. In Chapter 4, exposure of adults and children in an MR scanner was evaluated using the induced electric fields in realistic 3D whole-body adult male, adult female, and child models within shielded whole-body x-, y-, and z-gradient coils. The calculated in-situ electric fields were then compared with ICNIRP 2004 and IEC 2010 guidelines to prevent peripheral nerve stimulation in the patients. The simulation platform was validated against analytically derived results and the E-field evaluation methodology, based on the guidelines, was also detailed. We then, compared the induced electric field with limitations of the ICNIRP 2004, and IEC 2010 standard. This study was extended to include investigation of the effect of coil's type, human model type, and skin conductivity on the induced electric fields.

In Chapter 5, a realistic numerical modelling of the pVNS application at the human auricle including vessels and nerves was established. The simulation model

was verified with analytical results using the myelinated nerve model. The electric field distribution in the ear and its spatial derivative are then calculated and the stimulation thresholds for each configuration are calculated and compared. The titration mechanism was used to investigate the effect of different stimulation patterns using mono-phasic, bi-phasic, anodic, and cathodic pulses. The percentage of activated axons and stimulation thresholds to obtain 100 % axon activation are presented for each axon population with discussion of the effect of the electrode depth and position on the percentage of stimulated axons.

Chapter 6 is dedicated to a sensitivity analysis of the numerical model developed in Chapter 5. We started by specifying the input parameters range of values. Then the effects of fiber diameter, number of axons, model temperature, ear conductivity, as well as electrodes' penetration depth and position on the stimulation thresholds for single and bundled axons was assessed and discussed. The final goal is to identify and prioritize the most influential parameters, identify non-influential parameters in order to fix them to nominal values, and map the output behavior as a function of the parameters by limiting the input range values to a specific domain if necessary.

Finally, Chapter 7 summarizes this dissertation and addresses futures research.

1.5 Publications

1.5.1 Publications in International Journals (A1)

[AS1] **A. M. Samoudi**, K. Van Audenhaege, G. Vermeeren, M. Poole, L. Martens, R. Van Holen, and W. Joseph, "Analysis of eddy currents induced by transverse and longitudinal gradient coils in different tungsten collimators geometries for SPECT/MRI integration", *Magnetic Resonance in Medicine*, vol. 74, no. 6, pages:1780-1789, 2015.

[AS2] **A. M. Samoudi**, K. Van Audenhaege, G. Vermeeren, G. Verhoyen, L. Martens, R. Van Holen, and W. Joseph, "Simulated design strategies for SPECT collimators to reduce the eddy currents induced by MRI gradient fields", *IEEE TRANSACTIONS ON NUCLEAR SCIENCE*, vol. 62, no. 5, pages:2017-2022, 2015.

[AS3] **A. M. Samoudi**, G. Vermeeren, E. Tanghe, R. Van Holen, L. Martens, and W. Josephs, "Numerically simulated exposure of children and adults to pulsed gradient fields in MRI", *JOURNAL OF MAGNETIC RESONANCE IMAGING*, vol. 44, no. 5, pages:1360-1367, 2016.

[AS4] **A. M. Samoudi**, S. Kampusch, E. Tanghe, JC. Szeles, L. Martens, E. Kaniusas, and W. Joseph, "Numerical modelling of percutaneous auricular vagus nerve stimulation: a realistic 3D model to evaluate sensitivity of neural

activation to electrode position", *MEDICAL & BIOLOGICAL ENGINEERING & COMPUTING*, vol. 55, no. 10, pages:1763-1772, 2017.

[AS5] **A. M. Samoudi**, S. Kampusch, E. Tanghe, JC. Szeles, L. Martens, E. Kaniusas, and W. Joseph, "Sensitivity analysis of a numerical model for percutaneous auricular vagus nerve stimulation", *MEDICAL & BIOLOGICAL ENGINEERING & COMPUTING*, 2017. Under review

[AS6] **A. M. Samoudi**, E. Tanghe, L. Martens, and W. Joseph, "Deep transcranial magnetic stimulation: improved coil design and assessment of the induced fields using MIDA model", *MEDICAL & BIOLOGICAL ENGINEERING & COMPUTING*, 2017. Under review

1.5.2 Publications in International Conferences

[AS7] **A. M. Samoudi**, K. Van Audenhaege, G. Vermeeren, M. Poole, L. Martens, R. Van Holen, and W. Joseph, "Temporal analysis of Z-Gradient coil eddy currents in tungsten collimator with different resistivities for SPECT/MRI", *EJNMMI Physics*, vol. 1(Suppl. 1), page:A22, 2014.

[AS8] **A. M. Samoudi**, K. Van Audenhaege, G. Vermeeren, M. Poole, L. Martens, R. Van Holen, and W. Joseph, "Influence of collimator insertion on Eddy currents for different resistivities of Tungsten", *Joint Annual meeting ISMRM-ESMRMB*, page:2545, 2014.

[AS9] **A. M. Samoudi**, K. Van Audenhaege, G. Vermeeren, E. Tanghe, L. Martens, R. Van Holen, and W. Joseph, "Analysis and reduction of Eddy current effects induced by tesseral end zonal gradient coils in different collimator geometries for SPECT/MRI integration", *EJNMMI Physics*, vol. 2(Suppl. 1), page:A51, 2015.

[AS10] **A. M. Samoudi**, K. Van Audenhaege, G. Vermeeren, E. Tanghe, L. Martens, R. Van Holen, and W. Joseph, "Compatibility of metal additive manufactured tungsten collimator for SPECT/MRI integration", *EJNMMI Physics*, vol. 2(Suppl. 1), page:A52, 2015.

[AS11] **A. M. Samoudi**, S. Kampusch, E. Tanghe, JC. Szeles, L. Martens, E. Kaniusas, and W. Joseph, "Neural simulation for auricular vagus nerve stimulation", *38th Annual International Conference of the IEEE Engineering in Medicine and Biology Society*, 2016.

[AS12] **A. M. Samoudi**, S. Kampusch, E. Tanghe, JC. Szeles, L. Martens, E. Kaniusas, and W. Joseph, "Percutaneous Auricular Vagus Nerve Stimulation: assessment of sensitivity of neural activation to electrode position", *39th*

Annual International Conference of the IEEE Engineering in Medicine and Biology Society, 2017.

1.5.3 Other Publications

[AS13] **A. M. Samoudi**, E. Tanghe, S. Kampusch, JC. Szeles, L. Martens, E. Kaniusas, and W. Joseph, "Neural Simulation for Auricular Vagus Nerve Stimulation", *COST BM1309 Meeting & Workshop on Verification, Validation and Uncertainty Assessment in Medical EMF Applications, Prague, Czech Republic*, 2015.

[AS14] **A. M. Samoudi**, E. Tanghe, S. Kampusch, JC. Szeles, L. Martens, E. Kaniusas, and W. Joseph, "Numerical modelling of percutaneous auricular vagus nerve stimulation: Assessment of sensitivity of neural activation to electrode position", *COST BM1309 Meeting & Workshop on Vagus Nerve Stimulation, Warsaw, Poland*, 2017.

[AS15] E. Tanghe, **A. M. Samoudi**, S. Kampusch, JC. Szeles, L. Martens, E. Kaniusas, and W. Joseph, "Numerical modelling of percutaneous auricular vagus nerve stimulation: Investigation of the percentage of activated axons using different stimulation patterns.", *COST BM1309 Meeting & Workshop on Vagus Nerve Stimulation, Warsaw, Poland*, 2017.

[AS16] **A. M. Samoudi**, E. Tanghe, S. Kampusch, JC. Szeles, L. Martens, E. Kaniusas, and W. Joseph, "Percutaneous Auricular Vagus Nerve Stimulation: Sensitivity Assessment of the Numerical Model", *COST BM1309 Meeting & Workshop on Vagus Nerve Stimulation, Vienna, Austria*, 2017.

Bibliography

[1] Michael Poole and Richard Bowtell. *Novel gradient coils designed using a boundary element method*. Concepts in Magnetic Resonance Part B: Magnetic Resonance Engineering, 31(3):162–175, 2007.

[2] Siemens. *www.healthcare.siemens.com*. 2017.

[3] Fogelman. *Radionuclide and Hybrid Bone Imaging*. Springer-Verlag, 2012.

[4] Steven R. Meikle, Peter Kench, Michael Kassiou, and Richard B. Banati. *Small animal SPECT and its place in the matrix of molecular imaging technologies*, 2005.

[5] Karel Deprez, Stefaan Vandenberghe, Karen Van Audenhaege, Jonas Van Vaerenbergh, and Roel Van Holen. *Rapid additive manufacturing of MR compatible multipinhole collimators with selective laser melting of tungsten powder*. Medical Physics, 40(1):012501, 2012.

[6] Liang Cai and Ling Jian Meng. *Hybrid pixel-waveform CdTe/CZT detector for use in an ultrahigh resolution MRI compatible SPECT system*. Nuclear Instruments and Methods in Physics Research, Section A: Accelerators, Spectrometers, Detectors and Associated Equipment, 702:101–103, 2013.

[7] Simon R. Cherry. *Multimodality Imaging: Beyond PET/CT and SPECT/CT*, 2009.

[8] H Zaidi, N Ojha, M Morich, J Griesmer, Z Hu, P Maniawski, O Ratib, D Izquierdo-Garcia, Z A Fayad, and L Shao. *Design and performance evaluation of a whole-body Ingenuity TF PETâĂŞMRI system*. Physics in Medicine and Biology, 56(10):3091–3106, 2011.

[9] G. Delso, S. Furst, B. Jakoby, R. Ladebeck, C. Ganter, S. G. Nekolla, M. Schwaiger, and S. I. Ziegler. *Performance Measurements of the Siemens mMR Integrated Whole-Body PET/MR Scanner*. Journal of Nuclear Medicine, 52(12):1914–1922, 2011.

[10] Harald H. Quick. *Integrated PET/MR*. Journal of Magnetic Resonance Imaging, 39(2):243–258, 2014.

[11] A. Drzezga, M. Souvatzoglou, M. Eiber, A. J. Beer, S. Furst, A. Martinez-Moller, S. G. Nekolla, S. Ziegler, C. Ganter, E. J. Rummeny, and M. Schwaiger. *First Clinical Experience with Integrated Whole-Body PET/MR: Comparison to PET/CT in Patients with Oncologic Diagnoses*. Journal of Nuclear Medicine, 53(6):845–855, 2012.

[12] Nina F. Schwenzer, Christina Schraml, Mark Müller, Cornelia Brendle, Alexander Sauter, Werner Spengler, Anna C. Pfannenberg, Claus D. Claussen, and Holger Schmidt. *Pulmonary Lesion Assessment: Comparison of Whole-Body Hybrid MR/PET and PET/CT ImagingâĂŤPilot Study*. Radiology, 264(2):551–558, 2012.

[13] Lell M Quick HH, von Gall C, Zeilinger M, Wiesmüller M, Braun H, Ziegler S, Kuwert T, Uder M, Dörfler A, Kalender WA. *Integrated whole-body PET/MR hybrid imaging: clinical experience*. Invest Radiol, 48(5):280–289, 2013.

[14] Mediso Medical Imaging Systems. *www.mediso.com*. 2017.

[15] MRSolutions. *www.mrsolutions.com*. 2017.

[16] Michael A. Morich, David A. Lampman, Wayne R. Dannels, and Frederick T D Goldie. *Exact temporal eddy current compensation in magnetic resonance imaging systems.* IEEE Transactions on Medical Imaging, 7(3):247–254, 1988.

[17] Stuart Crozier, Craig D. Eccles, Frank A. Beckey, James Field, and David M. Doddrell. *Correction of eddy-current-induced B0 shifts by receiver reference-phase modulation*. Journal of Magnetic Resonance (1969), 97(3):661–665, 1992.

[18] P. Jehenson, M. Westphal, and N. Schuff. *Analytical method for the compensation of eddy-current effects induced by pulsed magnetic field gradients in NMR systems*. Journal of Magnetic Resonance (1969), 90(2):264–278, 1990.

[19] William A. Edelstein, Tesfaye K. Kidane, Victor Taracila, Tanvir N. Baig, Timothy P. Eagan, Yu Chung N Cheng, Robert W. Brown, and John A. Mallick. *Active-passive gradient shielding for MRI acoustic noise reduction*. Magnetic Resonance in Medicine, 53(5):1013–1017, 2005.

[20] P. Mansfield and B. Chapman. *Active magnetic screening of gradient coils in NMR imaging*. Journal of Magnetic Resonance (1969), 66(3):573–576, 1986.

[21] R Turner and R M Bowley. *Passive screening of switched magnetic field gradients*. Journal of Physics E: Scientific Instruments, 19:876–879, 2000.

[22] Hector Sanchez Lopez, Michael Poole, and Stuart Crozier. *Evaluating passively shielded gradient coil configurations for optimal eddy current compensation*. Journal of Physics D: Applied Physics, 43(19):195005, 2010.

[23] Tesfaye K. Kidane, William A. Edelstein, Timothy P. Eagan, Victor Taracila, Tanvir N. Baig, Yu Chung N Cheng, and Robert W. Brown. *Active-passive shielding for MRI acoustic noise reduction: Network analysis*. IEEE Transactions on Magnetics, 42(12):3854–3860, 2006.

[24] R. Bowtell and P. Mansfield. *Gradient coil design using active magnetic screening*. Magnetic Resonance in Medicine, 17(1):15–21, 1991.

[25] Takao Takahashi. *Numerical analysis of eddy current problems involving z gradient coils in superconducting MRI magnets*. IEEE Transactions on Magnetics, 26(2):893–896, 1990.

[26] Adnan Trakic, Hua Wang, Feng Liu, H.S. Lopez, and Stuart Crozier. *Analysis of transient eddy currents in MRI using a cylindrical FDTD method*. IEEE Transactions on Applied Superconductivity, 16(3):1924–1936, 2006.

[27] Feng Liu and Stuart Crozier. *An FDTD model for calculation of gradient-induced eddy currents in MRI system*. IEEE Transactions on Applied Superconductivity, 14(3):1883–1889, 2004.

[28] *IEC (Edition 3.0 2010) 60601-2-33 Medical electrical equipment - Part 2-33: Particular requirements for the basic safety and essential performance of magnetic resonance equipment for medical diagnosis)*.

[29] ICNIRP. *Medical magnetic resonance (MR) procedures: protection of patients*. Health physics, 87:197–216, 2004.

[30] *IEEE standard for safety levels with respect to human exposure to electromagnetic fields, 0-3 kHz, C95.6-2002, New York: Institute of Electrical and Electronics Engineers; 2002:43)*.

[31] Martin Bencsik, Richard Bowtell, and Roger M. Bowley. *Using the vector potential in evaluating the likelihood of peripheral nerve stimulation due to switched magnetic field gradients*. Magnetic Resonance in Medicine, 50(2):405–410, 2003.

[32] L K Forbes and S Crozier. *On a possible mechanism for peripheral nerve stimulation during magnetic resonance imaging scans.* Physics in medicine and biology, 46(2):591–608, 2001.

[33] Weihua Mao, Blaine A. Chronik, Rebecca E. Feldman, Michael B. Smith, and Christopher M. Collins. *Consideration of magnetically-induced and conservative electric fields within a loaded gradient coil*. Magnetic Resonance in Medicine, 55(6):1424–1432, 2006.

[34] Huawei Zhao, Stuart Crozier, and Feng Liu. *Finite difference time domain (FDTD) method for modeling the effect of switched gradients on the human body in MRI.* Magnetic resonance in medicine : official journal of the Society of Magnetic Resonance in Medicine / Society of Magnetic Resonance in Medicine, 48(6):1037–42, 2002.

[35] O Heid inventor. *Siemens Aktiengesellschaft, assignee. Magnetic resonance apparatus with compensation of fields arising due to eddy currents*. US patent 6844733 B2, January 18, 2005.

[36] Gernot Schmid, Stefan Cecil, and Richard Überbacher. *The role of skin conductivity in a low frequency exposure assessment for peripheral nerve tissue according to the ICNIRP 2010 guidelines*. Physics in Medicine and Biology, 58(13):4703–16, 2013.

[37] E. N. Marieb and K. Hoehn. *Human anatomy and physiology (9th ed.) Glenview: Pearson*. 2013.

[38] M S Evans, S Verma-Ahuja, D K Naritku, and J A Espinosa. *Intraoperative human vagus nerve compound action potentials*. Acta Neurol Scand, 110:232–238, 2004.

[39] D McNeal. *Analysis of a Model for Excitation of Myelinated Nerve*. IEEE Transactions on Biomedical Engineering, BME-23(4):329–337, 1976.

[40] J Reilly and W Larkin. *Understanding transient electric shock*. Johns Hopkins APL Tech. Digest, 5(3):296–304, 1984.

[41] S. Silva, P. J. Basser, and P. C. Miranda. *Elucidating the mechanisms and loci of neuronal excitation by transcranial magnetic stimulation using a finite element model of a cortical sulcus*. Clinical Neurophysiology, 119(10):2405–2413, 2008.

[42] B J Roth. *Mechanisms for electrical stimulation of excitable tissue*. Critical Reviews in Biomedical Engineering, 22(3-4):253–305, 1994.

[43] J Reilly and A Diamant. *Electrostimulation-Theory Applications and and Computational Model*. Artech House, 2011.

[44] D Groves and V Brown. *Vagal nerve stimulation: a review of its applications and potential mechanisms that mediate its clinical effects*. Neuroscience and Biobehavioral Reviews, 29(3):493 – 500, 2005.

[45] G De Ferrari, H Crijns, and M Borggrefe et al. *Chronic vagus nerve stimulation: a new and promising therapeutic approach for chronic heart failure*. European Heart Journal, 32(7):847–855, 2011.

[46] A Zamotrinsky, B Kondratiev, and J de Jong. *Vagal neurostimulation in patients with coronary artery disease*. Autonomic Neuroscience, 88(1-2):109–116, 2001.

[47] Robert H. Howland. *Vagus Nerve Stimulation*. Current Behavioral Neuroscience Reports, 1(2):64–73, 2014.

[48] J Ellrich. *Transcutaneous Vagus Nerve Stimulation*. European Neurological Review, 6(4):254, 2011.

[49] S Kampusch, E Kaniusas, and J Szeles. *New Approaches in Multi-Punctual Percutaneous Stimulation of the Auricular Vagus Nerve*. Proceedings of the 6th International IEEE EMBS Conference on Neural Engineering, pages 263–266, 2013.

[50] S Sator-Katzenschlager, J Szeles, G Scharbert, A Michalek-Sauberer, A Kober, G Heinze, and S Kozek-Langenecker. *Electrical Stimulation of Auricular Acupuncture Points Is More Effective Than Conventional Manual Auricular Acupuncture in Chronic Cervical Pain: A Pilot Study*. Anesthesia and Analgesia, pages 1469–1473, 2003.

[51] T Payrits et al. *Vagal stimulation - a new possibility for conservative treatment of peripheral arterial occlusion disease.* Zentralblatt fÃijr Chirurgie, 136:431–435, 2011.

[52] X Gao, S Zhang, B Zhu, and H Zhang. *Investigation of specificity of auricular acupuncture points in regulation of autonomic function in anesthetized rats*. Autonomic Neuroscience, 138(1-2):50–56, 2008.

[53] A M Samoudi, G Vermeeren, E Tanghe, R Van Holen, L Martens, and W Josephs. *Numerically simulated exposure of children and adults to pulsed gradient fields in MRI*. J. Magn. Reson. Imaging, 44:1360–1367, 2016.

[54] M De Lucia, K Embleton G Parker, J Newton, and V Walsh. *Diffusion tensor MRI-based estimation of the influence of brain tissue anisotropy on the effects of transcranial magnetic stimulation*. Neuroimage, 36(4):1159–1170, 2007.

[55] S Miocinovic. *Computational Analysis of Subthalamic Nucleus and Lenticular Fasciculus Activation During Therapeutic Deep Brain Stimulation*. Journal Of Neurophysiology, 96(3):1569–1580, 2006.

[56] C Schmidt and U Van Rienen. *Modeling the Field Distribution in Deep Brain Stimulation: The Influence of Anisotropy of Brain Tissue*. IEEE Transactions On Biomedical Engineering, 59(6):1583–1592, 2012.

[57] S M Danner et al. *Potential distribution and nerve fiber responses in transcutaneous lumbosacral spinal cord stimulation. Int*. In Int. Conference on Advancements of Medicine and Health Care through Technology; IFBME 44, pages 203–208, 2014.

Part I

Induced Eddy Currents in SPECT/MRI

2

EM Modelling and Characterization of Eddy Currents Induced by Gradient Coils for SPECT/MRI

2.1 Introduction

Medical imaging technology is shifting from single to multimodality imaging. Single-photon emission computed tomography (SPECT) and MRI each have their respective advantages and limitations. Combining these two technologies in a synergistic manner would allow researchers to exploit the strengths of both techniques. SPECT can provide insight into a wide range of biological processes. However, its relatively poor spatial resolution can make unambiguous localization of the probes extremely difficult, especially when the images lack significant anatomical detail for reference [1]. In contrast to SPECT, MRI can provide exceptionally high spatial resolution anatomical information as well as localized chemical and physical information such as metabolite concentrations and water diffusion characteristics.

Although combined PET and MRI is rapidly gaining popularity, no commercial systems for combining SPECT and ultrahigh-field MRI have been developed. Goetz et al. [2] used a strategy similar to PET/CT systems in which a small animal SPECT system was brought in close proximity to a separate low field (0.1T) MRI system for coregistered imaging. Because the investigators performed sequential SPECT and MRI, their technique cannot be qualified as a truly integrated multimodality system with simultaneous data acquisition. Furthermore, the use of a low

magnetic field is suboptimal and obvious given the state of the art of the ultrahigh-field MRI system presently available.

Although the integration of SPECT and MRI for simultaneous data acquisition offers numerous advantages and new opportunities, it also presents many technological challenges. One of these challenges is the presence of eddy currents in the collimator due to the pulsed magnetic field gradients. MRI techniques combine pulsed magnetic field gradients with frequency-selective RF pulses to achieve spatial localization of the nuclear MR signal [3]; in these approaches, the currents flowing in three gradient coils are rapidly switched on/off to encode the spatial position of the nuclear MR active nuclei by a linear spatial variation of the gradient field along the x, y, and z coordinates. However, according to Faraday's law, any time-varying magnetic field results in an eddy current in a conducting object. Therefore, this rapid switching of gradient coils induces spatially and temporally varying eddy currents within the conducting structures of the MRI scanner and in the collimator required for SPECT, which typically has a high conductivity. The undesired magnetic field produced by these eddy currents opposes and distorts the linear gradient fields in the region of interest, which results in image artifacts [4–6]. Other effects concern the thermal load in the cryostat of the superconducting magnet, which may lead to increased boil-off of the cryogens (can even cause magnetic quenching in extreme cases) and acoustic noise due to their interaction with the B_0 field [7].

2.1.1 Related Works

Hamamura et al. [1] developed a miniaturized dual-modality SPECT/MRI system and demonstrated the feasibility of simultaneous SPECT and MRI data acquisition. A cadmium zinc telluride nuclear radiation detector was interfaced with a specialized radiofrequency (RF) coil and placed within a whole body 4T MRI system. Their work can be considered as a feasibility study with simplified models to proof the possibility of simultaneous acquisition of SPECT and MRI data. Cai et al. [8] presented a stationary, MR-compatible small animal SPECT system development and preliminary imaging performance. Their system is based on 20 second-generation energy-resolved photon-counting CdTe detectors. Each detector is associated with four pinholes on average. Another SPECT/MRI project is the INSERT (integrated SPECT/MRI for enhanced stratification in radio-chemotherapy) [9] dedicated to develop a custom SPECT apparatus that can be used as an insert for commercially available MRI systems (e.g., 3T MRI with a 59 cm bore diameter). Two SPECT prototypes will be developed: one dedicated to preclinical imaging, another dedicated to clinical imaging. Finally, Mediso Medical Imaging Systems [10] was the first to market an in-line, whole

body, preclinical SPECT/MRI system (nanoScan SPECT/MRI), with a 1T permanent magnet, 450 mT/m gradient strength, up to 200 x 250 mm reconstructed field of view (FOV) and 275 mm spatial resolution for SPECT components.
Although many approaches have been proposed to minimize the generation of eddy currents [e.g., active and passive shielding coils [11–15], current pulse preemphasis [4, 6, 16], less conductive magnet bore materials and alternative cryostat configurations [17–20]], significant distortions will often remain, mainly in the short time interval after the gradient is switched off. This is particularly the case in the presence of highly conductive objects, where eddy currents are characterized by long time constants [6].

Simulating eddy currents in conducting objects is particularly computationally intensive. Several numerical approaches have been proposed to deal with this problem. These methods propose an efficient computer modeling tool that would reduce the experimental efforts during prototyping and development of pre-clinical SPECT/MRI or PET/MRI systems. Differential methods such as finite element method [18, 21] and finite difference time domain (FDTD) were proposed and adapted to simulate eddy currents. Trakic et al. [22] developed a three-dimensional FDTD method in cylindrical coordinates for the modeling of low-frequency transient eddy currents in MRI as an extension of the work of Liu et al. [23]. Integral methods, such as, the boundary element method [24] or the method of moments, only require the discretization of the active parts, neglecting the surrounding air and introducing a correct far boundary condition. Their formulations typically give rise to fully populated matrices, meaning that the storage requirements and computational time will typically grow linearly with the geometry and the required solution frequency [25]. Another integral method, the network method, has been applied in the analysis of the currents induced by axially symmetric coils (e.g., z-gradient) in a realistic cryostat [7, 14, 17], and even coupled in Fourier space to accurately evaluate the currents induced by coils of arbitrary geometry in cylindrical coordinates [20, 26].

2.1.2 Objective

The goal of this chapter is to use numerical models to study different designs of tungsten collimators for preclinical SPECT/MRI and the eddy currents in these collimators due to x-, y-, and z-gradient coils for different arrangements of tungsten collimators. To this end, an x-, y-, and z-gradient coil for preclinical systems [27] has been simulated with the collimators using FEKO [25]. Section 2.2 presents a model of the eddy current approximated as inductive-resistive circuits. In Section 2.3, the simulation platform, MRI gradient coils, and collimator model are described with an experimental validation of the numerical settings. Section

2.5 is dedicated to the characterization of the induced eddy current in the longitudinal and the transverse MRI coils. In Section 2.6, we investigated different arrangements of the collimators using hexagonal and pentagonal geometry with gaps. Conclusions are drawn in Section 2.7.

2.2 Theory: Eddy Current Model

The conducting structures that support the eddy currents are approximated as inductive-resistive circuits. Mutual inductance between the gradient coil and conducting structures allows currents to be induced by the gradient coil [3]. A straightforward analysis of this model approximates the eddy current as a superposition of multiple exponential decay terms as a Taylor expansion of the eddy currents [6]. According to previously described quasi-static eddy current models [4], the temporal behavior of the eddy current field $G_e(t)$ induced by a nominal gradient waveform $G(t)$ can be described as

$$G_e(t) = -\frac{dG(t)}{dt} \otimes H(t) \tag{2.1}$$

where $H(t)$ represents the eddy current impulse response function and $dG(t)/dt$ the time derivative of $G(t)$. $\otimes$ is the convolution operator

The eddy current impulse response $H(t)$ is given by a sum of decaying exponentials, characterized by amplitude constants α_n (which depend on the inductance and the mutual inductance of the n^{th} coupled eddy current mode with the gradient coil) and time constants τ_n (which depend on the resistance and the inductance of the n^{th} coupled eddy current mode) as follows

$$H(t) = u(t) \sum_{n=0}^{N-1} \alpha_n e^{-t/\tau_n} \tag{2.2}$$

where $u(t)$ is the unit step function and N the number of exponential terms.

2.3 Materials and Methods

2.3.1 Simulation Platform

The gradient coils and collimators were modeled with FEKO, a three dimensional, full-wave electromagnetic simulation platform based on the method of moments (MoM). FEKO uses the method of moments, which provides full-wave solutions of Maxwell's integral equations in the frequency domain. We activated the low-frequency stabilization and used the volume equivalence principle for meshing the collimator. The volume equivalence principle allowed the creation of dielectric bodies from cuboids or tetrahedrals, and it is advantageous for low-frequency

simulations [25].

FEKO provided time analysis functionality, allowing electromagnetic problems to be analyzed in the time domain. The relevant computations were performed in the frequency domain, and fast Fourier transform algorithms were used to transform the data to the time domain. First, we extracted frequency components of the gradient pulse by applying fast Fourier transform. We then performed a broadband simulation covering the frequency range of the gradient shape. The output was then postprocessed with FEKO time domain analysis to extract the time response of the system, based on the gradient pulse.

2.3.2 MRI Gradient Coils

The system under investigation consisted of x, y, and z gradient coils for preclinical systems and a SPECT collimator made of tungsten. Figure 2.1 shows the gradient coils, and Table 2.1 lists its properties and configurations. The setup was simulated with a broadband simulation from 0 to 10 kHz with a step of 400 Hz to cover the frequency range of a sinusoidal ramp from 500 mT/m to 0 mT/m within 0.25 ms. The magnetic field due to eddy currents was calculated by subtracting the z-component of the magnetic induction of the gradient coils without collimator (B_z) from the z-component (main component of the gradient field) of the magnetic induction of the gradient coils with the collimator (B_z^{col}). We then calculated the maximum value within the 3 cm FOV (field of view).

	X coil	Y coil	Z coil
Inner diameter (mm)	100	100	100
Outer diameter (mm)	126	126	128
Length (mm)	293	293	232
Gradient strength (mT/m)	500	500	500
Gradient efficiency (mT/m/A)	2.99	2.99	3.08
Applied current (A)	167.2	167.2	162.3
DSV of 3cm	2.1 %	2.1 %	0.9 %

Table 2.1: Parameters of the transverse and the longitudinal gradient coils. DSV refers to diameter of spherical volume

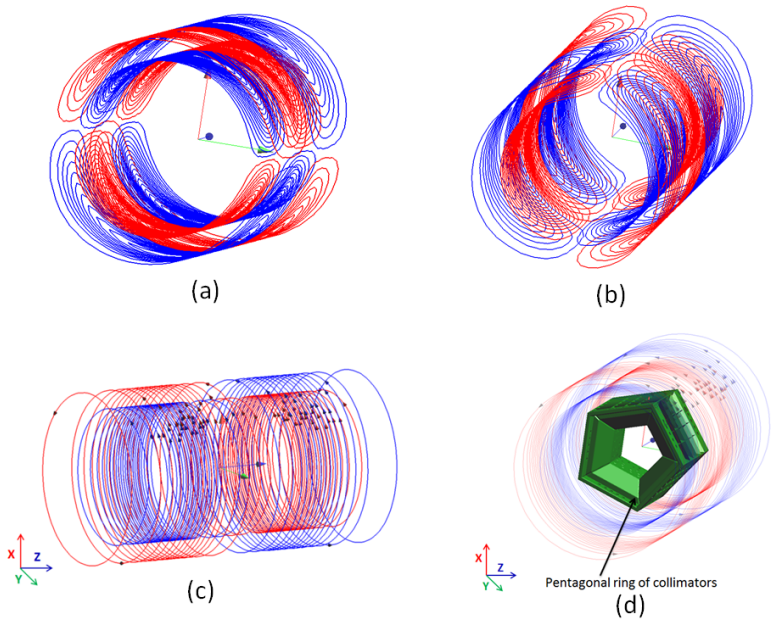

Figure 2.1: a-c: Wire patterns for x-gradient coil (a), y-gradient coil (b), and z-gradient coil (c). d: Pentagonal ring of the collimators centered inside the z-gradient coil. Red and blue colors are used to indicate wires in which there is a different sense of current flow (Source: Poole [27]).

2.3.3 SPECT Collimator

We simulated a full-ring, multi-pinhole collimator that is a part of a new, more compact microSPECT system that is under development. Deprez et al. [28] designed and produced the collimator with 20 loftholes [29] with 500 mm diameter pinhole openings. The density of the collimator was equal to 17.31 $\pm$ 0.10 g/cm^3 (89.92 $\pm$ 0.05 % pure tungsten). The designed multi-lofthole collimator (16 mm thick and 70 x 52 mm^2 transverse size) was sent to the additive manufacturer LayerWise (Leuven, Belgium) (Figure 2.2f). The collimator was built using a direct additive manufacturing technique based on selective laser melting of high-density tungsten powder. Van Holen et al. [30] used this collimator in a pentagonal and hexagonal arrangement to determine the optimal microSPECT system.

2.3.4 Resistivity of the Printed Tungsten

Pure lead has a low susceptibility and conductivity and has shown to be MR-compatible but the density of lead is only 11.34 g/cm^3. This is sufficient for parallel-hole or fan-beam collimators, but in pinholes, this results in high edge penetration and poor resolution. Therefore, pinhole collimators are usually made of tungsten, which has a much higher density (19.25 g/cm^3) but is also very brittle and difficult to machine. Tungsten alloys solve the issue of brittleness but they often contain ferromagnetic components and are therefore not MR compatible [28].

Additive manufacturing is based on the process of melting tungsten powder layer by layer using a laser beam. By adapting the strength of this laser beam, the laser spot size and/or changing the duration of the melting process at each position, it is possible to produce collimators with a lower/higher density [29]. As the material is built up layer by layer, we expect the resistivity to be different for directions parallel and perpendicular to the layers. Therefore, we determined resistivity in three directions. Resistance measurements were performed along different axes (Figure 2.3) with a four-point probe low resistance meter Keithley 6220/2182, which has a precision of 10 $n\Omega$. Four measurements were performed in order to determine resistivity in all directions (Figure 2.3).

2.3.5 Eddy Current Measurements for a Single Collimator

In this section, we will investigate eddy currents induced in a prototype single collimator. For this, distortions in a uniform water phantom were evaluated when a prototype preclinical collimator [32] is placed inside the MR bore of a 7T Bruker Pharmascan 70/16. The collimator was produced using additive manufacturing and had a density of 17.31$\pm$ 0.10 g/cm^3 (89.92 $\pm$ 0.05 % of pure tungsten). T1, T2 and T2* images were recorded using a RARE , FLASH -T2 and FLASH -T2*

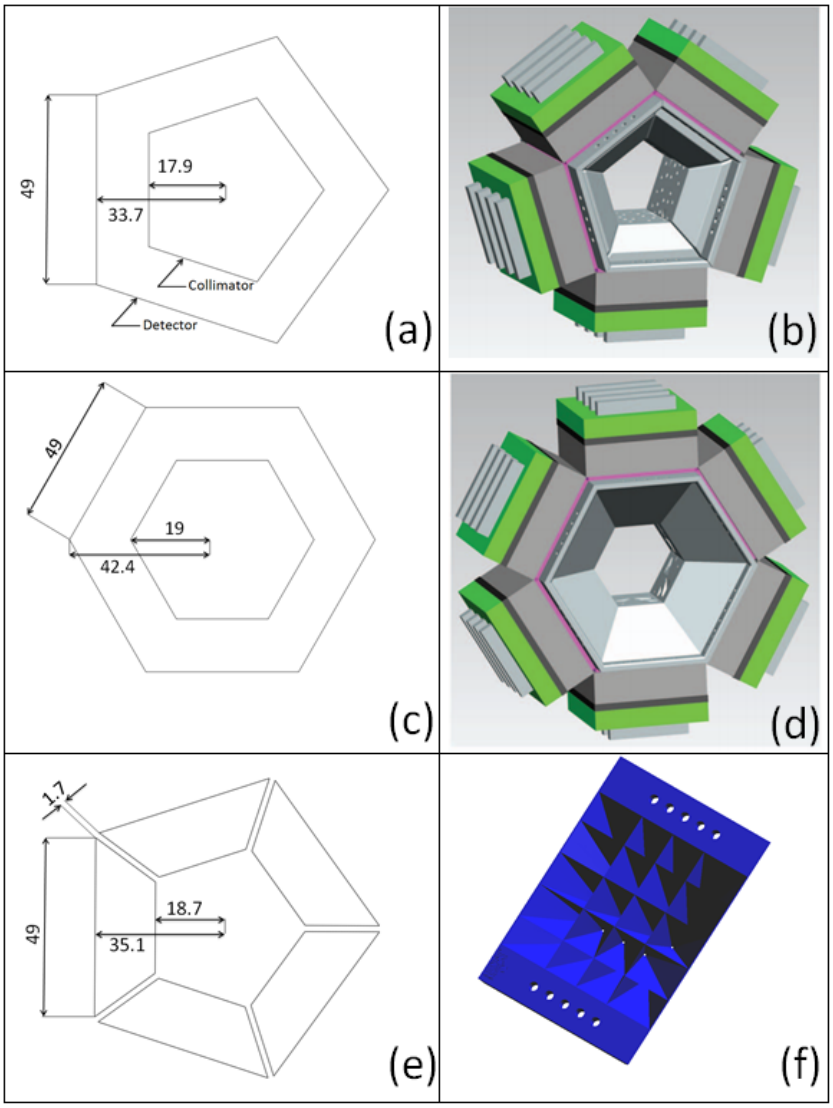

Figure 2.2: Simulated collimators system geometry definition. a, c: Pentagonal and hexagonal arrangements, respectively (dimensions are in mm). b, d: Rendering of the respective SPECT systems. Centrally, the multipinhole collimators are shown, followed by the scintillator, Photomultiplier tube, and electronics. e: Pentagonal geometry with gap of 1.7 mm between the collimators. f: Design of the collimator [28].

sequence, respectively, and using a volume transmit coil (Part No. T1123V3) and a rat brain surface receive coil (Part No. T11425V3) [29].

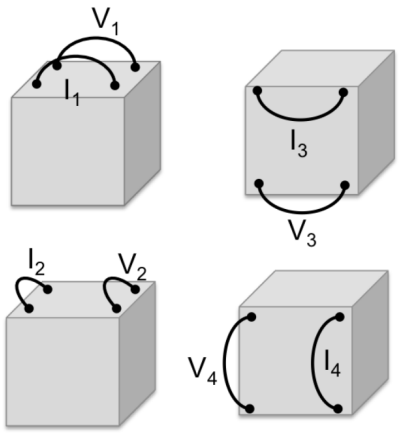

Figure 2.3: Resistance measurement setup in four directions (source: Van Audenhaege [31]).

Images were acquired with and without the collimator on top of the receiver coil (Figure 2.4) and compared based on their line profile. The effect of shimming was also investigated, which is the adjustment of the magnetic field in case of inhomogeneities, e.g. due to the presence of a ferro-magnetic material. The effect of shimming was measured on a uniform phantom scanned with an echo-planar imaging (EPI) sequence with and without collimator inside a volume transmit/receive coil (Part No. T1123V3). The EPI was used because the sequence is T2* based and typically very sensitive to changes in the magnetic field. Firstly, measurements were performed without the collimator. Secondly, measurements were performed with the collimator and lastly, shimming was realized before measuring again with the collimator using the Bruker second order local MAPSHIM, which is based on the minimization of the B_0 field map variation.

2.3.6 Experimental Validation of the Numerical Settings

2.3.6.1 Measurements

To validate the simulations, we performed measurements on a 7T preclinical MRI from Bruker Pharmascan with a volume coil (part no. T1123V3) and a rat brain surface receiver coil (part no. T11425V3). We measured eddy currents due to a 25 x 10 x 40 mm^3 block of lead with a resistivity of 186.43 $n\Omega m$. The block was inserted in the MR bore (at position x = 20.5, y = 0, and z = 2 mm on top of the receiver coil) together with a spherical phantom with an inner diameter of 12.24 mm, filled with $CuSO_4$ (1 g/L) in H_2O (CAS nr: 7758-99-8) with an electrical conductivity of 0.057 S/m.

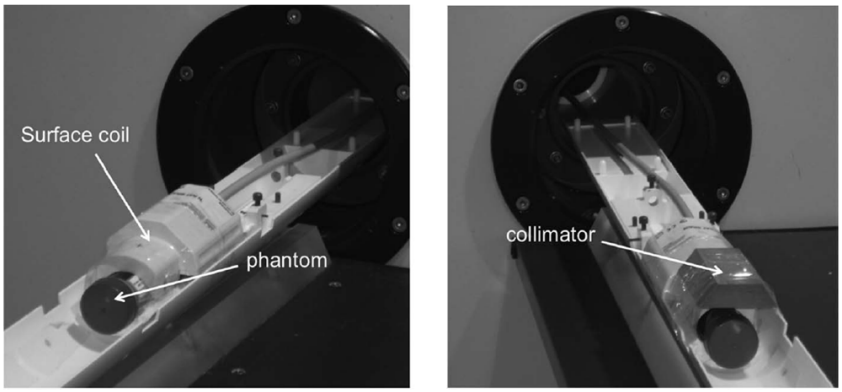

Figure 2.4: Measuring a uniform phantom in a 7T MRI with and without collimator (source: Deprez [29])

Measurements were performed with the phantom positioned at different locations along the z-axis (x = 0.35 mm and y = 0.23 mm) and with the sequence shown in Figure 2.5. We applied a z-gradient with a peak value of 119.35 mT/m (applied for 500 ms) and a sinusoidal ramp up and down (both with duration of 248 μs). Immediately after the ramp-down, we acquired the free induction decay signal, whose phase relates to the magnetization as follows [33]:

$$\phi(t) = \gamma \int_0^t B_e(x)dx + \phi_0 \tag{2.3}$$

where $\phi(t)$ is the phase of the free induction decay, γ is the gyromagnetic ratio (267.513 rad/s/T for protons), B_e is the magnetic field induced by the eddy currents in the lead block, and ϕ_0 is a constant phase offset due to main field inhomogeneities. To cancel out the constant offset, we acquired the free induction decay after both a positive and a negative gradient:

$$\phi_T(t) = \frac{\phi_+(t) - \phi_-(t)}{2} = \gamma \int_0^t B_e(x)dx \tag{2.4}$$

The magnetic field due to eddy currents was then retrieved by differentiating the phase:

$$B_e(t) = \frac{1}{\gamma}\frac{d\phi_T(t)}{dt} \tag{2.5}$$

We performed these measurements both with and without the lead block insert and for different locations of the phantom. We did not modify the pre-emphasis settings of the MRI system.

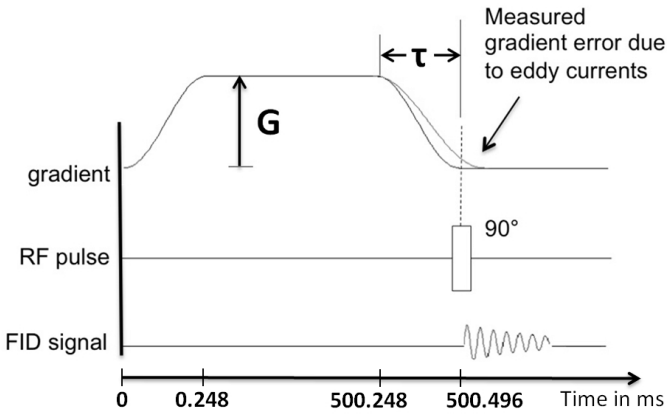

Figure 2.5: Pulse sequence used for the measurement of eddy currents. G is the gradient strength and τ the ramp-down time. The induced magnetic field is taken after completely switching off the gradient field.

2.3.6.2 Simulations

To validate simulations with the configuration of measurements, we considered a z-gradient coil, a representation of the phantom and the RF coil, and a cuboid representing the lead block. The phantom was modeled as a sphere of diameter 12.24 mm with electrical conductivity of the $CuSO_4$ - $5H_2O$, σ = 0.057 S/m. The RF coil was modeled as a half cylinder (central axis = z-axis, diameter = 37.5 mm, height = 80 mm, thickness = 5 mm) with a perfect electric conductor medium (a zero-resistance conductor). The lead block was represented by a cuboid of dimensions 25 x 10 x 40 mm^3 and electrical resistivity r = 186.43 $n\Omega m$. The simulated gradient ramp has a sinusoidal shape with a ramp-down time of 248 μs and a gradient strength G = 119.35 mT/m to match the gradient applied in measurements.

Figure 2.6 shows a representation of the described configuration. To determine the magnetic field due to eddy currents from the simulations, we first extracted the z-component of the magnetic induction B from both simulations (with and without the lead block), then compared the two components to quantify the additional magnetic field due to the lead insertion.

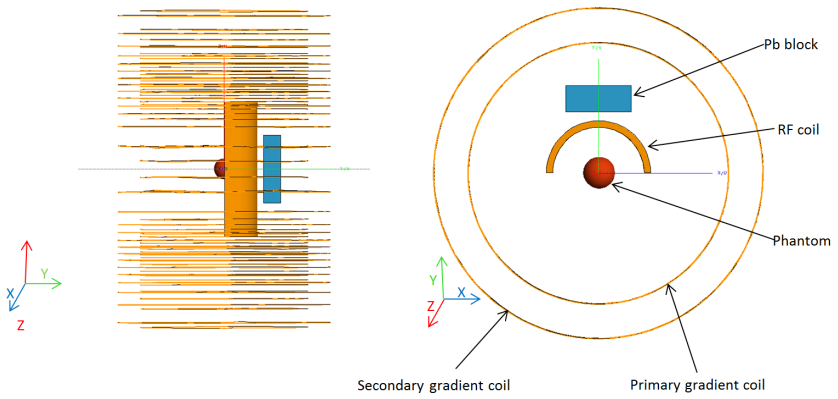

Figure 2.6: Experimental setup used to validate simulations. The gradient system consists of a shielded z-gradient coil. The phantom is modeled by a sphere of diameter 12.24 mm. The RF coil is modeled as a half cylinder (central axis = z-axis, diameter = 37.5 mm, height = 80 mm, thickness = 5 mm). A cuboid of dimensions 25 x 10 x 40 mm^3 represents the lead (Pb) block.

2.4 Measurement Results and Validation of the Simulations

2.4.1 Measured Resistivity of the Tungsten

The measured resistance values are shown in Figure 2.7 and then converted to resistivity values (from Van Audenhaege [31]). Figure 2.8 shows that the resistivity was highest in the direction parallel to the layers (310 to 360 $n\Omega$.m) and lowest in the direction perpendicular to the layers (158 to 78 $n\Omega$.m). The higher resistivity in the parallel layers can be explained by the long micro-cracks in these layers, which are a result of the high temperature that is needed to melt the tungsten powder and the fast cooling down afterwards. The micro-cracks also explain why it is challenging to achieve a density of 100 %: the stronger the laser, the higher the density should theoretically be, but the higher the risk for micro-cracks. These micro-cracks are usually not desired as they decrease the strength of the material, but in the context of MR-compatibility and decreasing eddy currents they appear to be advantageous and help to increase resistivity. In conclusion, all resistivity values are higher than the resistivity of solid tungsten (56 $n\Omega$.m), which is in line with the expected value.

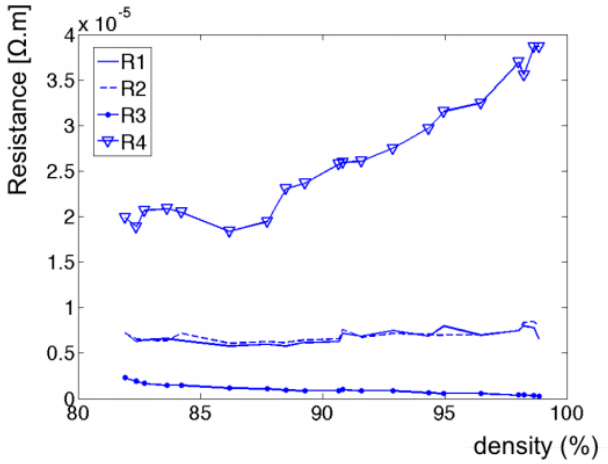

Figure 2.7: Resistance in function of density in four directions as depicted on Figure 2.3 (source: Van Audenhaege [31]).

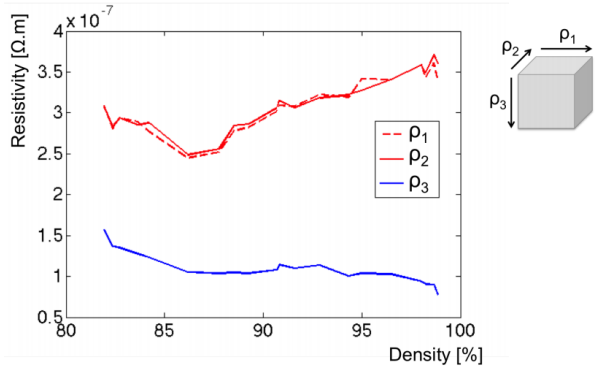

Figure 2.8: Resistivity as a function of density for three directions: ρ_1 is the direction perpendicular to the layers and ρ_2 and ρ_3 are the directions parallel to the layers (source: Van Audenhaege [31]).

2.4.2 Measured Eddy current for Single Collimator

The resulting T1, T2 and T2* images of the uniform phantom are shown in Figure 2.9. The decrease in sensitivity (in the vertical direction) is due to the properties of the receiver coil (which is a surface coil) and is normal. The deviation due to the presence of the collimator is best observed in the line profiles. The differences are very limited except for the T2* sequence, which is typically more sensitive to disturbances. The effect of shimming is shown in Figure 2.10. A small image deformation (squeezing) can be noticed when the collimator is inserted in

the bore (Figure 2.10d). This deformation can be almost completely removed by shimming after inserting the collimator in the bore (Figure 2.10e).

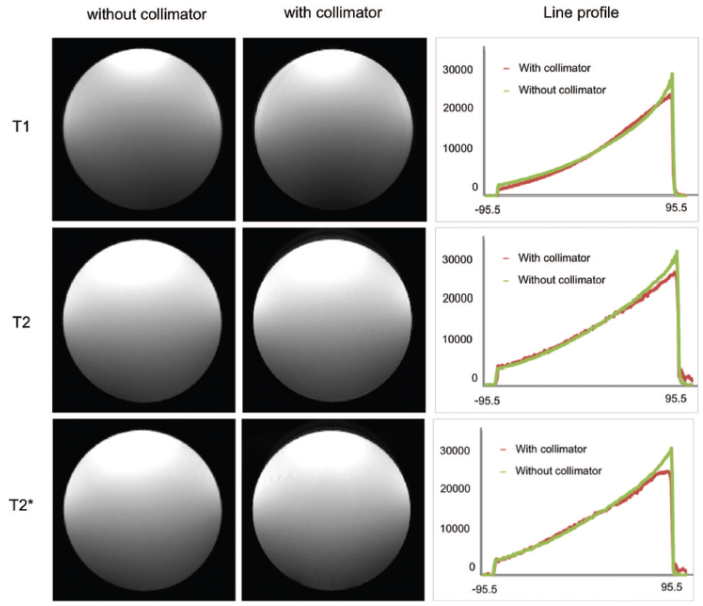

Figure 2.9: Images and line profiles of a uniform phantom with and without collimator (source: Deprez [29]).

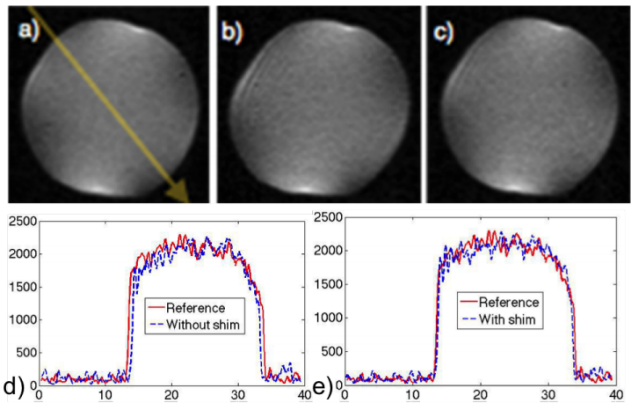

Figure 2.10: EPI image of a uniform phantom a) reference image b) with collimator, no shimming c) with collimator, auto-shim (d,e) line profiles (source: Van Audenhaege [31]).

2.4.3 Validation of the Numerical Model

Measurements were performed after turning off the gradient for 248 ms. Figure 2.11a shows the average value [over a sphere of radius 1 mm, centered at (0.345, 0.23, 2.8) mm] of the magnetic field due to eddy currents for both simulations and measurements. Figure 2.11b shows the difference between measurements and simulations compared with the applied gradient field. The maximum variation between measurement and simulation was <1 % of the applied gradient field. If the eddy currents induce a magnetic field that is >2 % of the gradient field, artifacts will arise [31]. This guideline value of 2 % is experimentally derived during measurements for the SIMRET project [31]. Induced fields due to eddy currents with values less than 2 % of the applied gradient field can be corrected using the shimming mechanism as detailed in Section 2.4.2.

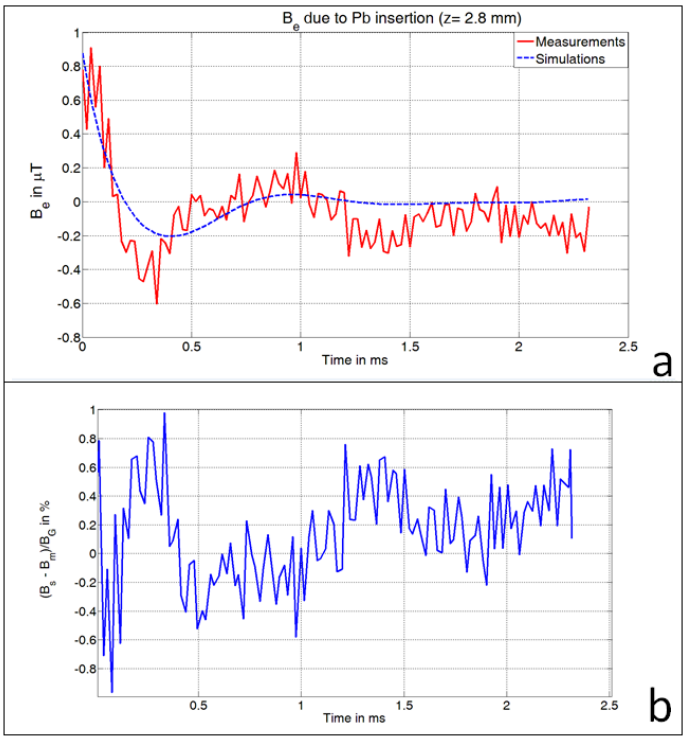

Figure 2.11: Validation of the simulation using the lead block. a: Measured and simulated magnetic induction due to eddy currents B_e. b: Difference between measured and simulated induced field due to lead insertion, compared with the applied gradient field. B_s, B_m, and B_G stand for simulated, measured, and applied magnetic induction, respectively.

2.5 Eddy Currents Characterization for Longitudinal and Transverse coils

Results from the measurements using a single collimator (Figures 2.9 and 2.10) were promising, but these measurements are for a single collimator element, while the final system consists of five or six collimator elements, forming a full ring. As the production of such a full ring is expensive, we investigated the full-ring design based on simulations. In this section, we will investigate and characterize the induced fields for both the longitudinal and transverse coils and we compare results for both coil types. In Section 2.6, we will investigate whether we can further reduce eddy currents by leaving small air gaps between neighboring collimators in the collimator ring or by changing the collimators' arrangement from pentagonal to hexagonal geometry.

Figure 2.12 shows a representation of the gradient field strength for the transverse and longitudinal gradient coils. Figure 2.13 shows the magnetic induction due to eddy currents (B_e) as a percentage of the applied gradient field for longitudinal and transverse gradient coils. The maximum value of the induced magnetic field is 4.66 % and 0.87 % of the applied gradient field (gradient strength = 500 mT/m) for longitudinal and transverse gradient coils, respectively. The applied gradient field is determined at the point in space where the eddy current is being calculated. Thus, the transverse coils induce fewer eddy currents than the longitudinal ones, due to the wire distribution for the two types of the coils and the collimators' position inside the coils. In fact, because gradient fields are along the z direction for both of the coils and increase linearly with the same ratio (G_x = G_y = G_z), the collimator, by its geometry and position, is more exposed to the gradient fields in the longitudinal configuration (Figure 2.12). Figure 2.13 shows that the magnetic field produced by the eddy current changes sign. These relatively small values (the maximum negative value represents 2.71 % of the maximum positive value) is due to competing eddy currents on different surfaces with slightly different time constants.

2.6 Effect of the Collimators' Arrangement Geometry on the Maximum Induced Eddy Currents

In this section, we investigated different arrangements of the collimators using pentagonal geometry with gaps and the hexagonal geometry for the transverse and the longitudinal gradient coils (2.2 shows the considered configurations). Table 2.2 shows the maximum value of B_e (always as a percentage of the applied gradient field) for the three configurations. The hexagonal geometry induces larger eddy currents (maximum induced magnetic field is equal to 6.17 % of the applied

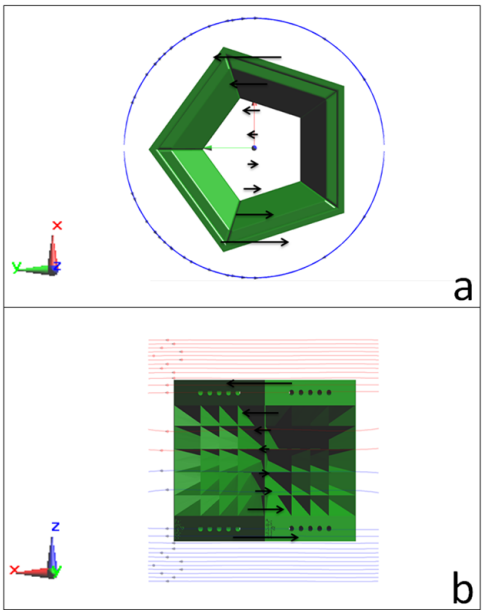

Figure 2.12: Representation of the gradient field strength for (a) the x-gradient coil (transverse gradient coil) (b) and the Z-gradient coil (longitudinal gradient coil) (b). The norm and the direction of the vectors represent the field's strength and sign, respectively.

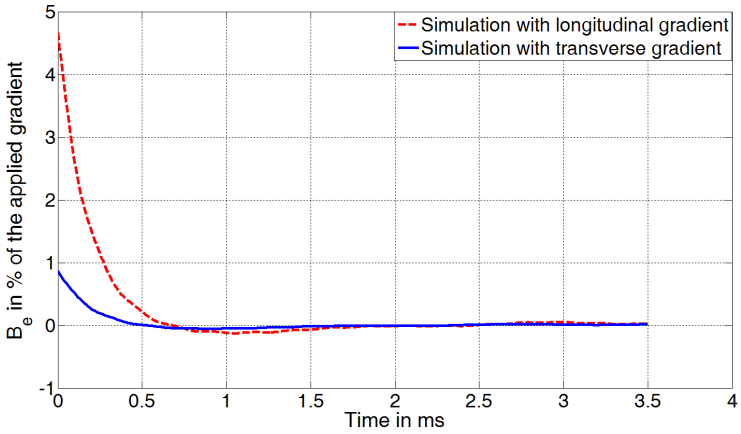

Figure 2.13: B_e in percentage of the applied gradient field of 500 mT/m for both the longitudinal and the transverse gradient coils in averaged a FOV of 3 cm, after switching off the gradient field.

	Pentagon	Pentagon with gaps	Hexagon
Transverse	0.87%	0.43%	0.97%
Longitudinal	4.66%	1.13%	6.17%

Table 2.2: Maximum Induced Magnetic Field as a Percentage of the Applied Gradient Field (G = 500 mT/m, τ =0.25 ms) in an FOV of 3 cm

gradient field, for hexagonal arrangement using longitudinal coil), and by adding relatively small gaps between the collimators (1.7 mm), the maximum value of the induced magnetic field was reduced by 50.6 % and 75.8 % for transverse and longitudinal gradient coils, respectively, bringing back the maximum value of the induced field to <2 % of the applied gradient field. The hexagonal system has a higher sensitivity than the pentagonal one [30] but it induces more eddy currents for both types of gradient coils. This is due to the increase in number of the collimators (six instead of five for the pentagonal arrangement), thus more conductive volume in the hexagonal arrangement. Adding gaps between the collimators can reduce the maximum value of B_e by 75 % (Table 2.2) and brings it to <2 % for all the gradient coils. However, the individual pieces should be electrically isolated; otherwise, the values of 1.13 % and 0.43 % should be revised to include eventual eddy current in the connections between the collimators.

Figure 2.13 and Table 2.2 show that there are still residual eddy currents inducing a spatio-temporal magnetic field, which can be further reduced nowadays using two standard practices. First, pre-emphasis techniques use eddy current models and constants to temporally modify the gradient pulse, in a way that the combination of the nominal gradient field and the induced field produce the desired pulse shape [16]. Second, active shielding, in which a secondary coil surrounding the first is introduced. The wires in this second screening coil are positioned so to cancel the field from the inner coil in the region outside the screen [14, 15]. Both approaches are used in combination in most MRI scanners. Poole et al. [34] proposed an eigenmode analysis of eddy currents to reduce the complex spatio-temporal eddy current field variation to a purely temporal variation. In this way, preemphasis would work exactly over the whole region of interest with a single time constant filter, since the spatial form of the eddy current field stays exactly the same. New modifications to the collimator's design and surface can also reduce the maximum induced magnetic field and mitigate the effect of residual eddy currents (next chapter 3).

2.7 Conclusions

A numerical model of the x-, y-, and z-gradient coils with different arrangements of the collimators was studied to investigate eddy currents in the tungsten collimators due to the gradient fields for SPECT/MRI system. The numerical model was validated with measurements, and it was proposed as an efficient tool for studying the effect of SPECT collimators within the MRI gradient coils. Simulations were performed using a three-dimensional electromagnetic simulator with a time analysis tool. First, we detailed the numerical model of the MRI gradient coils and the collimator. Then, we measured the resistivity of the printed tungsten used in the additive manufacturing of the collimators and we reported results of the induced eddy current measurements for a single collimator. We investigated the induced magnetic field in a full ring of pentagonal and hexagonal ring of collimators. We also studied the effect of adding gaps between the collimators in the pentagonal geometry to reduce eddy current density <2 % of the applied gradient field. The residual eddy currents can be further reduced using new design strategies for SPECT collimators to reduce eddy currents and to provide more optimized collimator designs for SPECT/MRI integration (next chapter 3).

2.8 Original Contributions

The MR-compatibility measurements in this Chapter were performed by Karen Van Audenhaege [31].

References

[1] Mark J Hamamura, Seunghoon Ha, Werner W Roeck, L Tugan Muftuler, Douglas J Wagenaar, Dirk Meier, Bradley E Patt, and Orhan Nalcioglu. *Development of an MR-compatible SPECT system (MRSPECT) for simultaneous data acquisition.* Physics in medicine and biology, 55(6):1563–75, 2010.

[2] Christian Goetz, Elodie Breton, Philippe Choquet, Vincent Israel-Jost, and André Constantinesco. *SPECT low-field MRI system for small-animal imaging.* Journal of nuclear medicine : official publication, Society of Nuclear Medicine, 49(1):88–93, 2008.

[3] Matt A. Bernstein, Kevin F. King, and Xiaohong Joe Zhou. *Handbook of MRI Pulse Sequences*. 2004.

[4] Michael A. Morich, David A. Lampman, Wayne R. Dannels, and Frederick T D Goldie. *Exact temporal eddy current compensation in magnetic resonance imaging systems.* IEEE Transactions on Medical Imaging, 7(3):247–254, 1988.

[5] Stuart Crozier, Craig D. Eccles, Frank A. Beckey, James Field, and David M. Doddrell. *Correction of eddy-current-induced B0 shifts by receiver reference-phase modulation*. Journal of Magnetic Resonance (1969), 97(3):661–665, 1992.

[6] P. Jehenson, M. Westphal, and N. Schuff. *Analytical method for the compensation of eddy-current effects induced by pulsed magnetic field gradients in NMR systems*. Journal of Magnetic Resonance (1969), 90(2):264–278, 1990.

[7] William A. Edelstein, Tesfaye K. Kidane, Victor Taracila, Tanvir N. Baig, Timothy P. Eagan, Yu Chung N Cheng, Robert W. Brown, and John A. Mallick. *Active-passive gradient shielding for MRI acoustic noise reduction*. Magnetic Resonance in Medicine, 53(5):1013–1017, 2005.

[8] Liang Cai, Xiaochun Lai, Zengming Shen, Chin Tu Chen, and Ling Jian Meng. *MRC-SPECT: A sub-500 μm resolution MR-compatible SPECT system for simultaneous dual-modality study of small animals*. Nuclear Instruments and Methods in Physics Research, Section A: Accelerators, Spectrometers, Detectors and Associated Equipment, 734(PART B):147–151, 2014.

[9] P. Busca, C. Fiorini, A. D. Butt, M. Occhipinti, R. Peloso, R. Quaglia, F. Schembari, P. Trigilio, G. Nemeth, P. Major, K. Erlandsson, and B. F. Hutton. *Simulation of the expected performance of INSERT: A new multimodality SPECT/MRI system for preclinical and clinical imaging*. Nuclear Instruments and Methods in Physics Research, Section A: Accelerators,

Spectrometers, Detectors and Associated Equipment, 734(PART B):141–146, 2014.

[10] Mediso Medical Imaging Systems. *www.mediso.com*. 2017.

[11] P. Mansfield and B. Chapman. *Active magnetic screening of gradient coils in NMR imaging*. Journal of Magnetic Resonance (1969), 66(3):573–576, 1986.

[12] R Turner and R M Bowley. *Passive screening of switched magnetic field gradients*. Journal of Physics E: Scientific Instruments, 19:876–879, 2000.

[13] Hector Sanchez Lopez, Michael Poole, and Stuart Crozier. *Evaluating passively shielded gradient coil configurations for optimal eddy current compensation*. Journal of Physics D: Applied Physics, 43(19):195005, 2010.

[14] Tesfaye K. Kidane, William A. Edelstein, Timothy P. Eagan, Victor Taracila, Tanvir N. Baig, Yu Chung N Cheng, and Robert W. Brown. *Active-passive shielding for MRI acoustic noise reduction: Network analysis*. IEEE Transactions on Magnetics, 42(12):3854–3860, 2006.

[15] R. Bowtell and P. Mansfield. *Gradient coil design using active magnetic screening*. Magnetic Resonance in Medicine, 17(1):15–21, 1991.

[16] G H Glover and N J Pelc inventors. *General Electric Company, assignee. Method for magnetic field gradient eddy current compensation*. US patent 4698591 A, October 6, 1987.

[17] Takao Takahashi. *Numerical analysis of eddy current problems involving z gradient coils in superconducting MRI magnets*. IEEE Transactions on Magnetics, 26(2):893–896, 1990.

[18] Takao Takahashi. *Numerical analysis of eddy current problems involving saddle-shaped coils in superconducting MRI magnets*. IEEE Transactions on Magnetics, 27(5):3996–3999, 1991.

[19] O Heid inventor. *Siemens Aktiengesellschaft, assignee. Magnetic resonance apparatus with compensation of fields arising due to eddy currents*. US patent 6844733 B2, January 18, 2005.

[20] Michael Poole, Hector Sanchez Lopez, Osamu Ozaki, Hitoshi Kitaguchi, Iwao Nakajima, Shin Ichi Urayama, Ken Ichi Sato, Hidenao Fukuyama, and Stuart Crozier. *Simulation of gradient-coil-induced eddy currents and their effects on a head-only HTS MRI magnet*. IEEE Transactions on Applied Superconductivity, 21(6):3592–3598, 2011.

[21] M. U. Nabi, S. V. Kulkarni, and V. R. Sule. *Novel Modeling and Solution Approach for Repeated Finite-Element Analysis of Eddy-Current Systems*. IEEE Transactions on Magnetics, 40(1 I):21–28, 2004.

[22] Adnan Trakic, Hua Wang, Feng Liu, H.S. Lopez, and Stuart Crozier. *Analysis of transient eddy currents in MRI using a cylindrical FDTD method*. IEEE Transactions on Applied Superconductivity, 16(3):1924–1936, 2006.

[23] Feng Liu and Stuart Crozier. *An FDTD model for calculation of gradient-induced eddy currents in MRI system*. IEEE Transactions on Applied Superconductivity, 14(3):1883–1889, 2004.

[24] Aldo Canova, Giambattista Gruosso, and Maurizio Repetto. *Integral methods for analysis and design of low-frequency conductive shields*. IEEE Transactions on Magnetics, 39(4 II):2009–2017, 2003.

[25] EM Software FEKO and Systems-S.A. (Pty) Ltd. *www.feko.info*. 2017.

[26] Hector Sanchez Lopez, Michael Poole, and Stuart Crozier. *Eddy current simulation in thick cylinders of finite length induced by coils of arbitrary geometry*. Journal of Magnetic Resonance, 207(2):251–261, 2010.

[27] Michael Poole and Richard Bowtell. *Novel gradient coils designed using a boundary element method*. Concepts in Magnetic Resonance Part B: Magnetic Resonance Engineering, 31(3):162–175, 2007.

[28] Karel Deprez, Roel Van Holen, and Stefaan Vandenberghe. *The lofthole: A novel shaped pinhole geometry for optimal detector usage without multiplexing and without additional shielding*. In IEEE Nuclear Science Symposium Conference Record, pages 3317–3322, 2012.

[29] Karel Deprez, Stefaan Vandenberghe, Karen Van Audenhaege, Jonas Van Vaerenbergh, and Roel Van Holen. *Rapid additive manufacturing of MR compatible multipinhole collimators with selective laser melting of tungsten powder*. Medical Physics, 40(1):012501, 2012.

[30] Roel Van Holen, Bert Vandeghinste, Karel Deprez, and Stefaan Vandenberghe. *Design and performance of a compact and stationary microSPECT system.* Medical physics, 40(11):112501, 2013.

[31] Karen Van Audenhaege. *Stationary, MR-compatible brain SPECT imaging based on multi-pinhole collimators*. PhD thesis, Ghent University, 2015.

[32] C Bouckaert, S Vandenberghe, and R Van Holen. *Design of an MR-compatible SPECT insert for simultaneous SPECT-MR imaging of a mouse*. 13th Belgian Day on Biomedical Engineering, 2014.

[33] Harald H. Quick. *Integrated PET/MR*. Journal of Magnetic Resonance Imaging, 39(2):243–258, 2014.

[34] M Poole, H S Lopez, and S Crozier. *Eigenmode Analysis of Eddy Currents and Eigenmode Coil Design*. Ismrm, 18(2005):3933, 2010.

3

Design Strategies for SPECT Collimators to Reduce the MRI Induced Eddy Currents

3.1 Introduction

In Chapter 2, a numerical model was developed to investigate the induced eddy currents due to different arrangements of tungsten collimators inside MRI coils for preclinical SPECT/MRI system. The numerical model was validated with measurements and the induced magnetic fields due to x-, y-, and z-gradient coils was characterized in a full ring of pentagonal and hexagonal ring of collimators. Chapter 2 proposed different arrangements of the collimators, including adding gaps between the collimators, to reduce the induced magnetic fields due to eddy currents. In order to optimize the transverse field of view of the SPECT/MRI system and increase it from 25 mm to around 30 mm, a new arrangement of the collimators will be used including 7 collimators instead of 5. Different design strategies will then, be used to adapt the collimator design, while keeping the heptagonal arrangement of the collimators, in order to maximally reduce the induced magnetic field due to eddy currents. With the current technology, collimators can be produced by additive manufacturing, which gives new degrees of freedom to the design and the material. Additive manufacturing uses selective laser melting of pure tungsten powder and provides techniques for the production of complex multipinhole collimators designs [4]. Eddy current reduction by introducing lamination, horizontal,

and vertical slits in the design has been reported for power transformers [5–8], electric motors [9, 10] and bending magnets [11]. Slit-slat and multi-slit slit-slat collimators was previously introduced for different SPECT system [12–15]. A slit-slat collimator can be considered as a mixture of a pinhole and a parallel-hole collimator. The slits used in [16] are oriented parallel to the axis of rotation of the collimator and form long knife-edges so that the collimator has the properties of a pinhole collimator in the transverse plane [16]. To the author's knowledge, slits in the collimators, core material reduction, and z-shaped vertical slits have never been used before for eddy currents reduction in SPECT/MRI systems.

The objective of this chapter is to use different collimators designs to optimize the SPECT collimator in order to reduce eddy currents by introducing smart design modifications. The final model will consist of a heptagonal configuration of optimized collimators designs. To this aim, numerical simulations are carried out using x-, y-, and z-gradient coils along with different designs of the collimators using FEKO [17]. First, the current density (J) was extracted for different single collimators design and compared to the original collimator current density. The induced magnetic field was then calculated for each ring of the adapted collimators and reduction in maximum induced magnetic field due to eddy current was reported and discussed. In Section 3.2.4 the simulation platform, MRI gradient coils and original collimator model are presented. Short description of the metal additive manufacturing process is also described in this section with introduction of the different design used to reduce the induced magnetic field due to eddy currents. Section 3.3 is dedicated to the description of the current density distribution in the single and ring of collimators. J distribution was extracted and compared for the original and adapted designs in single and heptagonal arrangement of the collimators. In Section 3.4, we reported the reduction in the maximum value of the induced magnetic field due to eddy currents for optimized collimators designs with a comparison of the current density for the ring of the original and the optimally adapted collimators. Section 3.5 shows then the magnetic induction due to eddy currents as a percentage of the applied gradient field for longitudinal and transverse gradient coils for the original and the optimized ring of collimators. Finally, conclusions are drawn in Section 3.6

3.2 Materials and Methods

3.2.1 Simulation Platform and Validation Method

The gradient coils [18] and collimators were modeled with FEKO (method of moments) [17], a three-dimensional electromagnetic simulation platform. FEKO (Altair, Germany) uses the method of moments, which provides full-wave solutions of Maxwell's integral equations in the frequency domain. We also used

FEKO's time analysis functionality, allowing electromagnetic problems to be analyzed in the time domain. The relevant computations were performed in the frequency domain and fast Fourier transform algorithms were used to transform the data to the time domain. First, we extracted frequency components of the gradient pulse by applying fast Fourier transform; we then performed a broadband simulation covering the frequency range of the gradient shape. The output was then post processed to extract the time response of the system, based on the gradient pulse. The setup was simulated with a broadband simulation from 0 to 10 kHz to cover the frequency range of a sinusoidal pulse with a ramp-down time of 0.25 ms.

We performed simulations with x-, y-, and z-gradient coils for preclinical systems (Figure 3.1). The coils are fed with 167.24 A and 162.33 A for transverse and longitudinal gradient coils, respectively. The gradient strength was 500 mT/m, and the maximum gradient deviation in a sphere of 30 mm was 2.06 % and 0.86 % for transverse and longitudinal gradient coils, respectively. The validation of the simulation model with measurements was reported in the Chapter 2. To validate simulations with the configuration of measurements, we considered a z-gradient coil, a representation of the phantom, a radio-frequency (RF) coil and a cuboid representing the lead block (Pb). The results of the simulations were compared to measurements using a 7T MRI scanner (Bruker Pharmascan). The z-gradient coil and the simulation tool used in Chapter 2 are identical to those used in this Chapter. The maximum variation between measurement and simulation was less than 1% of the applied gradient field (G = 500 mT/m).

3.2.2 Metal Additive Manufacturing

Additive manufacturing is a broad term used for a variety of production techniques in which material is built up in thin layers by 3D printers based on a 3D CAD design (STL file). The process starts with a thin solid piece on which consecutive layers of metal powder are melted. The melting is done with a laser that selectively melts the powder at locations where solid material is needed based on an STL file, created with 3D CAD software (Figure 3.1a). Figure 3.2 shows the steps used in the process of metal additive manufacturing. The production process starts with a thin solid piece of tungsten that is placed on the object piston Figure 3.2e). The powder table (Figure 3.2g) moves and the power distributer (Figure 3.2f) spreads a thin layer of tungsten powder on the solid tungsten piece. In the next step the laser scanner system (Figure 3.2a and Figure 3.2b) with a high intensity focus melts the wanted cross section of the part. Now, the object piston (Figure 3.2e) moves down and a subsequent layer can be build up. The multi-pinhole collimator (3.1b) is a complex and challenging design that was produced using metal additive manufacturing.

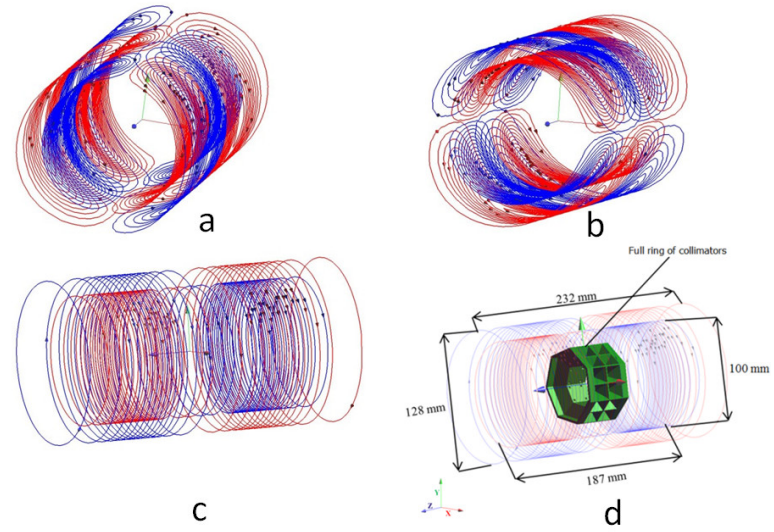

Figure 3.1: Wire patterns for (a) X-gradient coil. (b) Y-gradient coil and(c) Z-gradient coil. (d) Full ring of the collimators centered inside the z-gradient coil. Red and blue colors are used to indicate wires in which there is a different sense of current flow. (gradient coils from Poole [18])

3.2.3 Original Collimator

Figure 3.3a shows the proposed collimator that has been developed for a new microSPECT system (Figure 3.3b). The system consists of 7 identical collimators and digital silicon photomultipliers assembled in a ring. The system is stationary and therefore less sensitive to geometric calibration issues, better suited for dynamic and gated imaging and easier to integrate with MRI [4, 19]. Tungsten is a promising material for the production of MR-compatible collimators. It has a high number of electrons (Z=74) and a high density (19.25 g/cm^3). However, pure tungsten is difficult to process. It is both hard and brittle. Therefore, many pinhole collimators are made from tungsten alloys (with nickel, iron and/or copper). They are easier to process but have a higher susceptibility and are thus less MR-compatible. Additive manufacturing overcomes these problems by selective laser melting of pure tungsten powder. This technique can produce complex parts, given some restrictions like a minimum feature size of 500 µm, a precision of 50 µm and a maximum build volume of 245 mm x 245 mm x 190 mm and larger parts will be possible in the future. Down facing surfaces are also difficult to construct or need a supporting structure (Layerwise, Belgium). Selective laser melting also allows varying the density of the material. The supplier of the collimator is able to produce tungsten densities from 80 to 99%. Lower density tungsten has

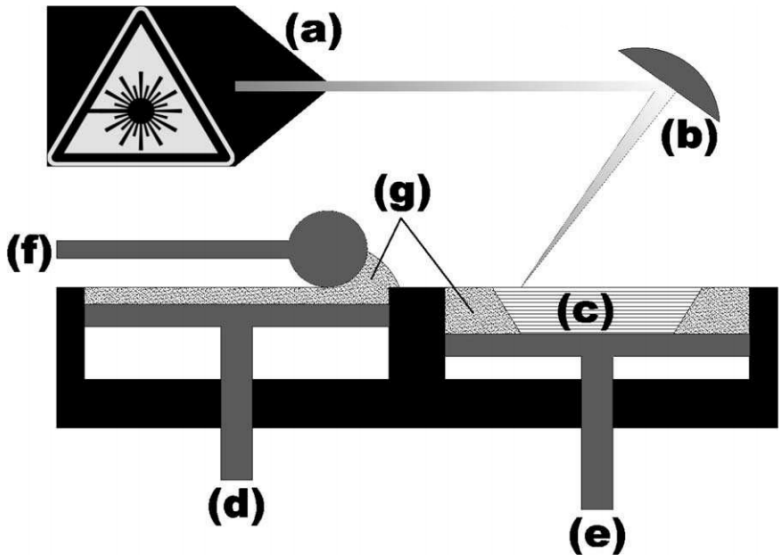

Figure 3.2: Illustration of the production process: laser source (a), scanner system (b), collimator (c), powder delivery system (d) and (f), object piston (e), powder (g) (source: Deprez [4]).

a lower conductivity, resulting in less eddy currents as reported and discussed in Section 2.4.1 (chapter 2). On the other hand, a lower density also results in a lower attenuation coefficient and thus less photons are attenuated by the material. In fact, according to the Beer-Lambert law, the number of photons transmitted through a material is equal to:

$$N = N_0 e^{-\mu\, x} \tag{3.1}$$

where N_0, x, and μ are the number of incident photons, thickness of the material (in cm) and linear attenuation coefficient usually expressed in cm^{-1}. The attenuation factor is then equal to $1 - \frac{N}{N_0}$. The attenuation coefficient, μ, is the product of the mass attenuation coefficient (photon energy dependent) with the volumetric mass density of the material. The mass attenuation coefficient for tungsten is equal to 1.581 cm^2/g for photons with an energy of 140 keV. The collimator was produced using additive manufacturing and had a density of 17.31$\pm$ 0.10 g/cm^3 (89.92 $\pm$ 0.05 % of pure tungsten), thus, using Equation 3.1, 2 mm of this material is sufficient to attenuate photons with energy of 140 keV which stops 99.58 % of all incoming gamma rays. Due to the additive manufacturing process, the collimator has a different resistivity along the transversal (292 nΩ.m) and the longitudinal (108 nΩ.m) direction. Because eddy currents increase with the material conductivity, we performed our simulations with a collimator using the lowest resistivity

(108 nΩ.m) to cover the strongest eddy currents.

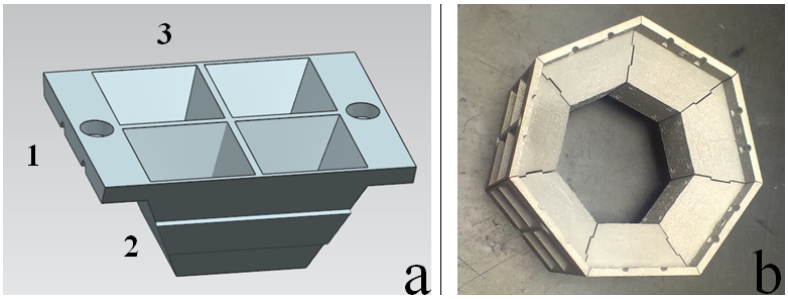

Figure 3.3: The original collimator. a) 3D CAD design of one collimator (1: flange, 2: slope, 3: region of pinholes). b) Printed full-ring multilofthole collimator.

3.2.4 System Optimization

Different collimators designs were investigated to reduce eddy currents induced in the collimators ring. We did this step-by-step and investigated the effect of every modification separately. We then evaluated the induced magnetic field due to the full ring collimator insertion for each optimization. The magnetic field due to eddy currents (B_e) was calculated by subtracting the z-component of the magnetic induction of the gradient coils without collimator (B_z) from the z-component of the magnetic induction of the gradient coils with the collimators (B_z^{col}). The choice of the z component is motivated by the fact that it represents the main component for the gradient field. The maximum induced magnetic field $B_{i,max}$ for each optimization was compared to the maximum induced magnetic field $B_{0,max}$ in the original collimator (Figure 3.3) using the relative variation (Δ_i in percentage) as follows:

$$\Delta_i = 100\ \frac{B_{0,max} - B_{i,max}}{B_{0,max}} \tag{3.2}$$

Figure 3.4 shows the different designs we simulated to reduce the induced magnetic field due to eddy currents.

Smaller Flanges:

First, we removed all excess material. The flanges (region 1 in Figure 3.3) at the edges of the collimator have as only function to mount the collimator and not to attenuate photons. Therefore, the first adaptation to the design was a reduction of the excessive material in the flanges where high current densities are expected. Proper mounting of the collimator is still possible (Figure 3.4A).

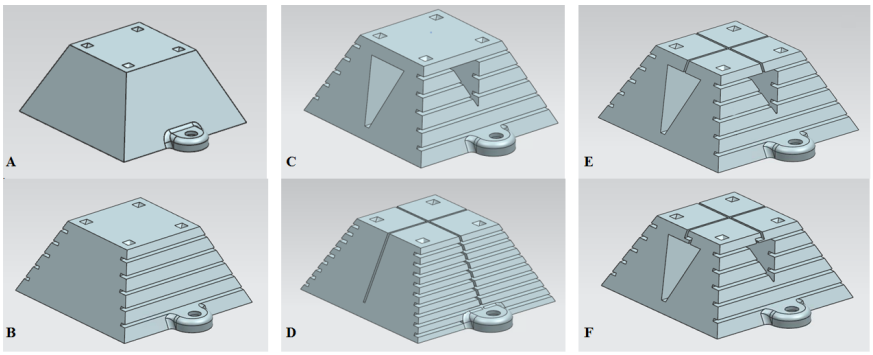

Figure 3.4: Adapted collimator designs. A): Smaller flanges. B): Horizontal slits. C): Material reduction in the core. D): Vertical slits in the middle. E): Combined vertical slits and material reduction. F): Z-shaped vertical slit.

Horizontal Slits:

It is expected that the current density is highest near the surface of the collimator due to the skin effect. This can be reduced with slits in the surface [11, 20] (Figure 3.4B).

Material Reduction in the Core:

In the center of the collimator there is a solid core of tungsten. The photons are attenuated before they reach the core so this excessive material may be omitted (Figure 3.4C). We expect this to further reduce eddy currents but the collimator will be more complex to print and a supporting structure will be needed.

Vertical Slit in the Middle:

The supporting structure can be avoided by using two vertical slits in the middle of the collimator (Figure 3.4D) to reduce eddy currents instead of removing all the core material.

Z-Shaped Vertical Slit:

In order to maximally reduce the eddy current, the two previous solutions (Sections 3.2.4 and 3.2.4) can be combined (Figure 3.4E). However, when the reduction of material in the core is combined with the vertical slits, some photons might not be attenuated and pass though the vertical slits and the thin wall of the lofthole. This penetration can be avoided by using a Z-shaped slit (Figure 3.4F and

Figure 3.5) instead of the vertical slit of Figure 3.4D.

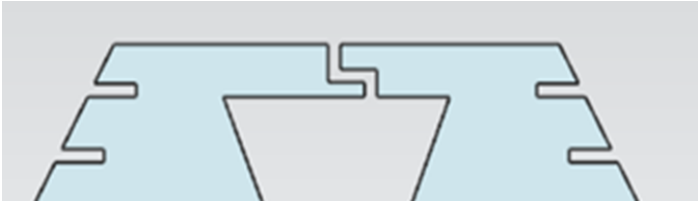

Figure 3.5: Z-shaped vertical slit.

3.3 Current Density Distribution

3.3.1 Current Density Distribution in the Original Collimators

Figure 3.6(a) shows the transversal view of current density distribution (RMS modulus, in dB normalized to 40.6 MA/m^2) in a single original collimator (Figure 3.3a) . The global maximum value is 40.62 MA/m^2 at x = 34.15 mm, y = 0.6 mm and z = -21.45 mm (located in the flanges region). This figure indicates that J increases with x and z. As the collimator is positioned 21 mm off-center in the x-direction, the increase in the x direction can be explained by the fact that the collimator is positioned closer to the wires of the gradient coils. The increase of J in the z-direction is explained by the fact that the applied magnetic field that increases linearly with the z position. These results confirm that the eddy currents are high in the flanges and in the core of the collimator, which justifies our adaptations to these areas. Figure 3.6(b) shows the summed J for different slices perpendicular to the z-axis. We added identifications for the different regions on the graph according to Figure 3.3a. The highest values of J are located in the flange region and around the center of the collimator, whereas the minimal value is located at the center (z = 0 mm). This indicates that by adapting the flanges we can reduce the maximal J value. Figure 3.6b showed the presence of 3 minima in the current density distribution at z $\approx \pm$ 19 mm, z $\approx \pm$ 7 mm, and z = 0 mm (indicated with 1, 2, and 3 in Figure 3.6b). This can be explained by the presence of the hole in the flanges, the location of the pinhole apertures in the collimator, and the very low value of the applied magnetic field in the slice z = 0, respectively.

Figures 3.7a and 3.7b show the maximum and the minimum J slice along the z-axis (longitudinal slices). The highest and lowest current density values occur at the edge and the center of the ring respectively. Figure 3.7 shows the summed current density (RMS modulus) for longitudinal slices on the full ring of seven collimators. The highest values of J are located near the edge of the ring and the

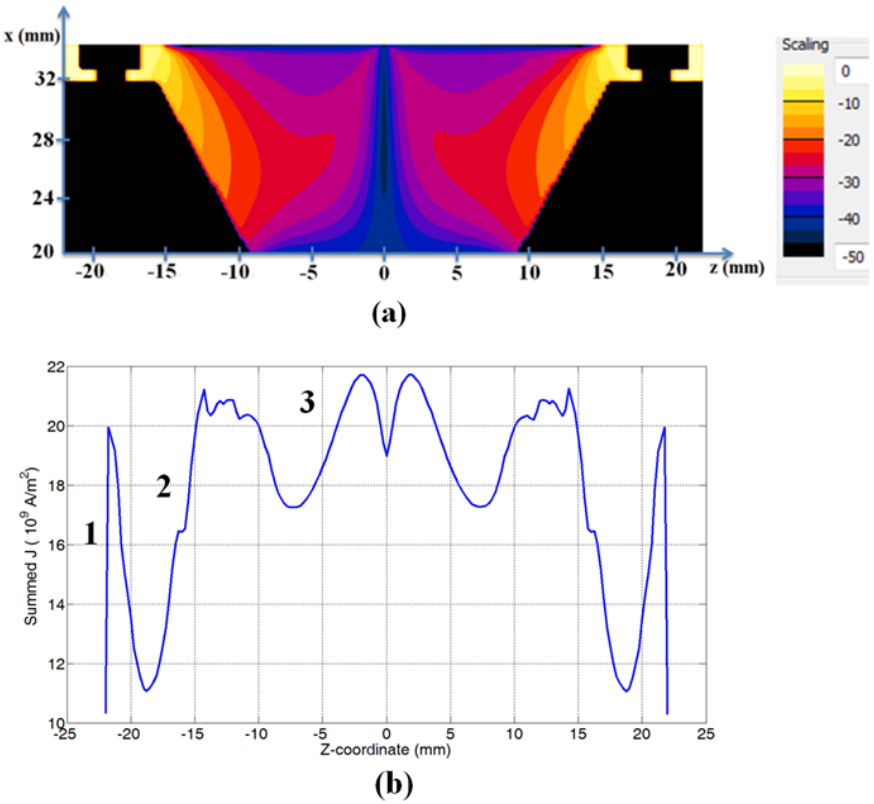

Figure 3.6: Current density distribution on a single collimator. (a): Transversal view of J (RMS modulus, in dB normalized to 40.6 MA/m^2) where the maximum J is located. (b): Summation of J (RMS modulus) in each slice perpendicular to the z-axis, (1 = flange, 2 = slope, 3 = region of pinhole).

minimum values occur at the center, with a decrease in summed J from the edge to the center of the ring. Simulations with the full ring of the collimators indicated that there is no cumulative effect of the current density of the individual collimators. In fact, Figure 3.8 shows a maximum current density of 80 MA/m^2 for the full ring of the collimators while the maximum of summed J of a single collimator is about 21 MA/m^2. Figure 3.7 and 3.8 even show a compensation effect of the current densities from different collimators on the global current density near the center of the ring.

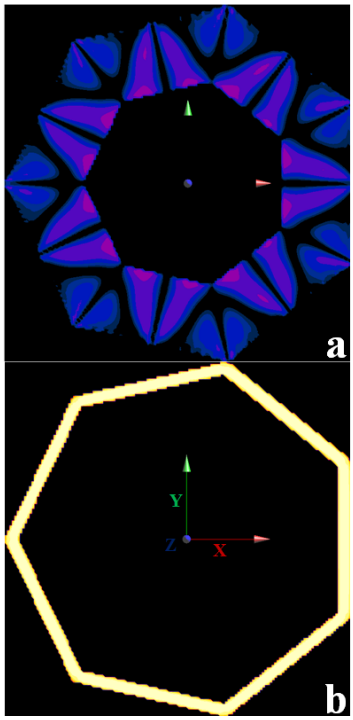

Figure 3.7: Transversal slices of the current density J (RMS modulus, in dB normalized to 46.3 MA/m^2) on the ring of seven collimators. (a): Minimum J slice z = 0 mm. (b): Maximum J slice z = 21.5 mm (scaling of Figure 3.6 and Figure 3.7 is identical).

3.3.2 Current Density on the Adapted Collimators

Figure 3.9 shows current density on the surface of the collimator for different adapted designs shown in Figure 3.4 and a comparison between the original and the optimized design (Figure 3.9O and 3.9F) shows a general decrease in current density. Figure 3.9O shows that high values of current density are located in the flanges of the collimators which motivates the first adaptation of our design (smaller flanges).

3.4 System Optimization Results

Table 3.1 shows the reduction in the maximum value of the induced magnetic field due to eddy currents inside a FOV of 3 cm, for each adaptation separately for the full ring of 7 collimators. Smaller flanges reduce the current density by 18 % and 16 % for longitudinal and transverse coils (x- and y-gradient coils), respectively. The horizontal slits reduce the eddy currents by 22.5 % and 20 % for

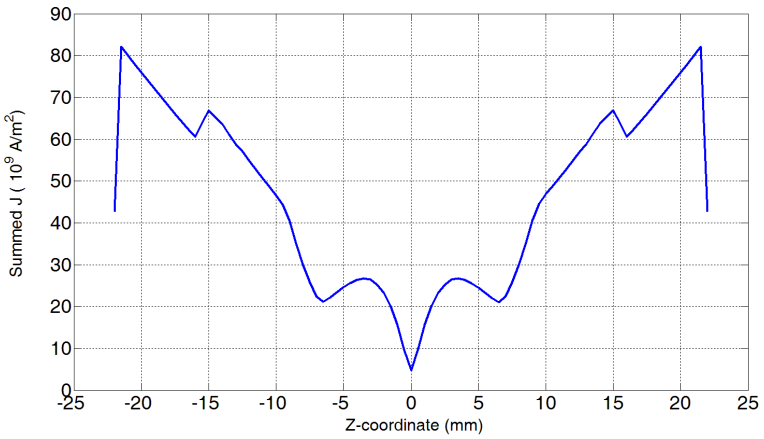

Figure 3.8: Summation of J (RMS modulus) in each slice perpendicular to the z-axis for the ring of seven collimators.

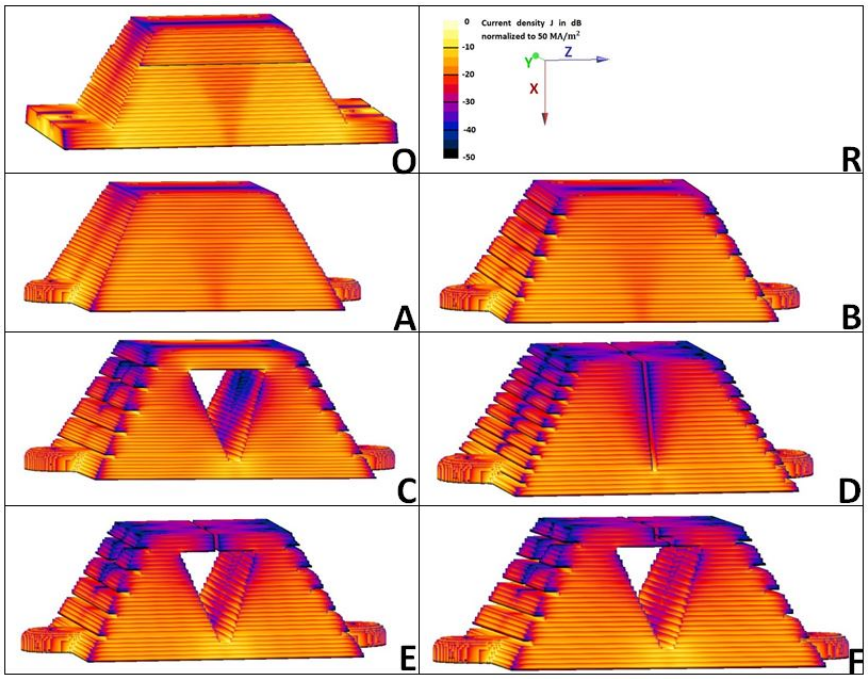

Figure 3.9: Current density on the surface of a single collimator (RMS value in dB normalized to 50 MA/m^2). O: Original collimator as shown in Fig. 2a. R: Reference and scaling for all the sub-figures. A-F: Adapted collimator designs as shown in Figure 3.4.

longitudinal and transverse coils, respectively. Using less material in the core or applying vertical slits results in almost the same reduction (37 % and 33 % for longitudinal and transverse coils). However, the vertical slits are cheaper because a hollow collimator requires supporting structures during production. Both can be combined, the reduction is then 54 % and 48 % for longitudinal and transverse coils, respectively. The z-shaped slits (Figure 3.5) are used to prevent attenuation problems introduced by the vertical slits and less material in the core combination. The reduction for z-shaped slits is then about 54 % and 48 % for longitudinal and transverse coils, respectively. Figure 3.10 shows the summed J on the full ring of

Adaptation	Description	Reduction (%) for longitudinal coil	Reduction (%) for transverse coils
A	Smaller flanges	18.36	15.93
B	Horizontal slits (2 mm)	22.54	19.54
C	Less material in the core	37.24	33.24
D	Vertical slits	37.06	33.23
E	Vertical slits and less material in the core	53.85	47.80
F	Vertical z-shaped slits and less material in the core	53.85	48.17

Table 3.1: Reduction in the maximum eddy current (B_e) for different adaptation (Figure 3.4)

the original collimators and the optimally adapted collimator. The highest reduction occurs at the edges and around the center of the ring.

The most important reductions are near the region of the flanges (smaller flanges design) and the center of the collimators (less material in the core and vertical slits designs). The z-shape configuration with reduced material in the core seems to be the most favorable since it gives the highest reduction value. The collimator was optimized for the microSPECT system (in terms of pinholes) and thus, we opted to modify this multi-pinhole collimator instead of making a new one and optimize it for the microSPECT system. A general rule is to omit all unnecessary material (which also makes the production cheaper when using additive manufacturing) while paying attention not to disturb the basic function of the collimator.

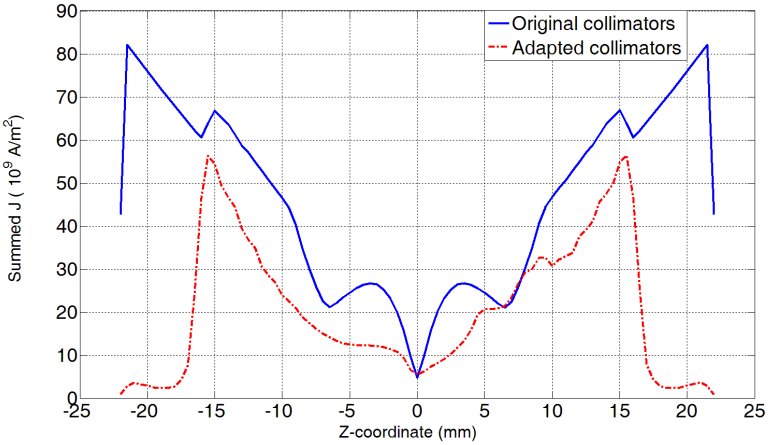

Figure 3.10: Summation of J (RMS modulus) in each slice perpendicular to the z-axis for the ring of the original and the optimally adapted collimators using the longitudinal coil.

3.5 Temporal Variation of the Induced Field for the Original and the Optimized Ring of Collimators

Figure 3.11 shows the magnetic induction due to eddy currents (B_i) as a percentage of the applied gradient field for longitudinal and transverse gradient coils (x- and y-gradient coils) for the original (Figure 3.3a) and the optimized (Figure 3.4F) ring of collimators, averaged in a FOV of 3cm. For the original collimator, the maximum value of the induced magnetic field is 4.21 % and 1.06 % of the applied gradient field (gradient strength = 500 mT/m) for longitudinal and transverse gradient coils, respectively. For the optimized ring of collimators, we have 1.91 % and 0.46 % of the applied gradient field for longitudinal and transverse gradient coils, respectively. The transverse coils induce thus less eddy currents than the longitudinal. This is due to the wire distribution for the two types of the coils and the collimators' position inside the coils (explained in more details in Section 2.5 Chapter 2). A global reduction of 53.8 % and 48.2 % for longitudinal and transverse coils, respectively, is finally obtained with these design changes, and thus by using the optimized design we can bring the percentage of the induced magnetic field to less than 2% of the applied gradient field. This guideline value of 2% is experimentally derived during measurements for the SIMRET project (Chapter 2)

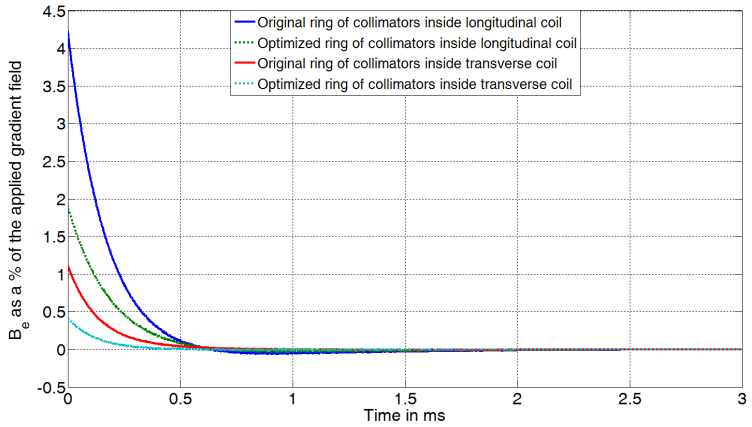

Figure 3.11: B_i (induced B-field due to eddy currents) as a percentage of the applied gradient field of 500 mT/m for both the longitudinal and the transverse gradient coils (x- and y-gradient coils) averaged in a FOV of 3 cm..

3.6 Conclusions

In this chapter, we investigated and reduced the induced magnetic field due to eddy currents in a full heptagonal ring of collimators that has been developed for a SPECT/MRI system. A numerical model of the x-, y-, and z-gradient coils with different designs of the collimators was studied to investigate eddy currents in the tungsten collimators due to the gradient fields for SPECT/MRI system. Simulations were performed using a 3D electromagnetic simulator with a time analysis tool. We made small modifications to the collimator's design and surface and reduced the maximum induced magnetic field by 53.8 % and 48.2 % for longitudinal and transverse coils, respectively, which results in an improved MR-compatibility. We conclude that printed tungsten collimators are suited to be used for combined SPECT/MRI systems. The final design presented in this chapter can be produced using the promising technique of metal additive manufacturing.

References

[1] Amine M. Samoudi, Karen Van Audenhaege, Günter Vermeeren, Michael Poole, Emmeric Tanghe, Luc Martens, Roel Van Holen, and Wout Joseph. *Analysis of eddy currents induced by transverse and longitudinal gradient coils in different tungsten collimators geometries for SPECT/MRI integration*. Magnetic Resonance in Medicine, 74(6):1780–1789, 2015.

[2] Amine Samoudi, Karen Van Audenhaege, Günter Vermeeren, Micahel Poole, Luc Martens, Roel Van Holen, and Wout Joseph. *Temporal analysis of Z-Gradient coil eddy currents in tungsten collimator with different resistivities for SPECT/MRI*. EJNMMI Physics, 1(1):A22, Jul 2014.

[3] Amine Samoudi, Karen Van Audenhaege, Günter Vermeeren, Micahel Poole, Luc Martens, Roel Van Holen, and Wout Joseph. *Temporal analysis of Z-Gradient coil eddy currents in tungsten collimator with different resistivities for SPECT/MRI*. ISMRM, page 2545, 2014.

[4] Karel Deprez, Stefaan Vandenberghe, Karen Van Audenhaege, Jonas Van Vaerenbergh, and Roel Van Holen. *Rapid additive manufacturing of MR compatible multipinhole collimators with selective laser melting of tungsten powder*. Medical Physics, 40(1):012501, 2012.

[5] Saurabh Kumar Mukerji, Moleykutty George, M. B. Ramamurthy, and Khandaker Asaduzzaman. *Eddy Currents in Laminated Rectangular Cores*. Progress In Electromagnetics Research, 83:435–445, 2008.

[6] László Koller and Balázs Novák. *Ridged surface for reducing eddy-current losses in ferromagnetic shielding*. Electrical Engineering, 91(3):117–124, 2009.

[7] Anastassia J. Tsivgouli, Marina A. Tsili, Antonios G. Kladas, Pavlos S. Georgilakis, Athanassios T. Souflaris, and Annie D. Skarlatini. *Geometry optimization of electric shielding in power transformers based on finite element method*. Journal of Materials Processing Technology, 181(1-3 SPEC. ISS.):159–164, 2007.

[8] R.L. Russell and K.H. Norsworthy. *Eddy currents and wall losses in screened-rotor induction motors*. Proceedings of the IEE Part A: Power Engineering, 105(20):163, 1958.

[9] Katsumi Yamazaki, Yuji Kanou, Yu Fukushima, Shunji Ohki, Akira Nezu, Takeshi Ikemi, and Ryoichi Mizokami. *Reduction of magnet eddy-current loss in interior permanent-magnet motors with concentrated windings*. IEEE Transactions on Industry Applications, 46(6):2434–2441, 2010.

[10] Seok Hee Han, Thomas M. Jahns, and Z. Q. Zhu. *Analysis of rotor core eddy-current losses in interior permanent-magnet synchronous machines*. In IEEE Transactions on Industry Applications, volume 46, pages 196–205, 2010.

[11] M. Negrazus, D. George, V. Vrankovic, and M. Werner. *Eddy current reduction in fast ramped bending magnets*. In IEEE Transactions on Applied Superconductivity, volume 16, pages 228–230, 2006.

[12] Scott D. Metzler, Roberto Accorsi, Ahmet S. Ayan, and Ronald J. Jaszczak. *Slit-slat and multi-slit-slat collimator design and experimentally acquired phantom images from a rotating prototype*. IEEE Transactions on Nuclear Science, 57(1 PART 1):125–134, 2010.

[13] S T Mahmood, K Erlandsson, I Cullum, and B F Hutton. *The Potential for Mixed Multiplexed and Non-Multiplexed Data to Improve the Reconstruction Quality of a Multi-Slit-Slat Collimator SPECT System*. Physics in Medicine and Biology, 55(8):2247–68, 2010.

[14] Shelan Mahmood, Kjell Erlandsson, Ian Cullum, and Brian Hutton. *Experimental results from a prototype slit-slat collimator with mixed multiplexed and non-multiplexed data.* Physics in medicine and biology, 56(14):4311–31, 2011.

[15] I Perali, A Celani, L Bombelli, C Fiorini, F Camera, E Clementel, S Henrotin, G Janssens, D Prieels, F Roellinghoff, J Smeets, F Stichelbaut, and F Vander Stappen. *Prompt gamma imaging of proton pencil beams at clinical dose rate*. Physics in Medicine and Biology, 59(19):5849–5871, 2014.

[16] Roberto Accorsi, John R. Novak, Ahmet S. Ayan, and Scott D. Metzler. *Derivation and validation of a sensitivity formula for slit-slat collimation*. IEEE Transactions on Medical Imaging, 27(5):709–722, 2008.

[17] EM Software FEKO and Systems-S.A. (Pty) Ltd. *www.feko.info*. 2017.

[18] Michael Poole and Richard Bowtell. *Novel gradient coils designed using a boundary element method.* Concepts in Magnetic Resonance Part B: Magnetic Resonance Engineering, 31(3):162–175, 2007.

[19] Roel Van Holen, Bert Vandeghinste, Karel Deprez, and Stefaan Vandenberghe. *Design and performance of a compact and stationary microSPECT system.* Medical physics, 40(11):112501, 2013.

[20] Matt A. Bernstein, Kevin F. King, and Xiaohong Joe Zhou. *Handbook of MRI Pulse Sequences*. 2004.

Part II

Patients Exposure to MRI Gradient Fields

4

Numerical Modelling of Children and Adults Exposure to Pulsed Gradient Fields in MRI

4.1 Introduction

Interactions of the living tissue with MRI scanner can cause potential patient risks [1–3]. Rapidly induced fields could stimulate nerves of the peripheral nervous system [3, 4]. Nerve stimulation might interfere with the examination [5]. Therefore, the physiological limit of exposure to such fields should be based on minimizing uncomfortable or intolerable sensation. Different guidelines and standards [5–7] suggest limits to mitigate these potential hazards. The IEC (2010) and ICNIRP (2004) recommended a maximum exposure level be set to a time rate of change of the magnetic field (dB/dt) or induced electric field (E) of 80% of the median perception threshold for peripheral nerve stimulation (PNS) for routine operation, and 100% of the median perception threshold for controlled operation [5–7].

Since the electric fields in tissue cause PNS and are practically difficult to be measured in humans, it is therefore necessary to numerically simulate and evaluate these fields. Such numerical simulations facilitates better understanding of the PNS phenomenon in MRI and, therefore, allows for prevention of its occurrence in subjects undergoing imaging without unnecessary restrictions placed on the switching rates of gradient fields. Induced electric fields in tissues from switching gradient coils have been computed in a few studies. Bencsik et al. [8] studied in-

duced electric fields in spherical and cylindrical tissue models due to time-varying gradient fields and highlighted the importance of both magnetic vector potential and electric scalar potential in deriving the internal electric field. Similarly, Mao et al. [9] reported calculations of the induced E-field within an anatomically realistic body model within an x-gradient coil and highlighted the importance of including the scalar potential associated with the windings of the coil, as well as the effect of the presence of an RF shield. Forbes et al. [10] considered simplified cylindrical models of a body and gradient coil and used an exact solution to Maxwell's equations to predict the transient E-fields induced within the body model by the rapid switching of current in the coil. Zhao et al. [11] described a modified FDTD method that was applicable to simulating gradient field-induced E-fields and induced currents within a human model. This technique was also used by Brand and Heid [12] who simulated induced E-fields within three body models: a homogeneous conducting rotational ellipsoid model, and two human male models, one with homogeneous conductivity and the other with nonhomogeneous conductivity. Lu and Ueno [13] investigated exposure of a voxel adult man model to gradient coils and compared result with the ICNIRP 1998 [14] basic restrictions. As reported, only simplified human models were used for these investigations. However, since the human body size and tissues locations inside the MRI coils are different between adult male, adult female and child models, the choice of the human body model can have and important impact on the induced electric field. On the other hand, other studies have investigated the exposure of workers to pulsed gradients in MRI and showed that it is possible to induce electric fields/current densities above levels recommended by the standards when the workers are standing close to the gradient coils [15, 16]

Another important issue, not considered in the PNS literature, is the modelling of the skin in the low-frequency magnetic field exposure. Schmid et al. [17] pointed out an obvious potential source of errors and uncertainties concerning computations of induced electric field strengths inside skin tissue in the low frequency range. It has been demonstrated that the conductivity values for skin obtainable from the most widely used data bases of dielectric tissue properties are not suitable for exposure assessment with respect to peripheral nerve tissue. De Santis et al. [18] conducted a sensitivity analysis on the electro-geometrical parameters of human skin. First, a multi-layer canonical skin structure is modeled to closely mimic the biological composition of the skin. An equivalent single-layer skin model is then derived. They finally suggested the value of 0.2 S/m for the skin conductivity.

The purpose of the present Chapter is to determine exposure of adults and children in an MR scanner by evaluating the induced electric fields in realistic 3D whole-body adult male, adult female, and child models within shielded whole-body x-, y- and z-gradient coils and compare them with ICNIRP 2004, and IEC

2010 guidelines. In Section 4.2, numerical simulations are carried out, using x-, y-, and z-gradient coils with detailed anatomical human models consisting of male, female and child human phantoms. The simulation platform was then validated against analytically derived results. The methodology used to evaluate the induced electric field in the human bodies were also detailed in Section 4.2. Sections 4.4, 4.5, and 4.6 are dedicated to the investigation of the effect of coils' type, human model type, and skin conductivity on the induced electric fields in fat and skin. In Section 4.7, compliances with IEC2010 and ICNIRP2004 guidelines are investigated and discussed. Finally, conclusions are drawn in Section 4.8.

4.2 Materials and Methods

4.2.1 Gradient Coils Models

Gradient coils and human bodies were modeled with a commercial software package SEMCAD-X (SPEAG, Switzerland) [19]. The induced electric fields in the human body were analyzed with the SEMCAD X magneto quasi-static solver.

Whole-body, symmetric shielded gradient transverse (x- and y-axis) and longitudinal (z-axis) coils [20] were used in this investigation to compute the current densities and the electric fields induced in the body models. All three gradient coils have approximately the same axial length of 1.4 m and the same diameter of 0.6 m for the primary coils. With this axial length, the gradient coils would fit inside most conventional MRI systems [15, 21]. Table 4.1 lists some coil parameters while Figure 4.1 shows designs of the gradient coils. The gradient coils are fed with pulsed sine currents of 1 kHz. A pulsed sine of 1 kHz represents the main frequency of the echo-planar imaging sequences, which is one of the fastest imaging sequences in clinical imaging. Since the induced currents is higher for faster pulse sequences, a frequency of 1 kHz represents the worst case for the patient exposure to induced electric filed (the highest values of the induced E-field). The diameter of spherical volume (DSV) is given as the region where the gradient field is uniform to 5% peak-peak and is expressed as diameter in meters. The secondary coil in Figure 4.1 is mainly used for shielding to reduce the magnetic field (generated by the primary coil) outside the field-of-view (FOV).

Gradient coil	Primary coil diameter (m)	Secondary coil diameter (m)	Primary coil length (m)	Secondary coil length (m)	DSV (m)
X	0.6	0.75	1.4	1.75	0.29
Y	0.6	0.75	1.4	1.75	0.27
Z	0.6	0.76	1.4	1.74	0.36

Table 4.1: Geometrical parameters of the transverse and the longitudinal gradient coils.

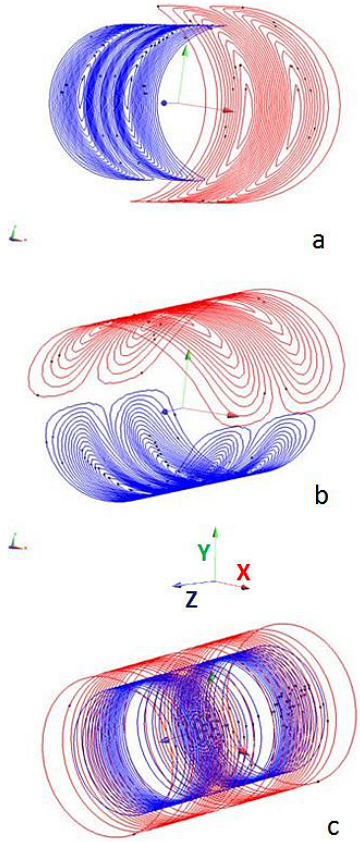

Figure 4.1: a: Wire patterns for a: x-gradient coil, b: y-gradient coil, and c: z-gradient coil. For transverse coils only one primary and one secondary layer is illustrated, while both are plotted for the longitudinal gradient coil. Red and blue colors are used to indicate wires in which there is a different sense of current flow (Source: Poole [20]).

4.2.2 Anatomical Models and Tissue Dielectric Properties

We used three human models (Figure 4.2) from the Virtual Population [22]: Duke, a 34-year-old male (72 kg, 1.77 m); Ella, a 26-year-old female (59 kg, 1.63 m); and Billie, an 11-year-old girl (35 kg, 1.47 m). These anatomical models have been developed from high-resolution MRI data and consist of more than 80 tissues and organs [23]. The dielectric parameters of the tissues are set based on the database developed by the IT'IS Foundation [23] mainly from the Gabriel dispersion relations [24]. To further account for weighing outer and inner skin layers, skin conductivity was set to $0.2\,\mathrm{Sm}^{-1}$ [18].

The human models were centered inside the gradient coils as shown in Figure 4.2. Uniform rectilinear meshes were applied to easily discretize the complex anatomical models with a voxel size of 2 mm along x, y, and z direction. The male, female, and girl body models were meshed approximately to 41.58 Mcells, 33.28 Mcells, and 25.95 Mcells, respectively.

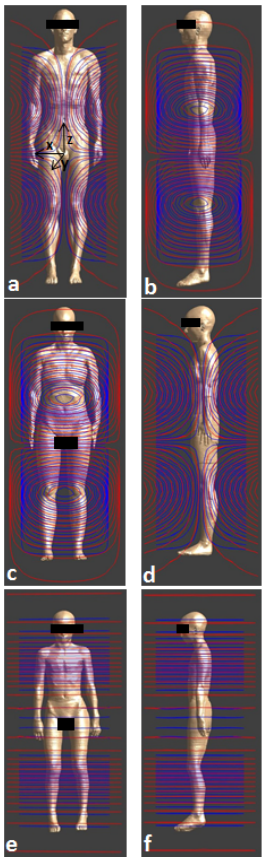

Figure 4.2: Orthogonal views (front and side) of body model inside gradient coils. a, b: Duke inside the x gradient coil. c, d: Ella inside the y gradient coil. e, f: Billie inside the z gradient coil.

4.2.3 Comparison with Analytical Solutions

We performed simulations to compare analytically derived results with simulations results to validate the simulation platform. The numerical model is composed of a homogeneous sphere (conductivity = 0.1 Sm^{-1}, radius = 0.25 m) placed symmetrically inside two concentric current loops forming a Helmholtz pair with radius and center-center separation of 0.35 m (Figure 4.3). The two loops were fed with a sinusoidal current of peak amplitude 1 A and the model was discretized with a voxel size of 5 mm. The B-field, which has only a z-component in this configuration, at a distance r off axis in the mid-plane, B_{Hz} is [25, 26]

$$B_{\mathrm{Hz}} = \frac{I\mu_0}{\pi a\sqrt{((1+\alpha)^2+\beta^2)}} \times \left[E(k)\frac{1-\alpha^2-\beta^2}{(1+\alpha)^2+\beta^2-4\alpha} + K(k)\right] \quad (4.1)$$

where I is the current in the loops, a is the radius of the loops, $\alpha = r/a$, $\beta = d/a$,$k = \frac{\sqrt{ar}}{a+r}$, r is the radial distance from the axis to the field measurement point, $2d$ is the separation of the loops, $\mu_0 = 4\pi\ 10^{-7}$ H/m is permeability of free space, and $E(k)$ and $K(k)$ are the complete elliptical integrals of the first and second kind, respectively. Analytical formula of the current density within a homogeneous sphere exposed to a time-varying uniform B-field is given by [26] :

$$J(r) = \pi f \sigma B r \quad (4.2)$$

where r is the radial distance (m), f is the frequency (Hz), B is the magnetic flux density (T), and σ is the conductivity (Sm^{-1}).

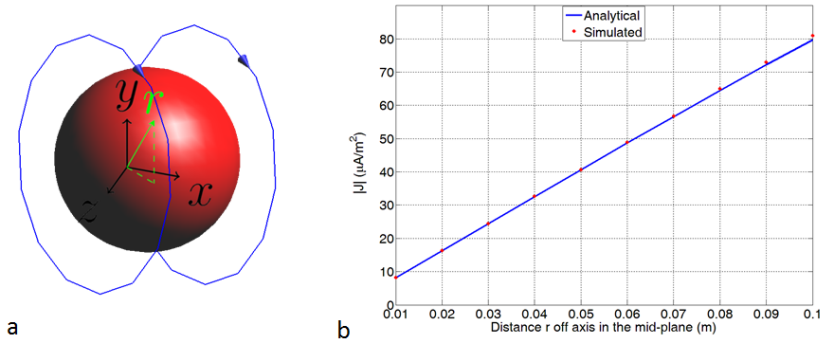

Figure 4.3: a: Homogenous sphere (conductivity 0.1 Sm^{-1}) of radius 0.25 m positioned symmetrically between two concentric current loops forming a Helmholtz pair. The radii of the loops and their center-center separation were 0.35 m. b: Comparison of simulated and analytically derived current density in z = 0 plane against the radial distance r in (m).

4.2.4 Evaluation of the induced electric field

In MRI systems, the stimulus for PNS is mainly the electric field induced in the patient by the changing magnetic field of the gradient system. Since the induction is governed by Maxwell's law, it is therefore influenced not only by the rate of change of the gradient strength but also by patient size, position and conductivity, as well as by the design of the gradient system [4]. To make a fair comparison possible with the previous published works, all the simulations were performed for 1 kHz sinusoidal current with a magnitude of 1 A in the longitudinal and the transverse gradient coils. According to the ICNIRP 2004 on medical magnetic resonance: protection of patients [5], population median rheobases for perception without discomfort, uncomfortable sensation and intolerable sensation are equal to 18.8, 28.3, and 36.9 T/s for the transverse coils, and 28.8, 44.0, and 59.8 T/s for the longitudinal coil. The computed electric fields, at the time derivative of the magnetic flux density rheobase (perception level without discomfort [5]), are scaled, from the calculated field at 1 A and 1 kHz, as follows [27, 28]:

$$E = E_{1kHz} \frac{(\frac{dB}{dt})_{Rh}}{(\frac{dB}{dt})_{1A}} \tag{4.3}$$

Where E is the scaled electric field, E_{1kHz} is the extracted field at 1 kHz, $(\frac{dB}{dt})_{Rh}$ is the rheobase time derivative of magnetic flux assumed to be equal to 18.8 T/s for x- and y-gradient coil, and equal to 28.8 T/s for z-gradient coil according to the ICNIRP 2004 guidelines on medical magnetic resonance: protection of patients [5], and $(\frac{dB}{dt})_{1A}$ is the time derivative of the magnetic field at 0.2 m off the coil center for unit coil current through the coil as specified by the IEC 2010 [7] and is equal to (for 1 kHz sinusoidal):

$$(\frac{dB}{dt})_{1A} = 2\pi 10^3 B_{max,1A} \tag{4.4}$$

$B_{max,1A}$ is the maximum magnetic flux density for a 0.2 m radius cylinder with unit current in the coil.

We used the ICNIRP 2010 [29] approach to determine the induced electric field $E(r_0)$ at a location r_0 as a vector average within a small contiguous tissue cubic volume of 2x2x2 mm^3 of the electric field $E(r_0)$. More specifically:

$$E(r_0) = \frac{1}{V} \int_V E(r) dv \tag{4.5}$$

where 0 < $V \leq 8\ mm^3$ is the volume of lossy tissue within the cube. We also used the 99^{th} percentile value of the electric field for a specific tissue as suggested by the ICNIRP 2010.

The IEC:2010 60601-2-33 standard and the ICNIRP statement on medical

magnetic resonance procedures: protection of patients (2004) prescribes the following limits related to PNS for the induced electric field in the normal operating mode (L_{01}) and in the first level controlled operating mode (L_{12}):

$$L_{01} = 0.8\ (2.2\ \frac{V}{m})(1 + \frac{0.36\ ms}{t_{s,eff}}) \tag{4.6}$$

$$L_{12} = 1.0\ (2.2\ \frac{V}{m})(1 + \frac{0.36\ ms}{t_{s,eff}}) \tag{4.7}$$

Where $t_{s,eff}$ denotes the effective stimulus duration, which is defined as

$$t_{s,eff} = \frac{1}{\pi f} \tag{4.8}$$

for sinusoidal waveforms of frequency f. This leads to $L_{01} = 3.8\ Vm^{-1}$ and $L_{12} = 4.7\ Vm^{-1}$.

4.3 Verification of Low-Frequency Solver

Figure 4.3b shows the simulated and analytically-derived current density within the homogenous sphere for different radial distances in $z = 0$ plane. Using Eqs. (4.1) and (4.2), taking $\sigma = 0.1\,\mathrm{S\ m^{-1}}$, $f = 1$ kHz, it follows that the numerical values simulated at 1 kHz deviate with $0.53 - 0.93\%$ from the analytical value. The applied numerical technique (low frequency solver in SEMCAD) was then verified with an analytical solution for a conducting sphere centered inside a Helmholtz coil. The simulated current density in the mid-plane (z = 0) at different radial distances (from 0.01 m to 0.1 m) agreed with analytically-derived values with deviation less than 1%. We observe that the simulated value tends to overestimate slightly the analytical value due to the spatial variation of the B-field produced by the Helmholtz pair (formula of Eq (4.2) assumed a time-varying uniform B-field while the Helmholtz B-field started lacking its uniformity when the radial distance r approaches 0.1 m for z = 0). The magneto quasi-static low-frequency solver of SEMCAD and its use in exposure investigations was also verified in several studies [9, 30].

4.4 Induced Electric Field: Effect of Coil Type

Table 4.2 shows the calculated electric field in fat and skin (where peripheral nerves are located) for different coils, and Figure 4.4 shows the distribution of the induced electric field. Several observations can be made based on the Table 4.2. The induced electric field is higher in transverse coils (x and y gradient coils) than in longitudinal coil (z gradient coil) despite stronger magnetic flux density produced by the longitudinal coil (e.g. E_{max} Duke, skin: 186 mV m^{-1}, 197 mV

m^{-1}, and 143 mV m^{-1} for x, y, and z gradient coils, respectively). Results also show that difference between transverse and longitudinal coil is more visible in the E_{max} than in the $E_{99\%}$ (difference of 18.5 % to 48 % for E_{max} compared to a difference of 10.1 % to 16.7 % for $E_{99\%}$). The y-gradient coil induced larger internal electric fields. This is due to larger body cross section intercepting the normal component of the magnetic flux density which is in agreement with previously published works [27, 31].

Model	Coil	Tissue	E_{max} (mV m^{-1})	$E_{99\%}$ (mV m^{-1})
Duke	x-coil	Fat	242	94
		Skin	186	85
	y-coil	Fat	272	109
		Skin	197	92
	z-coil	Fat	152	78
		Skin	143	70
Ella	x-coil	Fat	221	79
		Skin	149	72
	y-coil	Fat	248	86
		Skin	172	84
	z-coil	Fat	139	63
		Skin	133	60
Billie	x-coil	Fat	179	59
		Skin	116	57
	y-coil	Fat	191	61
		Skin	130	60
	z-coil	Fat	110	54
		Skin	106	52

Table 4.2: Calculated electric fields (mV m^{-1}) in fat and skin of the body models (1-A current into coil at 1 kHz)

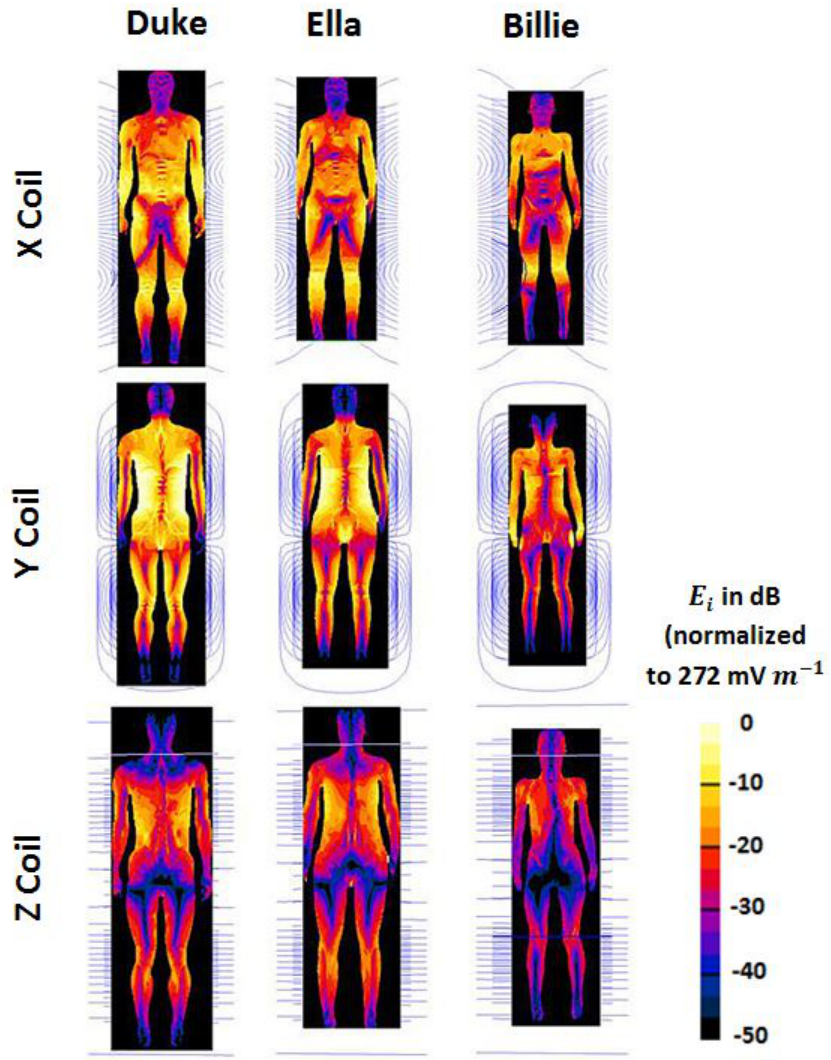

Figure 4.4: Distribution of the internal electric field E_i (dB normalized to 272 mV m^{-1}) for different gradient exposure (from top to bottom : x, y, z, gradients coils) in the Duke, Ella, and Billie models, in the coronal planes y = -0.0215 m, y = -0.026 m, and y = -0.015 m for Duke, Ella, and Billie, respectively.

4.5 Induced Electric Field: Effect of Model Type

The influence of the body model is illustrated in Table 4.2 and Figure 4.4. It is obvious from the table that the induced electric field is higher in Duke than in Ella and Billie for x, y, and z gradient coils and that the maximum induced field decreases with the decrease in the body size (e.g. $E_{99\%}$ fat inside y-gradient coil: 109 mV m^{-1}, 86 mV m^{-1}, and 61 mV m^{-1} for Duke, Ella, and Billie, respectively). Table 4.2 shows also that the difference between $E_{99\%}$ of fat and skin is tighter for Billie (child model) than for adult models. Localized high electric field values occur at the periphery of the volume occupied by the human body, as illustrated in Figure 4.4.

From Faraday's law, it follows that the largest values of circumferentially induced electric fields normal to the direction of applied magnetic field will localize in the outermost body surfaces [15]. The gradient fields are the largest in absolute value near the coils which results in higher rate of change and thus, the induced electric field through Faraday law will be maximum near the outermost body surfaces. It follows that the peripheral nerves in the skin are exposed to the strongest electric fields.

Results show that the human body model and the body size in general, is a primary factor for the induced electric fields. The maximum induced field occurred for the largest size of the body model (Duke). This behavior was also reported in several studies of exposure to uniform magnetic field (see [32] for example). Differences in shape and anatomy between the models are also a factor affecting the induced field but remain less important than the size of the model. [33]

The electric field is greater in fat than in skin. This due to the conductivity being lower in the fat compared to the skin (0.04 S m^{-1} for fat and 0.2 S m^{-1} for skin), and was already explained and reported in several published research. Chen et al [33] demonstrated that a high-low-high layered tissue conductivity transition can result in an enhancement of the induced E-fields in the less conductive region as shown in Figure 4.5. The sphere represents a larger organ while the dish layer represents a potential tissue-to-tissue interface with conductivity contrast. Conductivity values σ1 and σ1 are assigned to the sphere and the transition layer,respectively. It is observed that the induced E-fields are significantly enhanced in the heterogeneous model compared to the homogeneous model. In our case, the transition fo the E-field between high (skin conductivity of 0.2 S m^{-1})-low (fat conductivity of 0.04 S m^{-1})-high (muscles conductivity of 0.32 S m^{-1}) conductivity transition can explain the highest induced E-field in the fat (region of low conductivity).

Figure 4.4 indicates that the largest volumes of high intensity electric field are in the torso and in the outermost body surfaces, which is the body region where

the greatest number of stimulations were reported by the subjects [28].

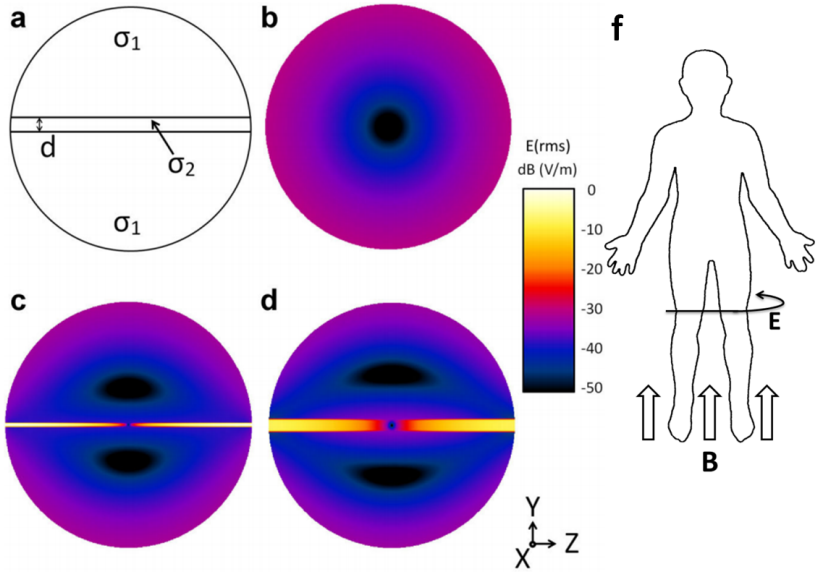

Figure 4.5: Spherical canonical model with tissue transition layer of thickness d. (a) Model configuration for a conductivity ratio of σ1:σ2 = 100:1 and uniform grid size of 0.5 mm, and the E(average) distributions in (b) homogeneous model, (c) d = 2 mm, and (d) d = 10 mm. (f) Schematic representation of the E-field and B-field showing E-field circulating the body model and pass through the skin-fat-muscles interface normally. Figure adapted from [33]

4.6 Induced Electric Field: Effect of Skin Conductivity

Table 4.3 shows E_{max} and $E_{99\%}$ for Duke inside x, y, and z gradient coils using the skin conductivity of 0.1 S m^{-1} and 0.2 S m^{-1}. The peak-induced E-field is higher for the skin conductivity of 0.1 S m^{-1} compared to the skin conductivity of 0.2 S m^{-1}. This difference is highlighted in the E_{max} rather than in the $E_{99\%}$ value. The skin conductivity does not have a great impact on the induced electric field for the 99% value (as an averaged value) which is in agreement with the works of the De Santis et al. [18]. They reported that any value of the skin conductivity between the range of 0.1-0.7 S m^{-1} will not considerably alter the spatial average E-fields. However, the maximum electric field decreased with the skin conductivity value. Table 4.3 shows that the $E_{99\%}$ is higher for z-coil compared to other coils (143 mV.m^{-1}). This can be due to some singularity in the $E_{99\%}$ extraction.

Model	Coil	Tissue	E_{max} (mV m^{-1})	$E_{99\%}$ (mV m^{-1})
Duke	x-coil	Skin (0.1 $S\ m^{-1}$)	198	87
		Skin (0.2 $S\ m^{-1}$	186	85
	y-coil	Skin (0.1 $S\ m^{-1}$)	215	96
		Skin (0.2 $S\ m^{-1}$	197	92
	z-coil	Skin (0.1 $S\ m^{-1}$)	154	143
		Skin (0.2 $S\ m^{-1}$	143	70

Table 4.3: Calculated electric fields (mV m^{-1}) in fat and skin for Duke model using skin conductivity of 0.1 S m^{-1} and 0.2 S m^{-1} (1-A current into coil at 1 kHz)

4.7 Compliance with the Guidelines

The calculated $B_{max,1A}$ is equal to 62.87 μT, 60.37 μT, and 84.39 μT, for x, y and z gradient coil, respectively. The given flux density is the maximum value within the volume of a cylinder with 0.2 m radius and a height of 0.2 m. Induced electric fields are computed from Table 4.2 using Equation 4.3. Calculations are summarized in Table 4.4. Table 4.4 shows that the E_{max} exceeds the standards basic restrictions for all the models and the coils (5.5 Vm^{-1}- 13.5 V m^{-1}). The $E_{99\%}$ is within the normal operating mode guidelines for the child model inside all the coils (2.7 V m^{-1} - 3 m^{-1}) and the adult female inside x and z gradient coils (3.3 V m^{-1} - 3.8 V m^{-1}). The $E_{99\%}$ exceeds the normal operating mode guidelines but remains within the first level controlled operating mode for the adult female model inside y-gradient coil (4.2 V m^{-1} - 4.3 V m^{-1}), and the adult male model inside x and z gradient coils (4.2 V m^{-1} - 4.5 V m^{-1}). Only the $E_{99\%}$ of the Duke model inside the y-gradient coil exceeds the first level controlled operating mode ($E_{99\%}$ = 5.4 V m^{-1}).

The induced electric fields for PNS computed in this Chapter are in the range of 2.7 V m^{-1} - 5.4 V m^{-1}. These values are in agreement with published studies [27, 31]. In [31] , an averaged value of E = 4.2 V m^{-1} was reported and estimated 2.9 V m^{-1} - 5.8 V m^{-1} was reported in [27]. Compliance with the ICNIRP 2004 and IEC 2010 guidelines for the normal operating mode (L_{01}) guidelines was recorded for the child model inside all the coils and the adult female inside x and z gradient coils. Results for the adult female model inside y-gradient coil and the adult male model inside x and z gradient coils exceeded the L_{01}, but remained within the first level controlled operating mode (L_{12}). The $E_{99\%}$ of the adult male model inside the y-gradient coil exceeded the L_{01} and L_{12} by a factor of 1.38 and 1.1 respectively. We note that we have focused on the configuration of human bodies centered with respect to the coils; the sensitivity of the PNS sensation thresholds to the human body position was already investigated by [27, 28]. So et al. concluded

that the position of the human body inside the coils influences the magnitude of the induced electric field. The changes, however, are typically below 20% for most measures and less than 5% for the average value of the electric field for a given tissue in a given coil [27].

Model	Coil	Tissue	E_{max} (mV m^{-1})	$E_{99\%}$ (mV m^{-1})
Duke	x-coil	Fat	11.5	4.5
		Skin	8.9	4
	y-coil	Fat	13.5	5.4
		Skin	9.8	4.6
	z-coil	Fat	8.3	4.2
		Skin	7.8	3.8
Ella	x-coil	Fat	10.5	3.8
		Skin	7.1	3.4
	y-coil	Fat	12.3	4.3
		Skin	8.5	4.2
	z-coil	Fat	7.6	3.4
		Skin	7.2	3.3
Billie	x-coil	Fat	8.5	2.8
		Skin	5.5	2.7
	y-coil	Fat	9.5	3
		Skin	6.4	3
	z-coil	Fat	6	2.9
		Skin	5.8	2.8

Table 4.4: Induced electric fields (V m^{-1})

4.8 Conclusions

In this Chapter, we have modeled the exposures of male, female and child patients to pulsed gradient fields typically used in MRI systems. These gradients coils are intended to be models of currently available cylindrical MRI systems, but we do not claim that we covered all gradient sets on the market and therefore we provided indicative results only. The y-gradient tends to induce more fields in the models than the other coils. The strongest levels of field exposure are observed for the adult male inside the y-gradient coil. The internal electric fields, when the patients are inside the gradient coils are within the first level controlled operating mode of the ICNIRP 2004 and IEC 2010 guidelines, except for the adult male

inside the y-gradient coil. Investigations such as these will help inform compliance of clinical procedures.

References

[1] John F. Schenck. *Physical interactions of static magnetic fields with living tissues*. In Progress in Biophysics and Molecular Biology, volume 87, pages 185–204, 2005.

[2] Frank G. Shellock. *Radiofrequency energy-induced heating during MR procedures: A review*, 2000.

[3] D J Schaefer, J D Bourland, and J A Nyenhuis. *Review of patient safety in time-varying gradient fields*. J Magn Reson Imaging, 12(1):20–29, 2000.

[4] J. P. Reilly. *Peripheral nerve stimulation by induced electric currents: Exposure to time-varying magnetic fields*, 1989.

[5] ICNIRP. *Medical magnetic resonance (MR) procedures: protection of patients*. Health physics, 87:197–216, 2004.

[6] *IEEE standard for safety levels with respect to human exposure to electromagnetic fields, 0-3 kHz, C95.6-2002, New York: Institute of Electrical and Electronics Engineers; 2002:43)*.

[7] *IEC (Edition 3.0 2010) 60601-2-33 Medical electrical equipment - Part 2-33: Particular requirements for the basic safety and essential performance of magnetic resonance equipment for medical diagnosis)*.

[8] Martin Bencsik, Richard Bowtell, and Roger M. Bowley. *Using the vector potential in evaluating the likelihood of peripheral nerve stimulation due to switched magnetic field gradients*. Magnetic Resonance in Medicine, 50(2):405–410, 2003.

[9] Weihua Mao, Blaine A. Chronik, Rebecca E. Feldman, Michael B. Smith, and Christopher M. Collins. *Consideration of magnetically-induced and conservative electric fields within a loaded gradient coil*. Magnetic Resonance in Medicine, 55(6):1424–1432, 2006.

[10] L K Forbes and S Crozier. *On a possible mechanism for peripheral nerve stimulation during magnetic resonance imaging scans.* Physics in medicine and biology, 46(2):591–608, 2001.

[11] Huawei Zhao, Stuart Crozier, and Feng Liu. *Finite difference time domain (FDTD) method for modeling the effect of switched gradients on the human body in MRI.* Magnetic resonance in medicine : official journal of the Society of Magnetic Resonance in Medicine / Society of Magnetic Resonance in Medicine, 48(6):1037–42, 2002.

[12] O Heid inventor. *Siemens Aktiengesellschaft, assignee. Magnetic resonance apparatus with compensation of fields arising due to eddy currents*. US patent 6844733 B2, January 18, 2005.

[13] Mai Lu and Shoogo Ueno. *Dosimetry of exposure of patients to pulsed gradient magnetic fields in MRI*. In IEEE Transactions on Magnetics, volume 47, pages 3841–3844, 2011.

[14] International Commission on Non-Ionizing Radiation Protection. *GUIDELINES FOR LIMITING EXPOSURE TO TIME-VARYING ELECTRIC, MAGNETIC, AND ELECTROMAGNETIC FIELDS (UP TO 300 GHz)*. Health physics, 75(5):535, 1998.

[15] Stuart Crozier, Hua Wang, Adnan Trakic, and Feng Liu. *Exposure of workers to pulsed gradients in MRI*. Journal of Magnetic Resonance Imaging, 26(5):1236–1254, 2007.

[16] Yan Li, Jeff W Hand, Tim Wills, and Jo V Hajnal. *Numerically-simulated induced electric field and current density within a human model located close to a z-gradient coil.* Journal of magnetic resonance imaging : JMRI, 26(5):1286–95, 2007.

[17] Gernot Schmid, Stefan Cecil, and Richard Überbacher. *The role of skin conductivity in a low frequency exposure assessment for peripheral nerve tissue according to the ICNIRP 2010 guidelines*. Physics in Medicine and Biology, 58(13):4703–16, 2013.

[18] Valerio De Santis, Xi Lin Chen, Ilkka Laakso, and Akimasa Hirata. *An equivalent skin conductivity model for low-frequency magnetic field dosimetry*. Biomedical Physics & Engineering Express, 1(1):015201, 2015.

[19] *SEMCAD X. Simulation platform for electromagnetic and thermal dosimetry, Schmid & Partner Engineering AG, Switzerland. www.semcad.com.* 2015.

[20] Michael Poole and Richard Bowtell. *Novel gradient coils designed using a boundary element method.* Concepts in Magnetic Resonance Part B: Magnetic Resonance Engineering, 31(3):162–175, 2007.

[21] *NHS Purchasing and Supply Agency. Report 06006 3T MRI Systems*. 2007.

[22] Andreas Christ, Wolfgang Kainz, Eckhart G Hahn, Katharina Honegger, Marcel Zefferer, Esra Neufeld, Wolfgang Rascher, Rolf Janka, Werner Bautz, Ji Chen, Berthold Kiefer, Peter Schmitt, Hans-Peter Hollenbach, Jianxiang Shen, Michael Oberle, Dominik Szczerba, Anthony Kam, Joshua W Guag, and Niels Kuster. *The Virtual FamilyâĂŤdevelopment of surface-based*

anatomical models of two adults and two children for dosimetric simulations. Physics in Medicine and Biology, 55(2):N23–N38, 2010.

[23] Hasgall P, Neufeld E, Gosselin M, Klingenbock A, and Kuster N. *IT'IS database for thermal and electromagnetic parameters of biological tissues*. 2012.

[24] Gabriel C. *Compilation of the dielectric properties of body tissues at RF and microwave frequencies. Technical Report AL/OE-TR-1996-0037, Occupational and Environmental Health Directorate. Radiofrequency Radiation Division, Brooks Air Force Base, Texas.* 1996.

[25] Montgomery DB and J Terrell. *Some useful information for the design of air core solenoids. National Magnet Laboratory, M.I.T. Report. AFOSR-1525.* 1961.

[26] Smythe WR. *Static and Dynamic Electricity, 2nd*. page 266, 1968.

[27] Poman P M So, Maria A. Stuchly, and John A. Nyenhuis. *Peripheral nerve stimulation by gradient switching fields in magnetic resonance imaging*. IEEE Transactions on Biomedical Engineering, 51(11):1907–1914, 2004.

[28] Nyenhuis JA, Bourland JD, Kildishev A V, and Scaefer DJ. *Health effects and safety of intense MRI gradient fields. Magnetic Resonance Procedures: Health Effects and Safety, 1st edition*. 2001.

[29] ICNIRP. *Guidelines for limiting exposure to time-varying electric and magnetic fields (1 Hz to 100 kHz).* Health physics, 99(6):818–36, 2010.

[30] J F Bakker, M M Paulides, E Neufeld, A Christ, X L Chen, N Kuster, and G C van Rhoon. *Children and adults exposed to low-frequency magnetic fields at the ICNIRP reference levels: theoretical assessment of the induced electric fields*. Physics in Medicine and Biology, 57(7):1815–1829, 2012.

[31] F. Liu, H. Zhao, and S. Crozier. *On the Induced Electric Field Gradients in the Human Body for Magnetic Stimulation by Gradient Coils in MRI*. IEEE Transactions on Biomedical Engineering, 50(7):804–815, 2003.

[32] Caputa K, Dimbylow PJ, Dawson TW, and Stuchly MA. *Modelling fields induced in humans by 50/60 Hz magnetic fields: reliability of the results and effects of model variations*. Phys Med Biol, 47:1391–1398, 2002.

[33] Xi-Lin Chen, Stefan Benkler, Nicholas Chavannes, Valerio De Santis, Jurriaan Bakker, Gerard Van Rhoon, Juan Mosig, and Niels Kuster. *Analysis of human brain exposure to low-frequency magnetic fields: A numerical assessment of spatially averaged electric fields and exposure limits*. Bioelectromagnetics, 34(5):375–384, 2013.

Part III

Numerical Modelling of Auricular Vagus Nerve Stimulation

5

Numerical Modelling of Auricular Vagus Nerve Stimulation

5.1 Introduction

The vagus nerve is the longest and most complex of the cranial nerves, innervating organs of the thorax, neck, abdomen, and reaching the colon [1]. It is an important component of the autonomic nervous system and plays a major role in the regulation of metabolic homeostasis. Its sympathetic and parasympathetic branch controls and regulates the function of various glands, organs, and involuntary muscles throughout the body [2]. Stimulation of the cervical vagus nerve by implanted stimulation devices gained importance as a treatment for therapeutic refractory epilepsy, major depression, and congestive heart failure [1, 3]. To cope with the associated risks, less invasive techniques were developed. Those include the percutaneous stimulation of the auricular branch of the vagus nerve (pVNS) [4, 5]. By using needle electrodes in targeted regions of the auricle [6], one can easily access these nerve branches [7]. By this, a minimally-invasive way of neuromodulative intervention is available. Current clinical applications include the treatment of chronic pain [8] or peripheral arterial disease (PAD) [9]. Specific stimulation of afferent vagus nerve fibers can activate autonomous modulation [10]. Sympathetic and parasympathetic branches of the autonomic nervous system modulate heart rate, blood pressure, or vascular tone [11]. A favorable parasympathetic/vagal stimulation may thus downregulate vascular tone [2], increase blood perfusion [9, 12], and downregulate inflammation [13, 14], all highly

beneficial for instance in the treatment of PAD.

Main shortcoming of current applications in pVNS is the unguided/empirical selection of both stimulation regions and parameters with unknown variation of the therapeutic effect. However, high specificity of stimulation seems to be of huge importance due to the dense innervation of the auricle with nerve fibers of different origin [6], which all may react differently to stimulation and can elicit opposite physiological reactions [15].

Simulations of electromagnetic fields excited in human biological tissue by artificial neurostimulation exist in literature. However, these studies are limited to the most common types of neurostimulation, e.g., for deep brain stimulation [16, 17], spinal cord stimulation [18], peripheral nerve stimulation [19], and transcranial magnetic stimulation [20, 21]. These studies provide us with a better understanding of the electric potential and current distributions in the biological tissues surrounding the stimulation electrodes. Some studies assume a simplified neural network that distributes the axons uniformly around the stimulation electrode with one and the same direction for all axons, see e.g., [22]. Using the potential distribution, it is then possible to calculate which axons are effectively stimulated. However, neural stimulation also heavily depends on the orientation of the externally applied electric field with respect to the orientation of the axon. Therefore, an improvement is to use the actual, often winding geometry of nerve axons in the simulation, as given in e.g., [16, 23].

The goal of this chapter is to establish, a realistic model of the pVNS application and investigate the effect of the electrodes' depth and position, as well as the stimulation pattern on the excitation threshold in single and bundled axons. To this aim, numerical simulations are carried out, using a realistic high-resolution model of a human ear including spatial model of major blood vessels and nerves. The electric field distribution in the ear and its spatial derivative are then calculated and the stimulation thresholds for each configuration is calculated and compared. More specifically, we will use the titration mechanism (which consists of stimulating the nerve with pulses of increasing amplitudes, to determine the threshold above which an action potential is generated) to compared different stimulation patterns and to asses the effect of the electrodes' depth and position on the stimulation thresholds. In Section 5.2, the simulation platform, numerical model, and different configurations of the electrodes are described. We also verified the simulation model with analytical results using the myelinated nerve model. Section 5.3 is dedicated to the electric fields distribution in the ear and its spatial gradient along the nerves. Section 5.4 presents results of the effect of different stimulation patterns using mono-phasic, bi-phasic, anodic, and cathodic pulses. In Section 5.5, the percentage of activated axons and stimulation thresholds to obtain 100 % axon activation are presented for each axon population with discussion of the effect of the electrode depth and position on the percentage of stimulated axons. Finally,

conclusions are drawn in Section 5.6.

5.2 Materials and Methods

5.2.1 Simulation Platform

Numerical simulations of pVNS were performed in Sim4Life [28]. The gridding was calculated using the stationary currents model of Sim4Life. The model was meshed approximately to 4.105 Mcells. Boundary conditions are set using Neumann conditions with a constant flux equal to zero (the derivative of a solution is set to zero on the boundary of the domain) to simulate an infinite system. The boundary settings of the electrodes are set using Dirichlet conditions (value of the solution is set to a constant value on the boundary of the domain) with a constant potential.

We performed all neuronal simulations using the neuronal tissue models from Sim4Life. The models (T-NEURO) enable the dynamic modeling of EM-induced neuronal activation and inhibition using either complex, multi-compartmental representations of axons, nerves as bundles of axons, and neuronal networks with varying channel dynamics, or generic models.

Sim4Life uses the NEURON solver (Yale University, CT, USA) to simulate the effect of electromagnetic fields on neuronal dynamics. It offers the possibility to directly couple the results of EM simulations with the neuronal dynamics solver. The NEURON solver offers the possibility of an external modulating pulse *a(t)*, which can be superimposed on the static field calculated from the EM fields sensed by the axon. Interaction of a nerve fiber or a neuron with an electromagnetic field results in its membrane electrical activity modification. These changes, when exceeding the stimulation thresholds, can fire action potentials propagating along the neuronal body. Several factors can be decisive for the neuronal response initiation. The orientation, geometric configuration of a neuron within the EM field, and the chosen transmembrane mechanism are key factors when considering the reaction of the neuron to the EM fields. Rapid changes and inhomogeneity of the EM field can result in high localized potential gradients along the nerve, which might results in the membrane depolarization and action potential generation if the depolarization is of sufficient strength.

We used the titration mechanism to calculate the minimum voltage needed to depolarize the axons. Titration is the process of stimulating an axon with a series of pulses of increasing (or varying) intensity to find the threshold above which a single action potential is generated, introducing an additional scaling factor that is varied until a response is detected. The final threshold field is the product of the static potential from the initial EM field ϕ, the modulating pulse $a(t)$, and the

titration factor T:

$$\phi_T(t) = \phi.T.a(t) \tag{5.1}$$

T factor can be considered as scaling factor to indicate the proportion or multiple of the actual modulated electric potential needed to generate an action potential. The fact that electrostatic equations are linearly separable into linear temporal components and non-linear spatial components makes the titration approach valid and suitable for the determination of axons' activation thresholds. We used the spatially extended nonlinear node (SENN) [25, 31] model for transmembrane mechanisms to simulate the time-response of an axonal membrane to external fields.

5.2.2 Verification of the Neuronal Dynamics Solver

The objective of this section is to compare analytically derived results with simulations to verify the neuronal dynamics solver. Our approach is to reproduce results of the SENN neuro-electrical model described in [26]. The configuration used in [26] includes a 20 μm fiber stimulated by a point electrode situated 2 mm from the central node. The fiber is excited by a cathodic rectangular mono-phasic current of 0.1 ms duration. The numerical model (Figure 5.1) is composed of a line representing an axon placed 2 mm away from a point electrode situated in a tissue simulating medium. The point electrode, tissue medium, and axon fiber are represented by a sphere (0.1 mm radius), cube (10 mm side), and line (20 mm). The boundary settings of the electrode were set using Dirichlet conditions with a constant potential of 1 V. Threshold for depolarization, temperature, initial potential, axon diameter, and the nodal gap were set to 80 mV, 34 °C, -70 mV, 20 μm, and 2.5 μm, respectively. The axon was stimulated with cathodic rectangular mono-phasic pulse (amplitude = -1 V, duration 0.1 ms).

Simulation results show that the first spike of the AP occurs at the axon central node (the nearest node to the electrode, Figure 5.2) with a titration factor of 1.64. To obtain the excitability threshold, we should first calculate the current applied to the cellular membrane of the axon, which is calculated by integrating the current density over a region of interest S

$$I_{(A)} = \int_s JdS \tag{5.2}$$

The current density J is related to the electric field by

$$J_{(\frac{A}{m^2})} = \sigma E \tag{5.3}$$

where σ is the electric conductivity of the medium. By integrating the current I at the surface of a sphere of radius r, we obtain

$$I = 4.\pi.r^2.\sigma.E = 0.425\ mA \tag{5.4}$$

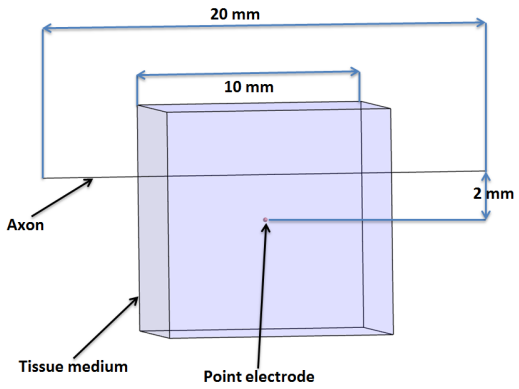

Figure 5.1: Numerical set up used for the validation. The point electrode (reed sphere) is 2 mm from the axon.

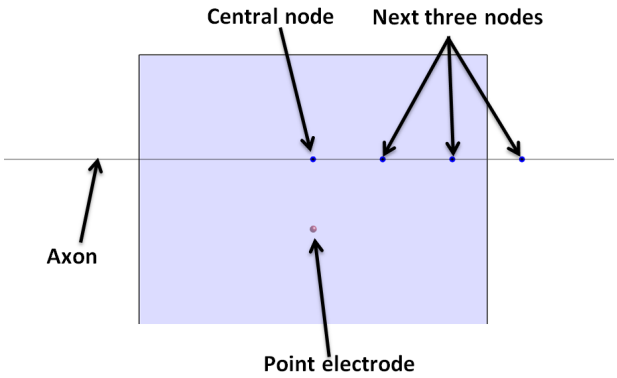

Figure 5.2: Position of the central node and the next three nodes used to extract the action potential.

The excitability threshold I_T is then calculated using equation 5.1:

$$I_T = I.T.a(T) = 0.7\ mA \tag{5.5}$$

The value of the excitability threshold I_T is in a good agreement with the value of 0.68 mA published in [26]. Reilly et al. also reported that the AP started from the axon central node, which is also the case for the simulated model.

Figures 5.3 and 5.4 show the response of the SENN model and the neuronal dynamics solver to cathodic rectangular mono-phasic current of 0.1 ms duration.

Solid lines, curves (a-c) in Figures 5.3 and 5.4, show the response at the central node for three levels of current ($0.8I$, I, and $1.2I$ for a, b, and c). The vertical axis applies to the transmembrane potential (V_n) relative to the resting potential as used in [26]. Transmembrane potential of 0 V will then be considered equal to the resting potential (-70 mV). Negative V_n indicate hyperpolarization while positive values indicate depolarization. The horizontal axis indicates the time elapsed following the onset of the mono-phasic pulses of 0.1 ms duration. Solid lines, curves (a-c) in Figures 5.3 and 5.4, show the action potential development at the first node to be excited (the central node in Figure 5.2). The broken lines (d-f) show the AP at the next three nodes in response to the pulse with threshold amplitude (next three nodes in Figure 5.2). Curve (c) shows the AP at 20 % above threshold while curve (a) is for the pulse at 80 % of the threshold amplitude. Curve (a) shows the AP at the threshold current. Time delay between the nodes from simulations (Figure 5.4), indicates a propagation velocity of 47.6 m/s, which is in a good agreement with the published value of 43 m/s in [26]. Comparison between Figure 5.3 and Figure 5.4 shows a good agreement between the calculated results with the SENN model in [26] and the simulated results provided by the neuronal dynamic solver.

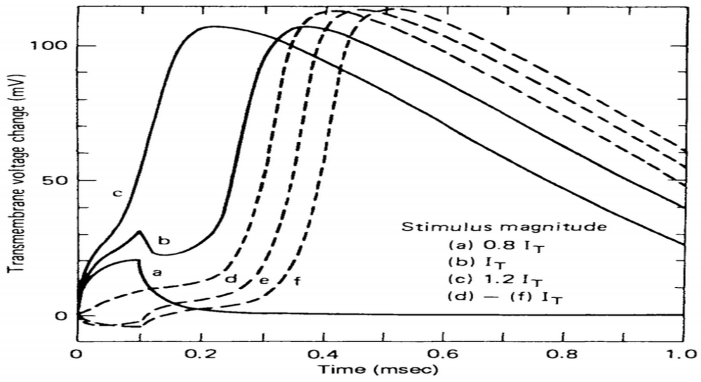

Figure 5.3: Response of SENN model to rectangular mono-phasic current of 0.1 ms duration, 20 µm-diameter fiber, point electrode 2 mm from central node. Solid lines show response at node nearest electrode for three levels of current. I_T denotes threshold current. Broken lines show propagated response at next three adjacent nodes for a stimulus at threshold. (From Reilly et al. [26]).

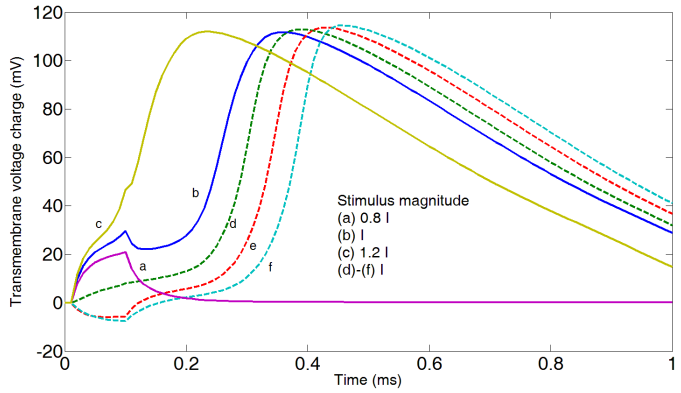

Figure 5.4: Response of neuronal dynamics solver model to rectangular mono-phasic current of 0.1 ms duration, 20 µm-diameter fiber, point electrode 2 mm from central node. Solid lines show response at node nearest electrode for three levels of current. I denotes threshold current. Broken lines show propagated response at next three adjacent nodes for a stimulus at threshold.

5.2.3 Ear and Nerves Modelling

The system under investigation consisted of a realistic high resolution model of a human ear (spatial resolution 3 mm), 3 electrodes, and a spatial model of major

blood vessels and nerves. Locations of the electrodes are based on positions used in clinical practice and on the innervation of the auricular branch of the vagus nerve given in [6]. One electrode is considered as a reference (zero potential), while the two other electrodes are considered as stimulating electrodes. Figure 5.5a shows a schematic overview of the numerical model. The conductivity of the vessels was set to 0.7 S/m [28] and the ear conductivity to 0.2 S/m based on a recent work of Santis et al. [32]. The boundary settings of the electrodes were set using Dirichlet conditions with a constant potential.

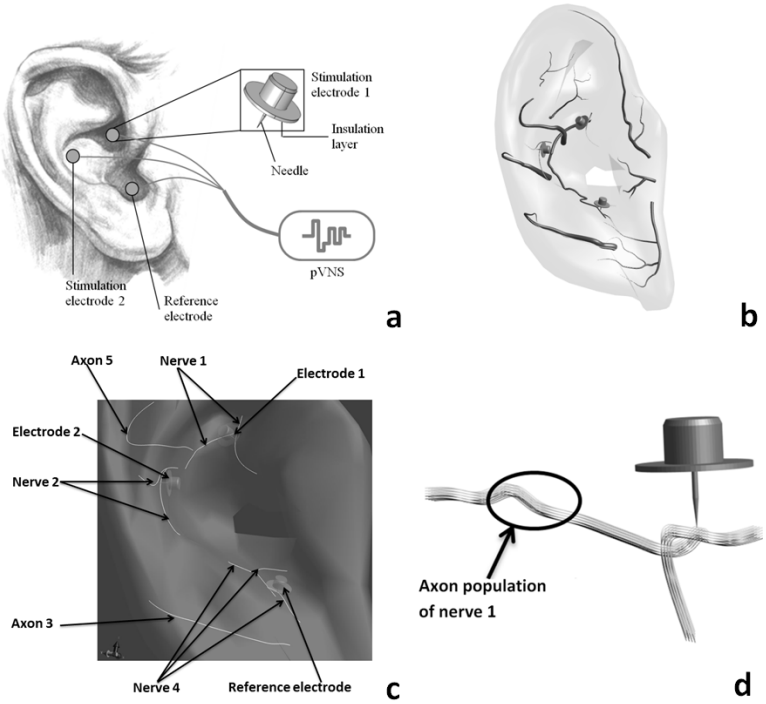

Figure 5.5: Numerical model of the pVNS application. (a) Scheme of the application. (b) Auricle, vessels, nerves, and the electrodes. Vessels and nerves are inside the ear and not on the surface of the ear. (c) Locations and shapes of the nerves. (d) Activation of the axon population of N1 stimulated by anodic mono-phasic pulses. Dark color indicates inactivated axons.

Figure 5.5b shows the locations of the vessels in the ear while Figure 5.5c shows the locations and shapes of the nerves (N) and axons (A) inside the ear model. Nerve1 (N1), nerve2 (N2), and nerve4 (N4) are branching nerves, while axon3 (A3) and axon5 (A5) are non-branching single axons. Locations of the vessels and nerves/axons are based on the vascularization of the auricle and the nerve supply of the human auricle studied in [6, 33, 34]. In fact, distribution of

nerves and vessels in the auricle is highly individual, thus a typical distribution was selected. The threshold for depolarization, temperature, initial potential, axon diameter, and the nodal gap were set to 80 mV, 34 °C, -70 mV, 10 μm, and 2.5 μm, respectively [35]. The axon diameter at node d and the internodal distance L are related to the fiber diameter D by Eqs. 1.10 and 1.11 . Simulations were carried out with realistic stimulation pulses [5]. Nerves were stimulated using two types of pulses: anodic and cathodic single cycle mono-phasic (amplitude = 1 V, duration 1 ms) and bi-phasic (amplitude = ± 1 V, duration 1 ms) pulses (Figure 5.6). This amplitude of 1 V will be rescaled using the titration factor for each configuration based on the Equation 5.1. For axon population simulations, 20 axons were defined

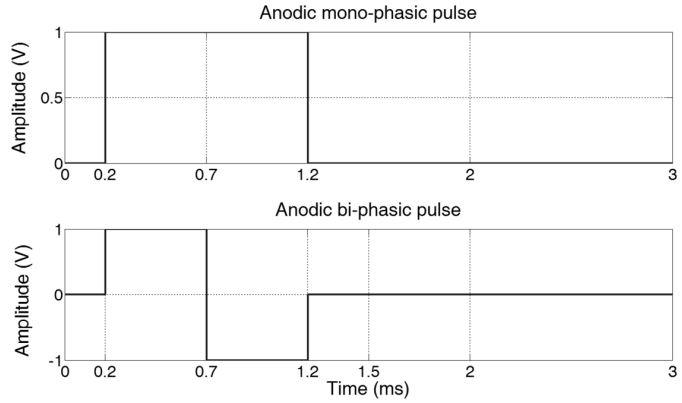

Figure 5.6: Mono-phasic and bi-phasic stimulation pulses.

from a rectangular seed region to form N1, N2, and N4; approximately 0.3 x 0.3 mm in size to generate a dense population of 60 axons in total (see Figure 5.5d). This number of axons is based on the work of Safi et al [36] who counted the numbers of thick myelinated Aβ-axons in the auricular branch of the vagus nerve. Results of [36] are based on sixteen bodies (11 males, 5 females, median age 73 years, range 50-96 years). The auricular branch of the vagus nerve, cervical vagus nerve, recurrent laryngeal nerve and thoracic vagus nerve were dissected from embalmed bodies. Numbers and calibers of myelinated axons were analyzed in semithin sections [36]. Vessels and nerves are just below the epidermis layer of the skin. The epidermis thickness is about 0.07 mm at the thinnest parts of the body (ear's skin, eyelids) [37]. We then used a depth of 0.07 mm for the nerves/vessels inside the ear. Point sensors for depolarization were placed each 1 mm for all the nerves/axons with respect to the used internodal distance of 1 mm. The SENN model judges that an excited state exists if a specified number of contiguous nodes successively attains a depolarization value of 80 mV. Typically, the specified number is three to demonstrate action potential propagation [35]. In

our simulation, we check the AP propagation along all the branching nerves and axons using the point sensors placed each 1 mm.

5.2.4 Electrodes' Position and Depth

To investigate the effect of the needle penetration depth on the percentage of activated axons, we varied the needle penetration depth of electrode1 (E1) and electrode2 (E2) inside the ear from 1.5 mm to 0.8 mm in steps of 0.1 mm (see Figure 5.7). The lateral position of the electrodes was also changed from the original position by ± 1 mm in the y and z directions, with a maximum of (± 1 mm, ± 1 mm). Here the needle penetration was kept at the maximum value, i.e., the insulation layer was always in contact with the ear.

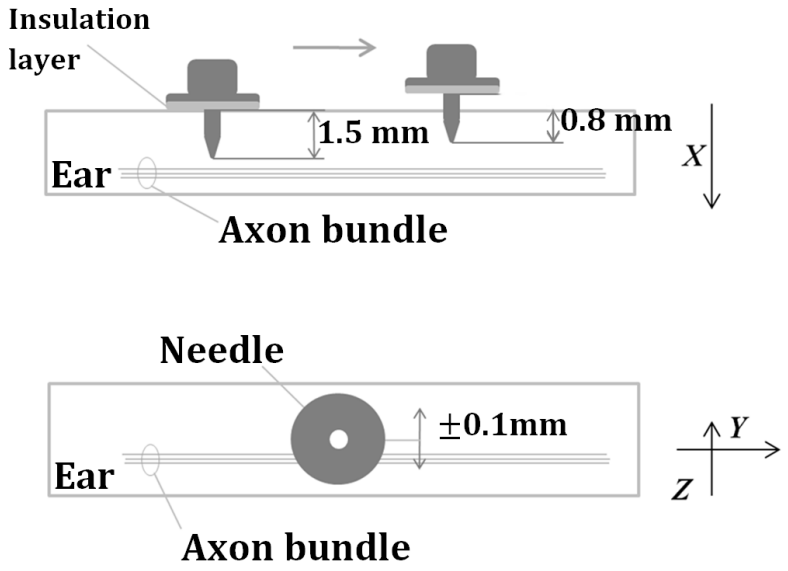

Figure 5.7: Scheme of the change in penetration depth and position with respect to the axon bundle.

5.3 Electric Field Distribution

Figure 5.8 shows the resulting electric field distribution in dB normalized to 100 V/m. The E-field is directed from the anodic electrodes (E1 and E2, blue electrodes at 1 V) to the reference electrode (green electrode at 0 V) with maximum values near the electrodes (99 V/m near the reference electrode, 82 V/m and 84 V/m near E1 and E2, respectively), and is penetrating inside the ear, vessels

and nerves. Electric field distribution shows that higher electric field values appear near the needle, which is due to the point effect on the needle. N4 branches are at locations with higher electric fields values compared to the other nerves.

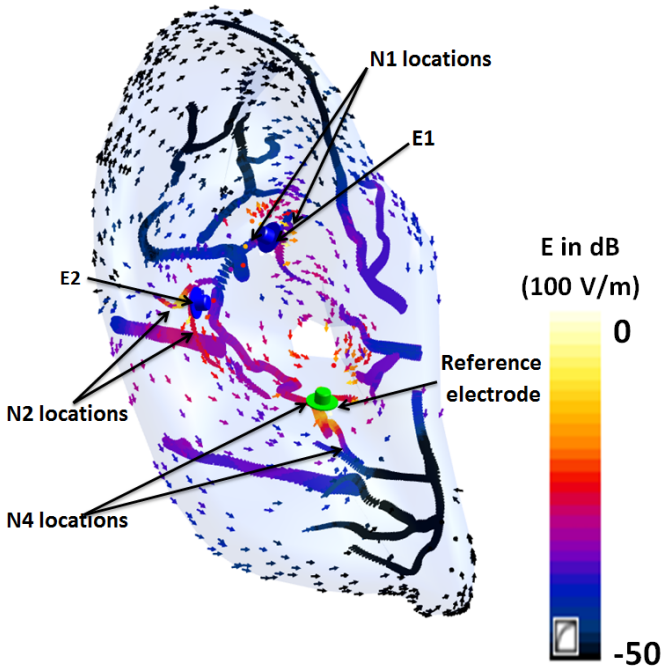

Figure 5.8: Electric field distribution, in dB normalized to 100 V/m. Blue electrodes have a potential of 1 V. The green electrode is the reference (0 V).

Figure 5.9 shows the spatial distribution of the E-field and its first derivative along N1, N2, and N4. The horizontal axis indicates the longitudinal distance along the nerve's branch triggering the first action potential. This Figure applies to a cathodic monopolar stimulus electrode. For the anodic monopolar electrode stimulus, the diagram in Figure 5.9 would be flipped around the horizontal axis.

Figure 5.9a shows that the electric fields reaches its maximum value (77 V/m) at the point x = 4 mm. Figure 5.10, shows that the AP started at the bend point of the nerve which is also the location of the maximum E-field. Thus bend-mode of stimulation is the dominant mechanism of excitation for the nerve N1. The maximum positive value of the E-field for N1 in the anodic configuration is 35 V/m at x = 3 mm(Figure 5.9 flipped around the horizontal axis) which is less than the maximum value of 77 V/m for the cathodic stimulation. The spatial gradient of the internal E-field reaches higher maximum values for the cathodic stimulation

compared to the anodic stimulation for N2 (Figure 5.9e: 0.2 (x = 3.7 mm) and 0.1 (x = 4.5 mm) for cathodic and anodic, respectively), and the inverse is true for N4 (Figure 5.9f: 0.74 (x = 5 mm) and 1 (x = 4.5 mm) for cathodic and anodic, respectively).

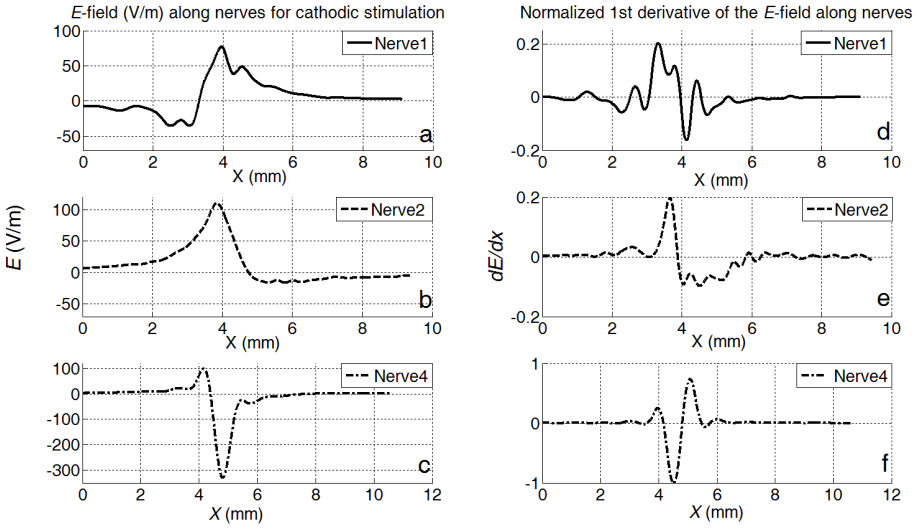

Figure 5.9: Spatial distribution of E-field and its 1^{st} derivative along N1, N2, and N4 (the activated nerves). The 1^{st} derivative was normalized to the maximum absolute value of the N4' 1^{st} derivative.

5.4 Effect of the Stimulation Patterns

Table 5.1 lists the required pulse amplitude to activate the nerves/axons as a function of the stimulation pattern. The voltage for each nerve/axon is related to the anodic mono-phasic voltage, and Δ_T is the percentage of the stimulation thresholds related to the anodic mono-phasic voltage of each nerve/axon. Branching nerves (N1, N2, and N4) are considered activated when a single axon of the nerve is activated and the generated action potential is propagated to all the branches of the nerves (measured by extracting action potential and titration factor in all the nodes of the nerve's branches) [35]. For an amplitude of 1 V, the nerves N1, N2 and N4 will be activated (generation and propagation of the action potential, threshold in Table 5.1 less than 1 V), while A3 and A5 require amplitudes of 14 V and 3.5 V, to be activated, respectively. A3 and A5 axons are on the back of the ear and thus less exposed to the electric field generated by the electrodes positioned in the front of the ear.

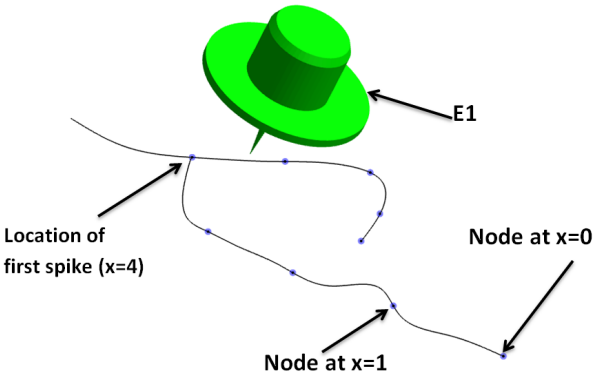

Figure 5.10: Location of the node where the AP started for the N1 nerve. N1 was stimulated with a cathodic mono-phasic pulse (amplitude = 1 V, duration = 1 ms). Distance between two consecutive nodes is equal to 1 mm.

Table 5.1 shows that cathodic stimulation (indicated by a minus sign) requires in general less amplitude compared to the anodic stimulation for N1 and N2 (cathodic mono-phasic pulse requires -34% and -50% amplitude than the anodic mono-phasic for N1 and N2, respectively) with higher difference between anodic and cathodic fro N2 compared to N1. The anodic mono-phasic pulse is the pulse requiring the least amplitude for N4. Stimulation was most effective using cathodic pulses than anodic pulses for N1 and N2 while the inverse is true for N4. This is explained by the spatial gradient of the E-field for N2 and N4 (for N2, the E field is reaching higher maximum positive gradient for cathodic while the inverse is true for N4). As discussed in section 5.3, N1 will have the excitation according to the bend-mode. The maximum E-field for N1 occur for the anodic configuration (35 V/m) which is less than the maximum value of 77 V/m for the cathodic stimulation (Figure 5.9).

Concerning the most effective stimulation pattern, the bi-phasic pulses tend to require less amplitude to activate the nerves/axons compared to the mono-phasic pulses. This can be explained by the fact that the bi-phasic pulses combine anodic and cathodic mono-phasic pulses, thus there is an additional chance for stimulation at the phase reversal, especially with pulse durations longer than 0.5 ms. Results of Table 5.1 show also that the stimulation thresholds for the bi-phasic pulses are almost equal to the lowest threshold of the anodic and the cathodic mono-phasic pulses for each nerve/axon [35].

N4 requires the least amplitude for the stimulation among all the nerves, which

is explained by the highest value of the maximum positive value of the 1^{st} derivative of E-field for the anodic stimulation (maximum 1st derivative of E-field for N4 is 5 times higher than those of N1 and N2 in Figure 5.9) and also due to its branches being at the location with higher electric fields values compared to the other nerves branches (Figure 5.8).

Nerve/Axons	Pulse type	Threshold amplitude (V)	Δ_T in %
N1	Mono-phasic+	0.77	-
	Bi-phasic+	0.49	-36
	Mono-phasic-	0.51	-34
	Bi-phasic-	0.5	-35
N2	Mono-phasic+	0.88	-
	Bi-phasic+	0.41	-53
	Mono-phasic-	0.44	-50
	Bi-phasic-	0.42	-52
A3	Mono-phasic+	14	-
	Bi-phasic+	6.02	-57
	Mono-phasic-	6.02	-57
	Bi-phasic-	6.16	-56
N4	Mono-phasic+	0.22	-
	Bi-phasic+	0.22	0
	Mono-phasic-	0.26	18
	Bi-phasic-	0.21	-4
A5	Mono-phasic+	3.5	-
	Bi-phasic+	3.78	8
	Mono-phasic-	4.2	20
	Bi-phasic-	3.43	-2

Table 5.1: Stimulation thresholds for each configuration and each nerve/axon.
+ refers to the anodic pulse, while - refers to the cathodic pulse. Δ_T is the percentage of the stimulation thresholds related to the anodic mono-phasic voltage of each nerve/axon.

5.5 Stimulation of the Axon Population

5.5.1 Map of Percentage of Stimulated Axons

Figure 5.5d shows an example of axon activation of N1 generated by an anodic mono-phasic pulse (amplitude = 1 V, period = 1 ms), activating 70% of the axons for the anodic mono-phasic pulse. Stimulation with a bi-phasic pulse (amplitude = 1 V, period = 1 ms) results in a 100% axon activation in N1. Results also show that a 9% higher amplitude is required for the anodic mono-phasic pulse to obtain 100% axon population activation of N1 than for the bi-phasic pulse.

The axon population of N4 was 100% activated for both stimulating pulses. 95% and 100% axons of N2 were activated when stimulated by the anodic mono-phasic and the anodic bi-phasic pulses, respectively. Results also show that 2% more amplitude is needed for the anodic mono-phasic pulse to obtain 100% axon population activation of N2.

The axon population of N1 needs slightly higher amplitudes to be 100% activated due to the high sensitivity of the percentage of stimulated axons to the electrode position, which will be detailed in the Section 5.5.3.

5.5.2 Effect of the Electrodes Depth

Figure 5.11 shows the percentage of the activated axons and the value needed to obtain 100% activation for axon population in N1, N2, and N4 as a function of the electrode depth (d) from 1.5 mm to 0.8 mm for anodic mono-phasic and bi-phasic pulses. The voltage for each nerve is related to the value at 1.5 mm (initial depth of the electrode) for each nerve.

The axon population of N4 is the most activated among the three sets of nerves and the bi-phasic pulses require less amplitude to activate the axon population. These observations are in coherence with results for single axons.

The axon population of N1 is the most sensitive to the electrode depth (maximum sensitivity of 9.8% per 0.1 mm for the 0.8 mm depth in Figure 5.11). We note that 9.8 % in the percentage of axons corresponds approximately to 2 axons out of 20 axons in each population. Results also show that 0% axon activation is obtained for depths less than 1 mm for all the nerves and all the pulses.

No axon activation is registered for needle depths less than 1 mm for all the pulses and nerves (Figure 5.11). This is due to the weak inner electric field, in case that the needle does not penetrate the ear to a sufficient extent. This shows the importance of the electrode penetration depth for nerve/axon activation. At least 1 mm penetration depth should be kept to ensure complete nerve activation with a value of 1.6 V pulse amplitude.

5.5.3 Effect of the Electrodes Position

Figure 5.12 shows the percentage of the activated axons and the value needed to obtain 100% activation for the axon population of N1 as a function of the electrode1 displacement with 1 mm in the y and z directions (y, z), as shown in Figure 5.7 for some displacements.

The percentage of activated axons is sensitive to the position of the electrode with a maximum sensitivity of 15.5% for each 0.1 mm (positions: (-0.1, 0.1) and (0.1, 0.1)). We note that 15.5 % in the percentage of axons corresponds approximately to 3 axons out of 20 axons in each axon population. Some electrode positions ((-0.1, -0.1), (0, -0.1), and (0.1,-0.1), Figure 5.7) provide a higher percentage

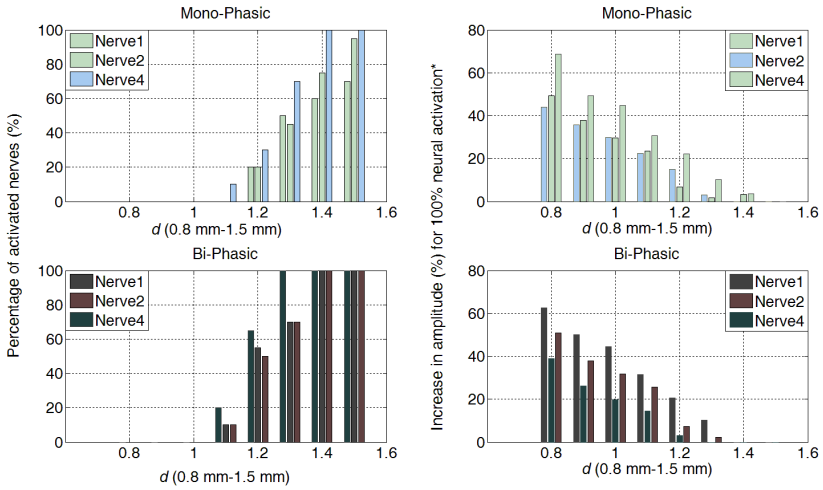

Figure 5.11: Percentage of activated axons of N1, N2, and N4 and increase in the amplitude needed to activate 100% of the axon population around each nerve, related to the value needed for 100% axon activation for the 1.5 mm depth position for different electrode depths (d). * Related to the value needed for 100% axon activation for the 1.5 mm depth position.

of activated axons than the original position, which can be used to further decrease the pulse amplitude (Figure 5.12). At these positions, the electrode needles are slightly closer to the axon population, exposing the axons to higher values of the electric field. Stimulation thresholds and the percentage of activated axons are sensitive to the electrodes' position.

5.6 Conclusions

A realistic numerical model for pVNS application at the human auricle including vessels and nerves was developed. The numerical model was used to investigate the percentage of the activated axons with respect to stimulation waveform, electrode depth, and electrode position. Results show that a cathodic bi-phasic pulse, besides being charge balanced, is the pulse requiring the least amplitude to activate the nerves. The feasibility and plausibility of the given model and tools are demonstrated. However, the robustness of the model has to be checked in the next chapters using sensitivity analysis of different model parameters as well as experimental validation of the numerical approach (next chapter 6).

The simulations provide an impression in the field distribution and thus stress the necessary accuracy while placing electrodes. The model explains physiological findings in regions known to be innervated by more than one nerve. Furthermore,

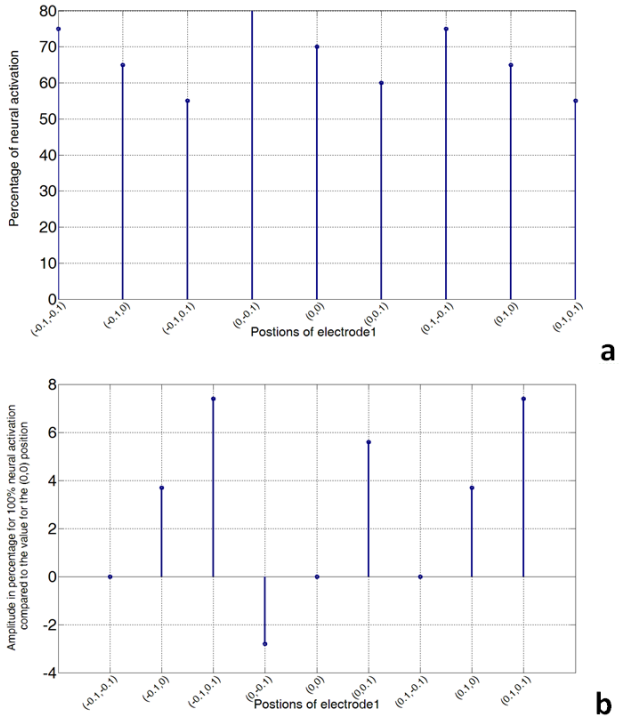

Figure 5.12: Percentage of axon activation and the amplitude needed for 100% axon activation for different positions of electrode1. These values are for axons of N1 stimulated by the anodic mono-phasic pulse.

the model allows personalization of stimulation when supported by experimental and clinical data. As the physiology of each patient is different to a degree, a typical distribution of the nerves and vessels was selected. Electrode-interface effects were not modelled in this study and we used constant voltage simulation. Nevertheless, it is possible to gain useful information for the necessity of accuracy when placing electrodes by evaluating simple nerve structures. In the next chapters, further evaluation of the model will be assessed to investigate additional stimulation patterns (tri-phasic pulses, pulses with equal energy) and burst stimulation as well as the robustness of the model. Experimental pVNS validation of the set-ups from numerical modelling and mutual optimization of the model and the experimental setup will also be performed using clinical studies.

References

[1] D Groves and V Brown. *Vagal nerve stimulation: a review of its applications and potential mechanisms that mediate its clinical effects*. Neuroscience and Biobehavioral Reviews, 29(3):493 – 500, 2005.

[2] A Zamotrinsky, B Kondratiev, and J de Jong. *Vagal neurostimulation in patients with coronary artery disease*. Autonomic Neuroscience, 88(1-2):109–116, 2001.

[3] G De Ferrari, H Crijns, and M Borggrefe et al. *Chronic vagus nerve stimulation: a new and promising therapeutic approach for chronic heart failure*. European Heart Journal, 32(7):847–855, 2011.

[4] J Ellrich. *Transcutaneous Vagus Nerve Stimulation*. European Neurological Review, 6(4):254, 2011.

[5] S Kampusch, E Kaniusas, and J Szeles. *New Approaches in Multi-Punctual Percutaneous Stimulation of the Auricular Vagus Nerve*. Proceedings of the 6th International IEEE EMBS Conference on Neural Engineering, pages 263–266, 2013.

[6] E Peuker and T Filler. *The nerve supply of the human auricle*. Clin. Anat., 15(1):35–37, 2002.

[7] E Kaniusas, G Varoneckas, B Mahr, and J Szeles. *Optic Visualization of Auricular Nerves and Blood Vessels: Optimisation and Validation*. IEEE Transactions on Instrumentation and Measurement, 60(10):3253–3258, 2011.

[8] S Sator-Katzenschlager, J Szeles, G Scharbert, A Michalek-Sauberer, A Kober, G Heinze, and S Kozek-Langenecker. *Electrical Stimulation of Auricular Acupuncture Points Is More Effective Than Conventional Manual Auricular Acupuncture in Chronic Cervical Pain: A Pilot Study*. Anesthesia and Analgesia, pages 1469–1473, 2003.

[9] T Payrits et al. *Vagal stimulation - a new possibility for conservative treatment of peripheral arterial occlusion disease.* Zentralblatt fÃijr Chirurgie, 136:431–435, 2011.

[10] H Berthoud and W Neuhuber. *Functional and chemical anatomy of the afferent vagal system*. Autonomic Neuroscience, 85(1-3):1–17, 2000.

[11] E Kaniusas. *Biomedical Signals and Sensors I.* Published by Springer, 2012.

[12] J Szeles and G Litscher. *Objectivation of cerebral effects with a new continuous electrical auricular stimulation technique for pain management*. Neurological Research, 26(7):797–800, 2004.

[13] K Tracey. *Reflex control of immunity*. Nature Reviews Immunology, 9(6):418–428, 2009.

[14] Y Zhao, W He, X Jing, J Liu, P Rong, and H Ben et al. *Transcutaneous Auricular Vagus Nerve Stimulation Protects Endotoxemic Rat from Lipopolysaccharide-Induced Inflammation*. Evidence-Based Complementary And Alternative Medicine, pages 1–10, 2012.

[15] X Gao, S Zhang, B Zhu, and H Zhang. *Investigation of specificity of auricular acupuncture points in regulation of autonomic function in anesthetized rats*. Autonomic Neuroscience, 138(1-2):50–56, 2008.

[16] S Miocinovic. *Computational Analysis of Subthalamic Nucleus and Lenticular Fasciculus Activation During Therapeutic Deep Brain Stimulation*. Journal Of Neurophysiology, 96(3):1569–1580, 2006.

[17] C Schmidt and U Van Rienen. *Modeling the Field Distribution in Deep Brain Stimulation: The Influence of Anisotropy of Brain Tissue*. IEEE Transactions On Biomedical Engineering, 59(6):1583–1592, 2012.

[18] S M Danner et al. *Potential distribution and nerve fiber responses in transcutaneous lumbosacral spinal cord stimulation. Int*. In Int. Conference on Advancements of Medicine and Health Care through Technology; IFBME 44, pages 203–208, 2014.

[19] A M Samoudi, G Vermeeren, E Tanghe, R Van Holen, L Martens, and W Josephs. *Numerically simulated exposure of children and adults to pulsed gradient fields in MRI*. J. Magn. Reson. Imaging, 44:1360–1367, 2016.

[20] M De Lucia, K Embleton G Parker, J Newton, and V Walsh. *Diffusion tensor MRI-based estimation of the influence of brain tissue anisotropy on the effects of transcranial magnetic stimulation*. Neuroimage, 36(4):1159–1170, 2007.

[21] M Lu and S Ueno. *Calculating the induced electromagnetic fields in real human head by deep transcranial magnetic stimulation*. In Conf. Proc. IEEE Eng. Med. Biol. Soc, pages 795–798. 2013.

[22] C Choi, Y Lee, and Y Tsou. *Modeling Deep Brain Stimulation Based on Current Steering Scheme*. IEEE Transactions on Magnetics, 47(5):890–893, 2011.

[23] A Chaturvedi, T Foutz, and C McIntyre. *Current steering to activate targeted neural pathways during deep brain stimulation of the subthalamic region*. Brain Stimulation, 5(3):369–377, 2012.

[24] M S Evans, S Verma-Ahuja, D K Naritku, and J A Espinosa. *Intraoperative human vagus nerve compound action potentials*. Acta Neurol Scand, 110:232–238, 2004.

[25] D McNeal. *Analysis of a Model for Excitation of Myelinated Nerve*. IEEE Transactions on Biomedical Engineering, BME-23(4):329–337, 1976.

[26] J Reilly and W Larkin. *Understanding transient electric shock*. Johns Hopkins APL Tech. Digest, 5(3):296–304, 1984.

[27] B Frankenhaeuser and AF Huxley. *A quantitative description of membrane currents and its application to conduction and excitation in nerve*. 1. Physiol, 117:500–544, 1952.

[28] Sim4Life Zurich Med Tech. *www.zurichmedtech.com/sim4life/*. 2016.

[29] E Neufeld, A Cassara, H Montanaro, N Kuster, and W Kainz. *Functionalized anatomical models for EM-neuron Interaction modeling*. Physics in Medicine and Biology, 61(12):4390–4401, 2016.

[30] E Neufeld, I Vogiatzis, M Ida Iacono, L Angelone, W Kainz, and N Kuster. *Investigation of assumptions underlying current safety guidelines on EM-induced nerve stimulation*. Physics in Medicine and Biology, 61(12):4466–4478, 2016.

[31] J Reilly, V Freeman, and W Larkin. *Sensory Effects of Transient Electrical Stimulation - Evaluation with a Neuroelectric Model*. IEEE Transactions on Biomedical Engineering, BME-32(12):1001–1011, 1985.

[32] V Santis, X Chen, I Laakso, and A Hirata. *An equivalent skin conductivity model for low-frequency magnetic field dosimetry*. Biomedical Physics and Engineering Express, 1:1, 2015.

[33] F Tilotta, B Lazaroo, M Laujac, and J Gaudy. *A study of the vascularization of the auricle by dissection and diaphanization*. Surgical and Radiologic Anatomy, 31(4):259–265, 2009.

[34] L Alvord and B Farmer. *Anatomy and orientation of the human external ear*. J. Am. Acad. Audiol, 8(6):383–90, 1997.

[35] J Reilly and A Diamant. *Electrostimulation-Theory Applications and and Computational Model*. Artech House, 2011.

[36] S Safi, J Ellrich, and W Neuhuber. *Myelinated Axons in the Auricular Branch of the Human Vagus Nerve*. Anat. Rec, 299(9):1184–1191, 2016.

[37] J Sandby-Moller, T Poulsen, and H Wulf. *Epidermal Thickness at Different Body Sites: Relationship to Age and Gender and Pigmentation and Blood Content and Skin Type and Smoking Habits*. Acta Dermato-Venereologica, 83(6):410–413, 2003.

6

Sensitivity Assessment of the pVNS Numerical Model

6.1 Introduction

In the Chapter 5, a realistic numerical model for pVNS application at the human auricle including vessels and nerves was developed. The percentage of the activated axons with respect to stimulation waveform, electrode depth, and electrode position was investigated. Results show that a cathodic bi-phasic pulse was the pulse requiring the smallest amplitude to activate the nerves. Chapter 5 provided a better understanding of the electric potential and current distribution in tissues surrounding the stimulation electrode. Quantitative sensitivity of the stimulation thresholds and percentage of activated axons to the electrodes' depth and position was also investigated and reported. The feasibility and plausibility of the given model and tools was demonstrated. However, a shortcoming of current clinical applications of ABVN stimulation is the mostly empirical selection of both stimulation regions in the ear and stimulation patterns with mostly unknown variation of therapeutic/physiologic effects, which may lead to over-stimulation with unfavorable recruitment of pain-related Aδ fibers or under-stimulation. Omnipresent inter-patient variability is neglected, while safety margins when stimulating different fibers are missing.

High sensitivity and specificity of stimulation is then of huge importance due to the dense innervation of the auricle with various nerves [1]. By stimulation of different nerves, opposite physiological reactions and an even adverse therapeutic

outcome may be elicited. Thus, a sensitivity analysis of the numerical model is an invaluable tool to better quantify the dependence of the numerical model developed in Chapter 5 to different parameters. Sensitivity analysis is used to link the uncertainty in the model output to different sources of uncertainty in the model parameters [2–5]. It is also used to identify the most contributing input parameter and ascertain interaction effects within the model. Thus, we can achieve a better model verification and understanding, factor prioritization, and model simplification.

The objective of this chapter is to perform a sensitivity analysis of a numerical model for pVNS. This chapter is structured as follows: we start by specification of the input parameters range of values. Then we investigate effects of the axon fiber diameter, number of axons, model temperature, ear conductivity, as well as electrodes' penetration depth and position on the stimulation thresholds for single and bundled axons. The final goal is to identify and prioritize the most influential parameters, identify non-influential parameters in order to fix them to nominal values, and map the output behavior as a function of the parameters by limiting the input range values to a specific domain if necessary. In Section 6.2 the simulation platform, overview of the updated numerical model, the methodology for sensitivity analysis and range values for the input parameters are described and provided. In section 6.3 we start by describing the electric fields distribution in the ear with comparison between electric fields values at the different nerves locations, then we present results of the effect of the fiber diameter, SENN model temperature, and the tissue conductivity on the stimulation thresholds for single nerves. In Section 6.4, the stimulation thresholds to obtain 100 % axon activation are presented for the axon population with discussion of the effect of the fiber diameter, axon number, SENN model temperature, as well as the electrodes' depth and position on the amplitudes for 100% activation of the axon populations. Finally, conclusions are drawn in Section 6.6.

6.2 Materials and Methods

6.2.1 Numerical Model

We used the Sim4Life platform [6] to conduct the numerical simulations. Electromagnetic simulations were performed using the low frequency solver. Neuronal simulations were performed using the neuronal tissue models from Sim4Life. Time-response of the axonal membrane potential to external injected currents was simulated using the spatially extended nonlinear node (SENN) [7, 8] model. The threshold amplitude of a pulse to depolarize the axons was calculated using the titration mechanism. Details of the simulation platform can be found in Chapter 5, Section 5.2.

Figure 6.1 shows an overview of the updated numerical model. We used a realistic high resolution model of a human ear (spatial resolution 3 mm), 3 electrodes (E1, E2, and reference electrode E3), and a spatial model of major blood vessels and nerves. The conductivity of the vessels and ear was set to 0.7 S/m and 0.2 S/m, respectively. Shapes and locations of the nerves (N) are shown in Figures 6.1b and 6.1c based on an exemplary nerve supply and vascularization of the human auricle [1, 9, 10]. Stimulation was performed with a single mono-phasic voltage pulse (amplitude = 1 V, anodic pulse, duration 1 ms) and bi-phasic voltage pulse (amplitude = $\pm$ 1 V, anodic phase precedes cathodic phase, total pulse duration = 1 ms), as in Chapter 5. A number of axons was defined from a rectangular seed region close to stimulation electrodes to generate an axon population composing nerves, based on the axon count used for the sensitivity analysis. According to [11] a space equal to the diameter of a single axon is modelled between two adjacent axons to simulate a dense axon population.

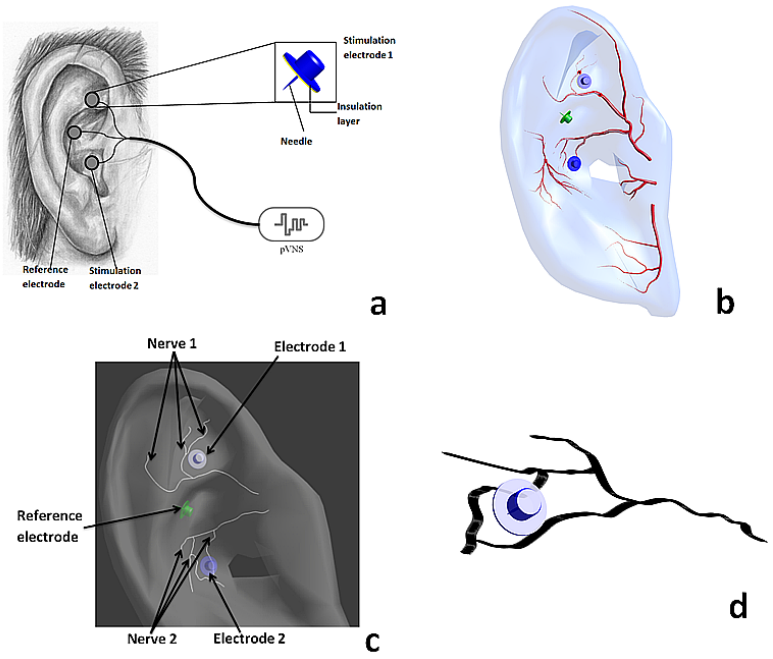

Figure 6.1: Numerical model of the pVNS application. (a) Scheme of the application. (b) Auricle, vessels, nerves, and the electrodes. Vessels and nerves are inside the ear and not on the surface of the ear. (c) Locations and shapes of the nerves. (d) Detail of the axon population N2 and Electrode 2.

6.2.2 Sensitivity Assessment of the Numerical Model

Sensitivity analysis of the numerical model parameters is critical to the model robustness and validity. It also serves to guide future research on the most influential of these factors. The method used to assess the sensitivity of the numerical model to parameters' fluctuation and uncertainty, is to repeatedly change one parameter at a time while keeping the others fixed (at an average value). We increase the parameter by a given step and we observe the change in the model output, which is the stimulation threshold for single axons and the stimulation threshold for 100% recruitment volume for the whole axon population [3]. A sensitivity index (SI) is calculated (as absolute percentage value) for each parameter as follows:

$$SI_{parameter} = 100\,\frac{O_{max} - O_{min}}{O_{max}} \tag{6.1}$$

Where O_{min} and O_{max} are minimum and maximum output values, respectively, resulting from changing the respective input over its selected range. The output values are defined as the stimulation threshold for single axons and the stimulation threshold for a 100% activation of an axon population. The largest SI values correspond to a high degree of sensitivity of the output values to the given input. This figure of merit represents a good quantification of parameter model and variability [3].

Two more quantifications were used for the variation of the stimulation thresholds to achieve 100% axon activation: relative variation of the stimulation thresholds compared to an average value (Δ_B) and relative variation between the thresholds of two adjacent inputs (Δ) adjusted to the difference between the input values.

$$\Delta_B = 100\,\frac{O_j - O_B}{O_B\,(i_j - i_B)} \tag{6.2}$$

$$\Delta = 100\,\frac{O_j - O_{j+1}}{O_j\,(i_j - i_{j+1})} \tag{6.3}$$

Where O_B, O_j and O_{j+1} are the stimulation thresholds to achieve 100% axon activation for the average (i_B), the j^{th} (i_j) and $(j+1)^{th}$ (i_{j+1}) input value, respectively. These two quantities show the variation in the stimulation threshold compared to a reference value and between thresholds of two consecutive inputs. The investigated parameters include: axon fiber diameter, number of axons, SENN model temperature, ear conductivity, as well as electrodes' penetration depth and position. For each of these parameters, a range of values was determined from literature:

- Table 6.1 shows the number of myelinated axons with diameter $\geq$ 7 μm of the auricular vagus nerve branch in the left and the right ear [12]. The ABVN axons are Aβ axons, and thus have diameters from 7 μm upwards [12].

These values were calculated using 16 bodies: 5 females, 11 males, range 50-96 years, and median age 73 years.

- Table 6.2 shows the average number of myelinated axons in the left and right ABVN for different axons with a diameter higher than 7 μm [12]. For each defined axon diameter and number of axons, a rectangular seed region of the axon population is defined with a calculated size of the seed region. Chaturvedi et al. [11] left approximately a diameter of an axon between each two axons to simulate a dense population in the brain. We used the same approach to generate a dense population around each of the two electrodes for each number of axons with a defined axon diameter.

- Model temperature was changed based on recent clinical investigation of the variation in normal ear temperature. Ear temperature was measured in 2006 individuals (38.3% males) [13]: 683 children 2-4 years, 492 adolescents 10-18 years, 685 adults 19-65 years, and 146 elderly 66-89 years. Mean temperature was 36.5 $\pm$1 0.5°C in adolescents, 36.1 $\pm$1 0.5°C in elderly, 36.3 $\pm$1 0.6°C in men, and 36.5 $\pm$1 0.5°C in women [13].

- The ear conductivity was changed from 0.1 S/m to 0.7 S/m [14].

- The needle penetration depth of E1 and E2 inside the ear was changed from 1.5 to 0.8 mm in steps of 0.1 mm [15].

- The lateral position of the electrodes (E1 and E2) was also changed from the original position by $\pm$0.1 mm in the y and z directions, with a maximum of ($\pm$0.1, $\pm$0.1) mm [15].

Table 6.3 summarizes the range, average (AV), and step of incrementing for each parameter.

Axon Count	
Left ABVN	Right ABVN
133	102
44	55
32	108
81	58
89	110
64	65
29	107
46	23
59	21

Table 6.1: Number of myelinated axons $\geq 7\mu m$ in diameter of the left and right auricular branch of the vagus nerve (ABVN), taken from [12].

Axon diameter (µm)	Axon Count	
	Left ABVN	Right ABVN
7	14.25	20
7.5	11.5	13
8	10.75	11.5
8.5	8	7
9	4	6.25
9.5	3.25	3.25
10	4	3.5
10.5	2	2.5
11	1.5	1.25
11.5	1	1
12	1	1

Table 6.2: Number of myelinated axons in the left and right auricular branch of the vagus nerve (ABVN) for axon diameters $\geq 7\mu m$, extracted from [12].

6.3 Sensitivity of the Stimulation Thresholds for Single Nerves

Table 6.4 summarizes the sensitivity indices for all investigated parameters. In the following sections, the electric field distribution in the ear will be investigated and the different sensitivity indices will be discussed and compared.

Parameter	Range	AV	Step	Reference
Number of axons	21-133	68	18	[13]
Axon fiber diameter (μm)	7-12	8	0.5	[13]
Model temperature (°C)	35.6-37	36.3	0.2	[14]
Ear conductivity (S/m)	0.1-0.7	0.4	0.1	[15]
Electrode penetration depth (mm)	0.8-1.5	*	0.1	[12]
Electrode position (mm)	(0.1, 0.1)	0	0.1	[12]

Table 6.3: Range, average (AV), and the incrementation step for each parameter used in the sensitivity analysis

Parameter	SI (%)
Diameter of axon (N1, single axon)	13
Diameter of axon (N2, single axon)	17
Temperature (N1, single axon)	0.9
Temperature (N2, single axon)	0.7
Ear conductivity (single axons)	0.1
Diameter (nerve population, mono-phasic)	14
Diameter (nerve population, bi-phasic)	13
Number of axons	18
Temperature (nerve population)	0.7
Electrode penetration depth (nerve population)	22.3
Electrode position (nerve population)	6.5

Table 6.4: Sensitivity index (SI) for the respective input parameters.

6.3.1 Electric Field Distribution

Figure 6.2 shows the electric field distribution. The E-field is directed from the anodic electrodes (E1 and E2 at 1 V) to the reference electrode (E3 at 0 V). Vessels and nerves near E2 are more exposed to the electric fields than those in the E1 region. Maximum field values occur near the electrodes (89 V/m near E1 and 98 V/m near E2), and are penetrating inside the ear, vessels and nerves. N2 branches are in locations with higher electric field values compared to branches of N1.

6.3.2 Effect of the Fiber Diameter

Figure 6.3 shows the effect of the fiber diameter on the stimulation thresholds for N1 and N2. The axon fiber diameter was changed from 7 μm to 12 μm in steps of 0.5 μm. Results show that the stimulation thresholds decrease with increasing fiber diameter. Bi-phasic pulses require slightly less amplitude to stimulate the

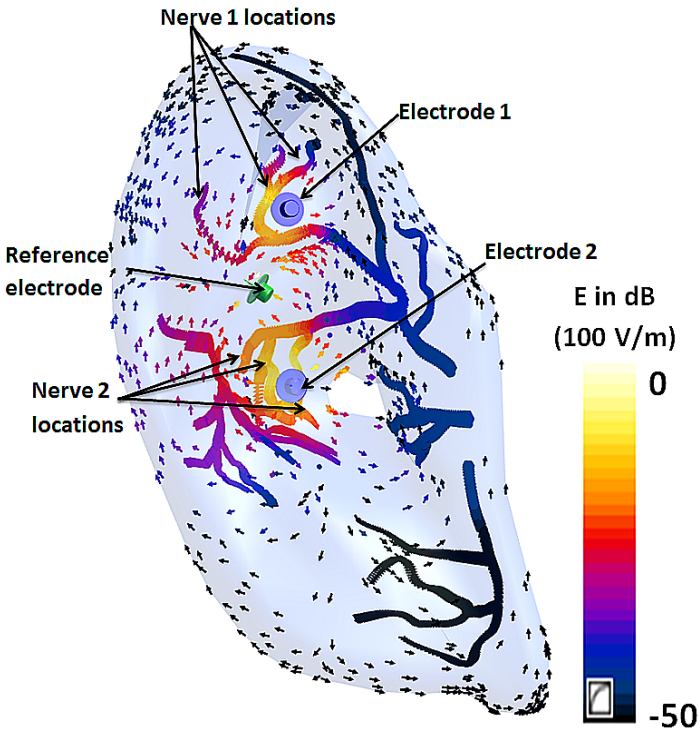

Figure 6.2: Electric field distribution, in dB normalized to 100 V/m. Electrodes 1 and 2 at 1 V, reference electrode at 0 V. Electrodes completely inside the ear (electrode penetration depth 1.5 mm).

nerves than the mono-phasic pulses (0.24%-0.88% and 0.28%-2.54% less for bi-phasic for N1 and N2, respectively). N2 is stimulated with lower amplitudes than N1 for the two types of pulses (with a fiber diameter of 8 μm for example, the stimulation thresholds are: 0.89 V and 0.88 V for N1 and 0.82 V and 0.80 V for N2). The sensitivity index for this parameter and for each configuration is in average equal to: $SI_{d,axon1} = 13\ \%$ and $SI_{d,axon2} = 17\ \%$ for N1 and N2, respectively. N2 is more sensitive to the axon fiber diameter.

6.3.3 Effect of the Model Temperature

Figure 6.4 shows the effect of the temperature on the stimulation thresholds for N1 and N2. The SENN model temperature was changed from 35.6 ° C to 37 ° C in steps of 0.2 ° C. Simulations were performed using the axon diameter of 8 μm. Results show only small impact of the temperature on the stimulation threshold for this range of values (0.9% and 0.7% change over the entire temperature range for N1 and N2, respectively). Changes in stimulation thresholds occurred only for

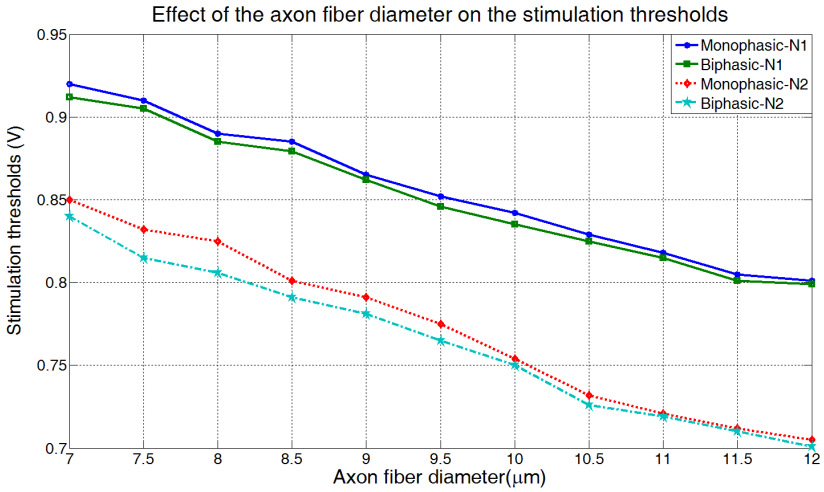

Figure 6.3: Effect of the axon fiber diameter on the stimulation thresholds for N1 and N2.

35.6 ° C (0.7%) and 37 ° C (0.4 %) for N2. Stimulation thresholds were more irregular over the temperature range for N1 than N2 (3 changes in the stimulation thresholds for N1 compared to one change for N2). The sensitivity index for this parameter for each configuration is equal to: $SI_{T,axon1} = 0.9\,\%$ and $SI_{T,axon2} = 0.7\,\%$ for N1 and N2, respectively.

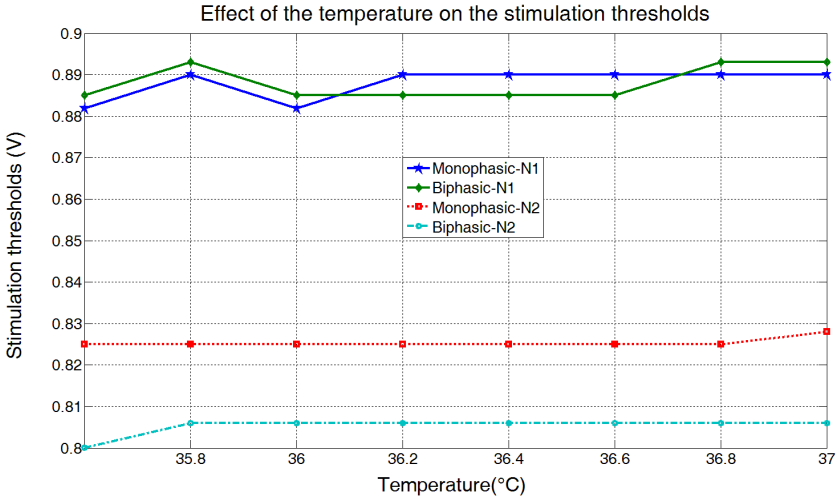

Figure 6.4: Effect of the temperature on the stimulation thresholds for N1 and N2.

6.3.4 Effect of the Tissue Conductivity

Figure 6.5 shows the effect of the ear conductivity on the stimulation thresholds. Only a very small change in the stimulation thresholds occurred (0.11% over the entire range 0.1-0.7 S/m). The sensitivity index for this parameter is equal to: $SI_{conductivty} = 0.1\ \%$ for mono-phasic and bi-phasic configurations. Lower values (not shown here) was found for the effect of the vessels conductivity on the stimulation thresholds.

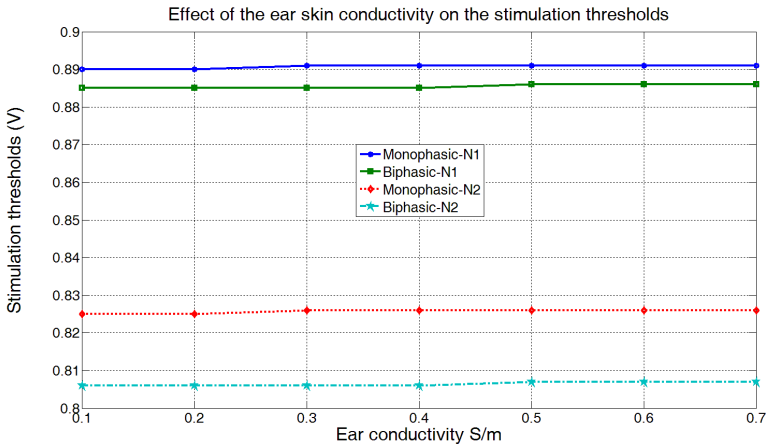

Figure 6.5: Effect of the ear conductivity on the stimulation thresholds for N1 and N2.

6.4 Sensitivity of the Percentage of Stimulated Axons

6.4.1 Effect of the Fiber Diameter

Figure 6.6 shows the amplitudes needed to obtain 100% activation for an axon population in N2 as a function of the axon fiber diameter from 7 µm to 12 µm in steps of 0.5 mm. Δ_B and Δ refer to the relative variation compared to the average value (8 µm) and between two adjacent diameters, respectively. The figure shows decreasing stimulation thresholds as a function of the axon fiber diameter for mono-phasic and bi-phasic pulses. Maximum deviation from the average value and between two adjacent diameters (5.88%) was obtained for the fiber diameter of 8.5 µm. Δ is equal to zero for the last input value (no consecutive value to compare with) The sensitivity index for this parameter is equal to: $SI_{d,population1} = 14\ \%$ and $SI_{d,population2} = 13\ \%$ for mono-phasic and bi-phasic configurations, respectively.

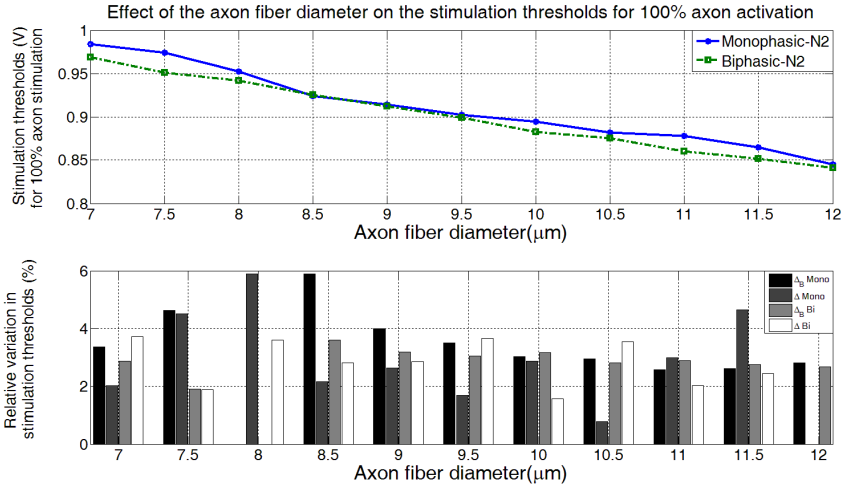

Figure 6.6: Effect of the axon fiber diameter on the stimulation thresholds for the axon population around N2. Δ_B and Δ refer to the relative variation compared to the average value (8 µm) and between two adjacent diameters, respectively.

6.4.2 Effect of the Axons Number

Figure 6.7 shows the amplitudes for 100% activation of the axon population in N2 as a function of the axon number from 21 to 133 in steps of 18 (half the standard deviation of the axons number range). Δ_B and Δ refer to the relative variation com-

pared to the average value (68 axons) and between two adjacent numbers, respectively. The stimulation thresholds increase as a function of the number of axons. Mono-phasic pulses require slightly higher amplitudes than bi-phasic pulses (1%-1.94% less for bi-phasic pulses). Maximum deviation from the average value (68 axons) and between two adjacent diameters was obtained for 57 axons (0.27 %). The sensitivity index for this parameter is equal to: $SI_{number,population} = 18\ \%$ for mono-phasic and bi-phasic configurations.

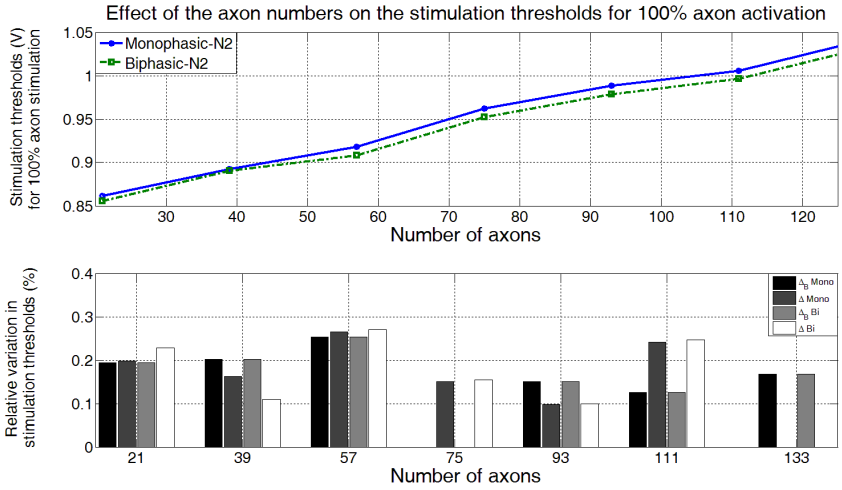

Figure 6.7: Effect of the axon numbers on the stimulation thresholds for the axon population around N2. Δ_B and Δ refer to the relative variation compared to the average value (68) and between two adjacent diameters, respectively.

6.4.3 Effect of the Model Temperature

Figure 6.8 shows the effect of the temperature on the stimulation thresholds for the axon population in N2. Temperature was changed from 35.6 ° C to 37 ° C in steps of 0.2 ° C. We used 68 axons with a diameter of 8 µm. As seen in the results for single axons, the effect of temperature is less significant than the axon diameters' effect (SI of 14% and 0.7% for axon diameter and temperature, respectively). The threshold was almost stable in the whole range except for the change at 35.8 ° C and 36 ° C. The sensitivity index for this parameter is equal to: $SI_{T,population} = 0.7\ \%$ for both mono-phasic and bi-phasic configurations.

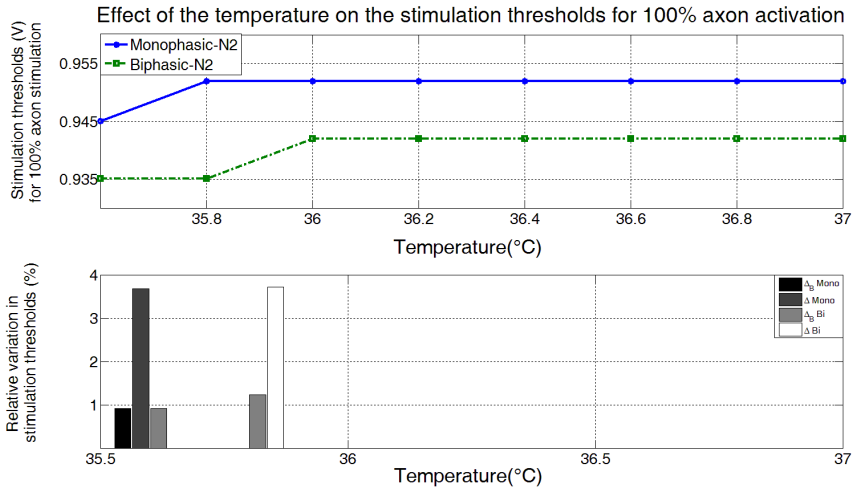

Figure 6.8: Effect of the temperature on the stimulation thresholds for the axon population around N2. Δ_B and Δ refer to the relative variation compared to the average value (36.3 ° C) and between two adjacent diameters, respectively.

6.4.4 Effect of the Electrodes' Penetration Depth

Figure 6.9 shows the effect of the electrodes' depth on the stimulation thresholds for the axon population in N1 and N2. Simulations were performed using anodic and cathodic mon-phasic pulses. E1 and E2 penetration depth were changed from 1.5 mm to 0.8 mm inside the ear with a step of 0.1 mm. Anodic stimulations require higher amplitudes than cathodic stimulations (ratio of stimulation threshold for anodic to cathodic (P) is between 1.3 and 1.4 for N1 and N2, Figure 6.9). The sensitivity index for the E1's depth is equal to 20.1% and 21.5% for anodic and cathodic stimulation, respectively. For the E2's depth, the sensitivity index is equal to 24% and 23.8% for anodic and cathodic stimulation, respectively. This yields to an average value for the sensitivity index of the electrodes' depth of $SI_{depth,population} = 22.3\ \%$.

6.4.5 Effect of the Electrodes' Position

Figure 6.10 shows the stimulation thresholds for 100% axon activation for N1 and N2 as a function of the electrodes' position with $\pm$ 0.1 mm displacements. For each electrode, some positions provide lower stimulation thresholds than the original position (positions (0.1, 0.1), (0, 0.1) and (0.1, 0) for E1. Positions (0, -0.1), (-0.1, 0) and (-0.1, -0.1) for E2). The sensitivity index for the E1's position is equal to 4.7% and 7.3% for anodic and cathodic stimulation, respectively. For the E2's

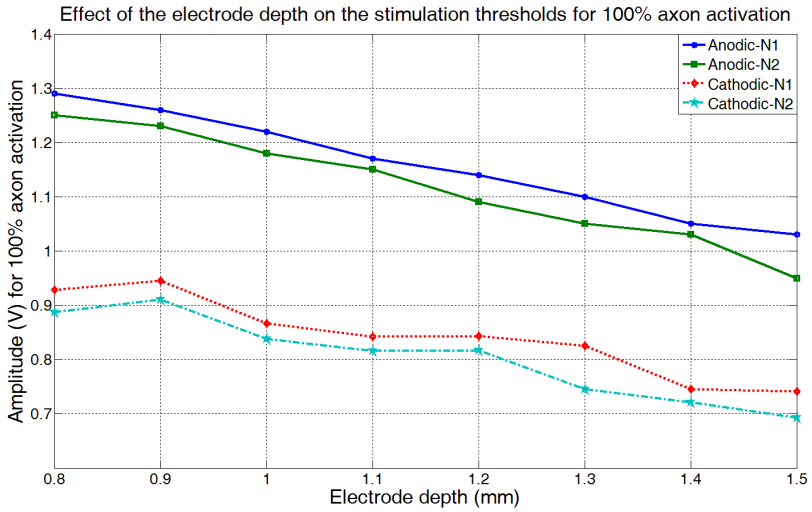

Figure 6.9: Effect of the electrodes' penetration depth on the stimulation thresholds for 100% axon activation using anodic and cathodic mono-phasic pulses.

position, the sensitivity index is equal to 6.1% and 7.9% for anodic and cathodic stimulation, respectively. This yields to an average value for the sensitivity index of the electrodes' position of $SI_{position,population} = 6.5\ \%$.

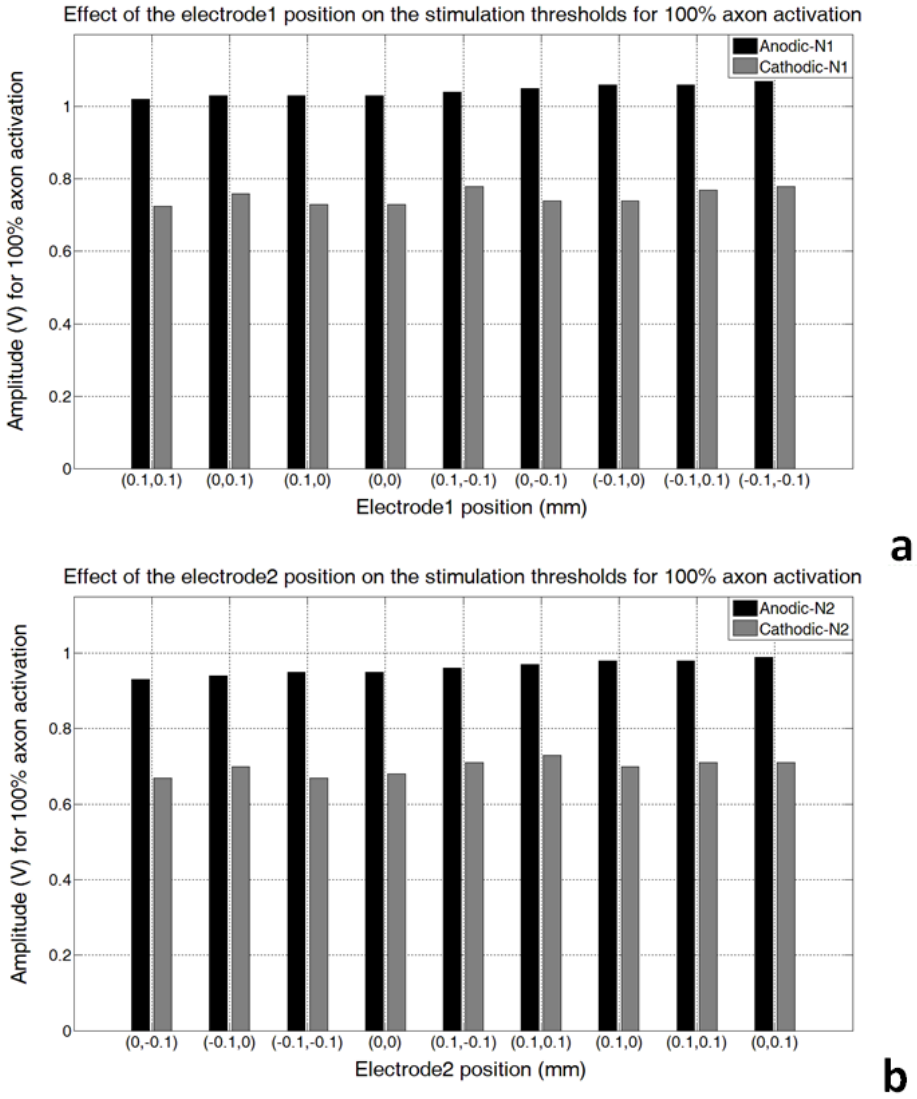

Figure 6.10: Effect of the electrodes' position on the stimulation thresholds for 100% axon activation using anodic and cathodic mon-phasic pulses.

6.5 Discussion

The temperature and ear conductivity are the non-influential parameters in the specified range of values. Maximum change in the stimulation threshold is equal to 8 mV (0.9 %) and 1 mV (0.1 %) over the entire range for the temperature and ear conductivity, respectively. The electrodes' position is a more influential parameter with an SI equal to 6.5% over the entire range and less than 7 mV for 0.1 mm shift in the electrodes' position. The number of axons seems to be more influential parameter than the axon diameter (18% is the maximum change in the stimulation threshold for 100% axon activation over the entire range). However, this parameter has a wider range of values than the axon diameter (number of axons is in the range 21-133 while the axon diameter is from 7 μm to 12 μm). If we adjust the SI with the range of values for each parameter, the axon number sensitivity will become 1.5 mV for each axon and 25.6 mV for each 1 μm diameter. The frequency distribution of the axon fiber diameters from 7-12 μm shows, that more than 60% of the ABVN axons have a diameter between 7 μm and 8 μm [12]. In this range, the maximum variation in the stimulation threshold for 100% axon activation is 32 mV for each 1 μm diameter. The electrodes' penetration depth is the most influential parameter with a maximum variation of 38 mV for each 0.1 mm penetration depth. Clinical data show that 38 mV is a rather small voltage change. Stimulations are typically applied with several 100 mV up to several V. In some cases steps of approximately 50 mV can be perceived by the patients.

In the following sections, the influence of different parameters on the stimulation thresholds will be discussed based on the results of Sections 6.3 and 6.4

6.5.1 Tissue Conductivity

In the range of interval between 0.1 S/m and 0.7 S/m, the ear conductivity has the lowest effect on the stimulation thresholds among all the parameters (change of 0.1% over the entire range of 0.1-0.7 S/m). In fact, as suggested by de Santis et al. [14], any value of the skin in the range 0.1-0.7 S/m will not considerably alter the E-fields. Works on the effect of skin conductivity in a low frequency exposure assessment for peripheral nerve tissue [16] show that the choice of skin conductivity affects the induced electric field, resulting in an increasing factor of three in the induced electric field when using a skin conductivity of 0.0002 S/m instead of 0.1 S/m. However, since the ratio of maximum to minimum values in [16] is two orders higher than in our study, we expect the induced electric field to change a way less in our study compared to [16]. The effect of skin conductivity on the induced electric field for peripheral nerve exposure was also investigated in Chapter 4 using a skin conductivity of 0.1 S/m and 0.2 S/m. Results of the study in [17] show maximum changes in the electric field of 4%. However, the values reported in [17] concern the maximum (99% value) induced electric field for an

adult model completely inside shielded whole-body x-, y-, and z-gradient coils. Furthermore, the ear conductivity is less likely to change a lot in the range of 0.1-0.7 S/m between individuals. Thus, dielectric properties of the ear have no effect on the stimulation thresholds and the axons' recruitment volume.

6.5.2 Fiber Diameter and Number

Results of Sections 6.3.2 and 6.4.1 show decreasing stimulation thresholds with increasing axon fiber diameter (a decrease of 17% over the entire range of 7-12 μm for N2). Examination of equations 1.7, 1.8 and 1.9 shows that the three components G_a, G_m, and C_m are proportional to fiber diameter d ($G_a \propto$ d since L $\propto$ d) [8]. Since G_a, G_m, and C_m occur only in the transmembrane voltage equation 1.12 as ratios, changes in axon fiber diameter affect the solution only through its relation to the internodal distance L. The only effect of the changing axon diameter is then in the calculation of the external potential at the nodes. The induced voltage along the nodes and thus the associated transmembrane voltage will be decreased quite considerably for the 7 μm axon diameter compared to the 12 μm axon diameter since the internodal distance L is greater in the latter case. Thus, the excitability will be decreased for the axons of lower diameter.

Results of Figure 6.7 show that the stimulation thresholds increase with increasing number of axons. By increasing the number of axons, we also increase the size of the axon population region and we expand the location of the axon population. Some axons will then be located in regions of lower electric fields or lower spatial gradient of the E-field along the axons. By increasing the size of the axon population region, we are more likely to find axons in different E-field iso-layers which will cause the differences between the axons' stimulation thresholds.

6.5.3 Stimulation Waveform

Bi-phasic stimulation requires slightly less amplitude to stimulate the nerves than the mono-phasic pulses. This indicates that bend-mode and end-mode stimulation may dominate as well as that the single phase duration is sufficiently long for excitation to develop. The axon population around N2 was slightly more sensitive in the mono-phasic configuration than in the bi-phasic configuration. Similar behavior was also recorded in Chapter 5 and explained by the additional chance for stimulation at the reversal phase for the bi-phasic pulses compared to the mono-phasic pulses [15]. Since cathodic stimulation has lower thresholds than anodic stimulation (in the straight-mode stimulation), the varying polarity of stimulus (bi-phasic stimulus) increases the probability of firing in comparison with the constant polarity (mono-phasic stimulus). N2 was activated with lower amplitudes than N1 using both mono-phasic and bi-phasic patterns. This is due to its branches being at the location with higher electric field values compared to the branches of N1

(Figure 6.2). N2 was more sensitive to the axon fiber diameter than N1. This can be explained by its exposure to higher electric field values, thus the effect of small changes in the axons diameter can be enhanced by these higher values of E-fields. However, due to the decreasing behavior of the plots in Figure 6.3, one can see that SI depends only on the stimulation thresholds for 7 μm and 12 μm. Thus, SI will mostly reflect changes occurring between these two edges of the axon diameter interval. Results of Figures 6.9 and 6.10 show that cathodic stimulation requires less amplitude to activate N1 and N2 axon population using mono-phasic pulses. This effect was also reported in the previous Chapter (Chapter 5) and several other studies [18]. This is due to lower maximum values of the E-field gradient along the axon for anodic stimulation compared to the cathodic one [15]. The value of the polarity ratio P is in agreement with various human perception experiments [7] where P is typically in the range of 1.25-1.5.

6.6 Conclusions

A sensitivity analysis of a realistic numerical model for a pVNS application was performed. The numerical model was used to investigate the excitation threshold in single and bundled axons with respect to the axon fiber diameter, axon number, SENN temperature, electrodes' penetration depth and position, and the ear conductivity. Results show that the stimulation thresholds increase with increasing number of axons and decreasing axon fiber diameter. Bi-phasic stimulation requires slightly lower amplitudes to stimulate the nerves than the mono-phasic stimulation. SENN model temperature and the ear conductivity effect are negligible compared to the effect of the axon fiber diameter and the electrodes' penetration depth. The electrodes' penetration depth is the most influential parameter with maximum sensitivity of 38 mV for each 0.1 mm and bundled axons.

References

[1] E Peuker and T Filler. *The nerve supply of the human auricle*. Clin. Anat., 15(1):35–37, 2002.

[2] A Saltelli, K Chan, and E M Scott. *Sensitivity Analysis*. 2000.

[3] D M Hamby. *A review of techniques for parameter sensitivity analysis of environmental models.* Environ. Monit. Assess., 32(2):135–154, 1994.

[4] Bertrand Iooss and Paul Lemaître. *A review on global sensitivity analysis methods*. Uncertainty management in Simulation-Optimization of Complex Systems: Algorithms and Applications, (around 30):23, 2014.

[5] Dan G. Cacuci. *Sensitivity theory for nonlinear systems. I. Nonlinear functional analysis approach*. Journal of Mathematical Physics, 22(12):2794–2802, 1981.

[6] Sim4Life Zurich Med Tech. *www.zurichmedtech.com/sim4life/*. 2016.

[7] J Reilly, V Freeman, and W Larkin. *Sensory Effects of Transient Electrical Stimulation - Evaluation with a Neuroelectric Model*. IEEE Transactions on Biomedical Engineering, BME-32(12):1001–1011, 1985.

[8] D McNeal. *Analysis of a Model for Excitation of Myelinated Nerve*. IEEE Transactions on Biomedical Engineering, BME-23(4):329–337, 1976.

[9] F Tilotta, B Lazaroo, M Laujac, and J Gaudy. *A study of the vascularization of the auricle by dissection and diaphanization*. Surgical and Radiologic Anatomy, 31(4):259–265, 2009.

[10] L Alvord and B Farmer. *Anatomy and orientation of the human external ear*. J. Am. Acad. Audiol, 8(6):383–90, 1997.

[11] A Chaturvedi, T Foutz, and C McIntyre. *Current steering to activate targeted neural pathways during deep brain stimulation of the subthalamic region*. Brain Stimulation, 5(3):369–377, 2012.

[12] S Safi, J Ellrich, and W Neuhuber. *Myelinated Axons in the Auricular Branch of the Human Vagus Nerve*. Anat. Rec, 299(9):1184–1191, 2016.

[13] Märta Sund Levander and Ewa Grodzinsky. *Variation in Normal Ear Temperature*, 2017.

[14] V Santis, X Chen, I Laakso, and A Hirata. *An equivalent skin conductivity model for low-frequency magnetic field dosimetry*. Biomedical Physics and Engineering Express, 1:1, 2015.

[15] Amine M. Samoudi, Stefan Kampusch, Emmeric Tanghe, Jozsef C. Széles, Luc Martens, Eugenijus Kaniusas, and Wout Joseph. *Numerical modeling of percutaneous auricular vagus nerve stimulation: a realistic 3D model to evaluate sensitivity of neural activation to electrode position*. Medical & Biological Engineering & Computing, 55(10):1763–1772, Oct 2017.

[16] Gernot Schmid, Stefan Cecil, and Richard Überbacher. *The role of skin conductivity in a low frequency exposure assessment for peripheral nerve tissue according to the ICNIRP 2010 guidelines*. Physics in Medicine and Biology, 58(13):4703–16, 2013.

[17] A M Samoudi, G Vermeeren, E Tanghe, R Van Holen, L Martens, and W Josephs. *Numerically simulated exposure of children and adults to pulsed gradient fields in MRI*. J. Magn. Reson. Imaging, 44:1360–1367, 2016.

Part IV

Conclusions

7 Conclusions and future research

This chapter summarizes the main achievements and conclusions obtained during this thesis. Furthermore, some opportunities for future research are mentioned.

7.1 Conclusions

Several topics related to the numerical modelling and optimization of different medical applications were studied in this dissertation. First, we investigated the induced eddy currents in SPECT/MRI systems using different arrangements of the SPECT collimators as well as new collimators' design strategies, including slit-slats, material reduction and z-shaped designs. Second part of this dissertation was dedicated to exposure assessment of adults and children in an MR scanner. We evaluated the induced electric fields in realistic 3D adult male, adult female, and child models within shielded whole-body x-, y-, and z-gradient coils and compared them with ICNIRP 2004, and IEC 2010 guidelines. Effect of the coils' and models' type, as well as the skin conductivity on the induced E-fields was investigated and discussed. The last part presented numerical modelling of the auricular branches vagus nerve stimulation (ABVNS). We established, a realistic model of the ABVNS application and investigated the effect of the electrodes' depth and position, as well as the stimulation pattern on the excitation threshold in single and bundled axons. We then, performed a sensitivity analysis of this numerical model by investigating effects of the axon fiber diameter, number of axons, model temperature, ear conductivity, as well as electrodes' penetration depth and position on

the stimulation thresholds for single and bundled axons.

In Chapter 1, we started by an overview of the medical imaging technologies with an emphasize on the magnetic resonance imaging technology. We explained the nuclear magnetic resonance principle used to acquire anatomical diagnostic images, then we introduced the main parts of an MR system (strong magnet, gradient system, and RF coils) with description of each MR system component. Safety considerations of patients in MRI systems was then investigated based on the IEC 2010 and ICNIRP 2004 guidelines. The normal operating mode and the first level controlled operating mode was detailed with the requirements that should be respected for each operating mode. Finally, the main parts of the nerve cell structure and function was presented along with the SENN model for myelinated nerve reaction to the electrodes' stimulations, including the transmembrane voltage equation along with the different SENN model parameters.

In Chapter 2, a numerical modelling of the transverse and longitudinal coils with different arrangements of the collimators was performed to investigate the induced eddy currents in the tungsten collimators due the MRI gradient coils for SPECT/MRI system.The numerical model was validated with measurements, and it was proposed as an efficient tool for studying the effect of SPECT collimators within the MRI gradient coils. We started by providing a detailed numerical model of the x, y, and z gradient coils along with pentagonal and hexagonal configurations of the collimators using a three-dimensional electromagnetic simulator with a time analysis tool. Then, we measured the resistivity of the printed tungsten used in the additive manufacturing of the collimators and reported dependency of the resistivity values to the measurement directions. Eddy current measurements for a single collimator were also performed and resulted in the conclusion that deviation in the magnetic field caused by the single collimator insertion can be completely removed by shimming after inserting the collimator in the bore. However, the final SPECT/MRI system will be composed of five or six collimator elements and thus eddy current characterization of the full ring of collimators is of huge importance. We then investigated the induced magnetic field in a full ring of pentagonal and hexagonal ring of collimators, and studied the effect of adding gaps between the collimators in the pentagonal geometry to reduce eddy current density <2 % of the applied gradient field. The residual eddy currents can be further reduced using new design strategies for SPECT collimators to reduce eddy currents and to provide more optimized collimator designs for SPECT/MRI integration, which is the main subject of Chapter 3. Chapter 2 was dedicated to the eddy currents due to gradient coils and does not consider other sources of eddy currents namely, the cryostat and RF coils. As a result, the final induced field can be higher when taking into consideration all the MR components. Numerical simulations can have an uncertainty of up to 20% (worst-case scenarios) and thus the maximum induced magnetic field can be greater than 2% of the applied gradient field in some cases

(Table 2.2)

Chapter 3 was dedicated to the investigation and reduction of the the induced magnetic field due to eddy currents in a full heptagonal ring of collimators by introducing smart design modifications. First, we characterized the current density (J) for different single collimators design and compared it to the original collimator current density. The induced magnetic field was then calculated for each ring of the adapted collimators and reduction in maximum induced magnetic field due to eddy current was reported and discussed. The small modifications to the collimator's design and surface resulted in a reduction of the maximum induced magnetic field by 53.8 % and 48.2 % for longitudinal and transverse coils, respectively, which results in an improved MR-compatibility with the heptagonal ring of collimators. Extrapolating results of the induced eddy current from the preclinical SPECT/MRI system to the clinical SPECT/MRI will result in much lower amplitudes of the induced fields. This is justified by the fact that in clinical MR system, the gradient strength is in the order of 40-50 mT/m compared to the 500 mT/m used in preclinical SPECT/MRI (higher gradient strength results in higher induced eddy currents).

In Chapter 4, we modeled the exposure of male, female and child patients to pulsed gradient fields typically used in MRI systems. We started by presenting the numerical model, including x-, y-, and z-gradient coils with detailed anatomical human models consisting of male, female and child human phantoms. The used numerical platform was then validated using a homogeneous sphere placed inside Helmholtz coils and the induced electric field evaluation methodology were described based on the ICNIRP 2004, and IEC 2010 guidelines. Results show that the strongest levels of field exposure are observed for the adult male inside the y-gradient coil. The first level controlled operating mode of the ICNIRP 2004 and IEC 2010 guidelines was not exceeded when the patients are inside the gradient coils, except for the adult male inside the y-gradient coil. The y-gradient tends to induce more fields in the models than the other coils. Effect of the skin conductivity on the induced E-field shows that the maximum electric field decreased with the skin conductivity value while only small effect is observed in the 99% value. Values reported in this chapter were calculated using the worst-case scenario and thus, the induced electric field can be lower than in most practical cases. However, special attentions should be paid, especially for adult male inside y gradient coils. The second part of this thesis was dedicated to the modelling and optimization of the percutaneous auricular branches vagus nerve stimulations.

In Chapter 5, a realistic numerical model for pVNS application at the human auricle including vessels and nerves was developed. The numerical model was used to investigate the stimulation thresholds and percentage of the activated axons with respect to stimulation waveform, electrode depth, and electrode position. The simulation model was then verified using experimental and analytical results

from the SENN model literature. The electric field distribution and its spatial gradient were calculated to explain the nerves' behaviors with respect to different stimulation patterns as well as the electrodes' position and penetration depth. Simulation results show that the cathodic bi-phasic pulse was the pulse requiring the least amplitude to activate the nerves. Chapter 5 provides a better understanding of the electric potential and current distribution in tissues surrounding the stimulation electrode. The feasibility and plausibility of the given model and tools was demonstrated. Investigations of the electrodes' position and depth effect stress the necessary accuracy while placing electrodes. Considering the high specificity and sensitivity of stimulation, due to the dense innervation of the auricle with various nerves, a sensitivity analysis of the numerical model is an important tool to better quantify the dependence of the numerical model developed in Chapter 5 to different parameters.

Chapter 6 is dedicated to perform a sensitivity analysis of a numerical model for pVNS. Dependency of the stimulation thresholds to the axon fiber diameter, axon number, SENN temperature, electrodes' penetration depth and position, and the ear conductivity was investigated and discussed. Results show that the stimulation thresholds increase with decreasing axon fiber diameter and increasing number of axons. Investigation of the waveform effect showed that bi-phasic stimulation requires slightly lower amplitudes to stimulate the nerves than the monophasic stimulation with cathodic pulses performing better than the anodic pulses. SENN model temperature and the ear conductivity effect are negligible compared to the effect of the axon fiber diameter and the electrodes' penetration depth. The electrodes' penetration depth is the most influential parameter with maximum sensitivity of 38 mV for each 0.1 mm and bundled axons. Sensitivity analysis results confirm Chapter 5 conclusions about the high importance of the electrodes' position to prevent opposite physiological reactions and an even adverse therapeutic outcome by unfavorable stimulation of pain-related Aδ fibers or under-stimulation.

7.2 Future research opportunities

In Chapters 2 and 3, we note here that we have focused only on the eddy current induced in the tungsten collimators. The proposed work does not consider the effect of coupling of the gradient and/or RF coils, nor the eddy currents on the cryostat magnet, which leads to some remnant error. An extension of this works would be to include an RF coil with the gradient coils and investigate the induced magnetic fields in both RF coils and collimators.

In Chapter 4, the human bodies were centered with respect to the coils. The position of the human body inside the coils influences the magnitude of the induced electric field. The changes, however, are typically below 20% for most measures and less than 5% for the average value of the electric field for a given tissue in a

given coil. Future works could consist of a sensitivity study concerning the effect of the human body's position inside the coils on the induced electric field using great population spans with different position of the human body models inside the gradient coils.

As a continuation of the study in Chapters 5 and 6, future works will consist of further evaluating the numerical model by comparing numerical results with experimental data using clinical studies. Additional stimulation patterns (pulses with equal energy, tri-phasic pulses, Figure 7.1) and bursted stimulation will also be investigated to perform both experimental validation and mutual optimization of the model and the experimental setup. The clinical data were already collected using 8 healthy adult volunteers (without any pain) of age 28 to 60 years (5 female), 3 young volunteers of age less than 40 years.

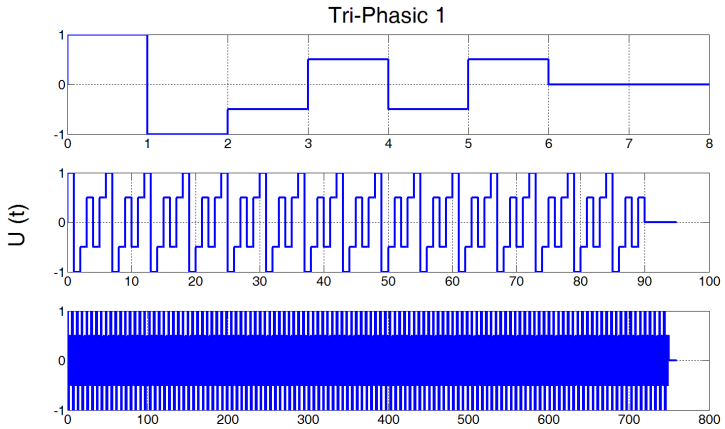

Figure 7.1: 1, 15, and 125 impulses per second using tri-phasic signal.